博士論文

Directed Self-assembly of Soft Matter Based on Spatiotemporal Control of Electric Field Pattern

（電場パターンの時空間制御に基づくソフトマターの誘導自己組織化）

宮廻 裕樹

Abstract

The self-assembly of soft matter is widely studied in the field of biology and engineering and can be applied to the nanomanufacture of materials. Direction of the self-assembly process is necessary for the precise control and measurement of the resultant nanostructures, but the existing directed self-assembly techniques have some limitations in terms of spatiotemporal resolutions and the degrees of freedom. In this thesis, I propose a new analysis and fabrication technique of soft matter is proposed to achieve operando analysis and directed self-assembly of soft matter using the spatiotemporal control of an electric field. The proposed techniques were applied to a directed self-assembly of some representative soft matter, such as lipid bilayers and DNA molecules.

First, the basic concept of virtual cathodes using an electron beam (EB) was introduced to achieve the spatiotemporal control of an electric field. Then, the electrical, chemical, and thermal effects of EB-induced virtual cathodes were discussed based on experiments and numerical simulations. As a result, it was shown that the thermal effect is small and that the electrical and chemical effects could be controlled by changing acceleration voltages.

Second, electrostatic effects of virtual cathodes were discussed. The governing equations of EB-induced virtual cathodes were formulated, and then these fundamental solutions were derived to calculate the electric field, spatial distribution of electrolytes, and diffusion of hydroxide ions generated by cathodic reactions. Using the derived fundamental solutions, a design procedure for a virtual cathode was proposed to achieve the desired distributions of the electric field and ionic concentration.

Third, it was shown that EB-induced virtual cathodes could induce electrokinetic phenomena, such as electroosmotic flows and electrophoresis. These phenomena could be applied to the manipulation of a single nanoparticle, the concentration patterning of nanoparticles, and the elongation of DNA molecules. It was also shown that EB-induced cathodes could induce surface reactions, such as the detachment of MPC polymers and the deposition of organic molecules.

Finally, the proposed techniques were applied to the electromechanical control of lipid membrane domains and morphology. By controlling the surface reactions of the EB-induced virtual cathode, the supported lipid bilayers(SLBs) were dynamically patterned. The fluidity and re-spreading of the SLBs could be controlled through the dose amount of the EB. Moreover, the re-spreading of the SLBs could induce directed self-assembly of phase separation in lipid mixtures. It was also demonstrated that the EB-induced virtual cathode could control the dynamic and reversible deformation of the stacked lipid bilayers by Maxwell's stress to them. These results indicated the proposed method could be applied to spatiotemporal measurements of the mechanical properties of SLBs.

Contents

List of Figures

Chapter 1

Introduction

1.1 Overview of soft matter

Soft matter is a general term for soft materials such as macromolecules and colloidal particles. Soft matter is common in biology and engineering. For example, DNA molecules are polymers consisting of deoxyribonucleic acid, and the proteins are polymers of amino acid. Plasma membranes are composed of phospholipid molecules which are amphipathic molecules, and cytoskeleton is composed of microtubules, actin filament, and intermediate filament, which are the polymers of proteins. Soft matter, such as rubber and liquid crystals, is applied in many engineering fields.

Soft matter usually consists of nanometer- or micrometer-scale components [1]; thus, the internal degrees of freedom of the structures of soft materials are large compared with hard materials such as metal crystals. The high degrees of freedom of soft materials contribute to the nonlinearity of the relationship between force and deformation and to the long relaxation time of deformation in response to external fields such as electric and magnetic fields [1]. Due to their nonlinearity and nonequilibrium, soft materials have a variety of structures and physical properties such as elasticity and viscosity.

For the application of soft matter to engineering, (i) the measurement techniques of the rheological properties and (ii) fabrication techniques of two- or three-dimensional structures using soft matter have been studied by many researchers. In the following three sections, these techniques will be overviewed.

1.2 Measurement techniques for microrheological properties of soft matter

Rheological properties, which are deformability and fluidity under mechanical stress, are important for characterizing the physical properties of soft materials. In measuring the rheological properties of a material, the material is placed between two plates and shear stress is applied to the material linearly or rotationally by moving one plate and fixing the other plate, and rheological parameters, such as viscosity, are calculated from the relationship between shear stress and deformation velocity [1]. However, this technique can be applied only to the measurements of the macroscopic properties of the material.

For microscopic measurements of rheological properties, such as DNA, proteins, and the lipid membranes of living cells, measurement techniques for the microrheology of soft materials have been studied in recent years [2]. There are two strategies for the measurement of microrheology. Passive microrheology [3,4] is based on the measurements of Brownian motions within soft materials. Tracers are placed and tracked within soft materials, and the mean squared distances of tracers are calculated. Viscoelastic properties can be calculated by using the Stokes-Einstein relationship. Active microrheology is based on the application of forces. For the application of forces, tracers are attached to the target material, and force is applied to the tracers using an electric field [5], a magnetic field [6], lasers [7], or atomic-force microscopy (AFM) [8]. This strategy has enabled *in-situ* measurements of the material, but the attachment of tracers is often needed, which might affect the viscoelastic properties of the target material. Moreover, the force can be applied only to tracers, so the degrees of freedom are still limited.

1.3 Fabrication techniques of soft matter

1.3.1 Top-down approach for fabrication of soft matter

In top-down approaches, microstructures are made by removing micro parts from large materials. Top-down approaches are achieved by micromachining such as photolithography [9] and soft lithography [10], and these technologies have enabled reproducible and fine structures of soft materials. However, photolithography and soft lithography techniques have fundamental limitations in spatial resolutions. Electron-beam lithography [11] is a candidate for the fabrication of nanostructures, but it needs vacuum conditions; thus, it is not suitable for soft materials in aqueous solutions, such as proteins. Moreover, the time and energy consumptions in top-down processes are relatively high.

1.3.2 Self-assembly: Bottom-up approach for fabrication of soft matter

To achieve low energy consumption and fabricate structures in milder conditions, bottom-up approaches based on self-assembly have been widely studied. [12] The self-assembly of molecules in aqueous solutions is a fundamental approach to creating higher-order structures in nature. In many self-assembly processes, many small molecules interact with each other via various intermolecular interactions and spontaneously form large and higher-ordered structures when the chemical potentials of the ordered structures are lower than the summation of the chemical potential per unit molecule. Such self-assembly processes can be found in many biomaterials. For example, the double-stranded structures of DNA molecules are formed via hydrogen bonding between base pairs, and the conformation of proteins also involves many intermolecular interactions including electrostatic, hydrophobic, and hydrogen bonds. The double lipid bilayers of living cells are formed via hydrophobic interactions among phospholipids, and their shapes and physical properties can be controlled by changing the electrical charges of head groups and mixing several

phospholipids with various hydrocarbon chains and head groups. Not only biomaterials but also non-biological materials, such as liquid crystals, block copolymers, colloidal particles and gels, can form ordered two-dimensional and three-dimensional structures, and such structures are applied in many fields.

Reversibility is one of the most important features in self-assembly processes. In 1991, Lindsey introduced seven types of self-assembly processes and clearly distinguished reversible self-assembly from irreversible self-assembly [13]. The main features of reversible self-assembly are summarized as follows:

- The intermolecular interactions of reversible self-assembly are usually dependent on non-covalent bonds, such as electrostatic interactions, van der Waals forces, hydrophobic interactions, hydrogen bonding, and excluded volume interactions (entropic interactions).
- Resultant structures from self-assembly processes are in thermodynamic equilibrium, and the structures can be easily and reversibly controlled by changing thermodynamic parameters such as temperature, pH, and ionic strength.
- Since the processes are reversible, the self-assembled structures are tolerant to synthesis errors.

In contrast, irreversible self-assembly processes are usually dependent on covalent bonds, and the processes are not tolerant of synthesis errors. Representative examples of reversible self-assembled structures are DNA, lipid molecules and block copolymers, and examples of irreversible self-assembly are the polymerization of chain polymers and allotrope forms of carbon and sulfur. As described above, reversible self-assembled structures are error-tolerant and easy to control and three-dimensional structures at the nano- and micrometer scales can be easily formed by reversible self-assembly processes; thus, reversible self-assembly processes are applied to many fields in engineering. For example, DNA origami techniques have been widely studied for the fabrication of three-dimensional structures by only designing the base sequences of DNA molecules [14]. Lipid molecules tend to form spheres called liposomes in water solution [15], and they are applied to drug delivery systems. Block copolymers are widely used to fabricate nanostructures by microphase separation [16] and are applied to the high integration of semiconductors, which cannot be achieved by top-down approaches, such as photolithography or soft lithography.

Although reversible self-assembly processes enable the efficient and easy fabrication of three-dimensional structures, reversible self-assembly has some limitations regarding the stability of structures. In the thermal equilibrium state, a reversible self-assembled structure is in a local minimum of free energy. Therefore, the self-assembled structure can be easily transformed from one to another by thermal fluctuations if the free energy has many local minima and the local minimum values are almost the same. This vulnerability to thermal fluctuations has a negative influence on the reproducibility and reliability of products in self-assembly processes. For example, the exact control of particle size in the fabrication of liposomes is difficult, and defects are formed in nematic liquid crystals

and block copolymers. In particular, the formation of defects in the nanostructures of block copolymers is a fatal problem in applications to the high integration of semiconductors, and many researchers have made great efforts to improve the reproducibility and uniformity of the nanostructures of block copolymers [17].

1.3.3   Directed self-assembly of soft matter

An integrated approach combining the top-down and bottom-up approaches is solution for achieving self-assembly with high reproducibility and reliability, because soft matter has large degrees of freedom in response to external fields. Directed self-assembly is a self-assembly process controlled by external fields. There are several types of directed self-assembly processes.

Directed self-assembly with topographic guides
Directed self-assembly techniques have been widely studied in the field of the micropatterning techniques of semiconductors. In directed self-assembly process, the microphase separation of diblock copolymers, which have two polymers, is used to make nanostructures [16]. As mentioned in Section 1.3.2, structures made through self-assembly fluctuate due to thermal disturbances. Therefore, the direction of nanopatterns cannot be controlled and defects inevitably form in the nanostructures of diblock copolymers. To overcome these problems, nanopatterns of diblock copolymers are directed using external topographic guides made via photolithographic techniques [17].

Directed self-assembly of stimuli-responsive materials
Directed self-assembly is also achieved by using stimuli-responsive materials whose molecular structures can be changed by external fields. For examples, photo-responsive materials have photochromic structures, such as azobenzene structures, whose cis-trans bonds can be controlled by irradiating light, and structural changes of photo-responsive materials can be achieved by changing the polarity and electrical charges of the materials [18]. The dynamic phase separation of artificial lipid membranes has been achieved by adding lipid molecules with azobenzene [19]. Various external fields, such as electric field, magnetic field, pH, and temperature, are used for the stimulation of materials.

1.4   Need for operando analysis of soft matter in aqueous solutions

As discussed in Sections 1.2 and 1.3, the challenging problems in the measurements and fabrication of soft matter are summarized as follows:

- For measurements of the microrheology of soft matter, the precise application of forces is needed. However, previous techniques of passive and active rheology need to attach tracers to target materials, and the degrees-of-freedom for the manipulation of the material.
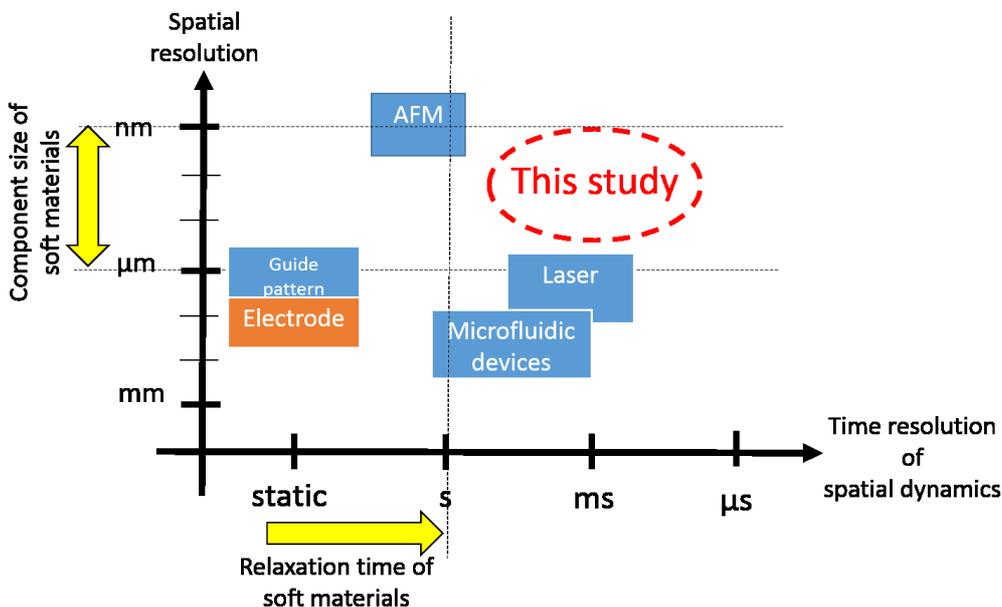
Fig. 1.1. Relationship between spatial resolution and time resolution of spatial dynamics of various manipulation techniques.

- For the fabrication of soft matter at the nanometer scale, the integration of the top-down approach and self-assembly process is needed. The existing techniques with guide patterns are candidates for this integration, but the guide patterns are fixed and cannot be dynamically changed, which means the dynamic control of self-assembly cannot be achieved by only using guide patterns.

Therefore, it is considered that the non-invasive and spatiotemporal control of soft matter in aqueous solutions by external fields is needed in the aspects of the measurement and directed self-assembly of soft matter.

To achieve the non-invasive and spatiotemporal control of soft matter with external fields, the spatiotemporal analysis of the behaviors of soft matter under external fields is needed. The spatiotemporal analysis of materials under their working conditions is known as "operando analysis," and includes both high spatiotemporal resolutive measurements and the active control of external fields to imitate the external environment. [20–22] Operando analysis is regarded as the key technology for the improvement of devices, development of new materials and finding of biological phenomena. Previous works on operando analysis have been focused on solid–liquid or solid–gas interfaces in fuel batteries, chemical catalysts, and electric devices, and these works are based on the emission spectroscopy of X-ray and Raman scattering and microscopes, such as transmission electron microscope and scanning probe microscopes. In other words, previous works have focused on pure solid, liquid or gas materials and the distributions of elements or ions are mainly measured. Contrary to this, we should think following requirements for the operando analysis of soft matter.
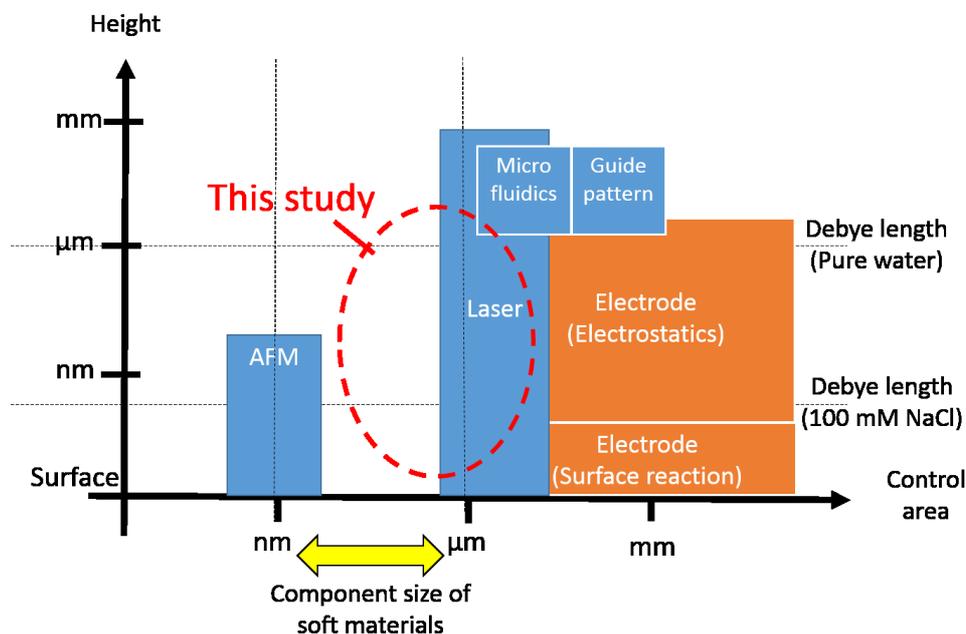
Fig. 1.2. Relationship between controllable height and area of various manipulation techniques.

- Operando analysis should be performed not in a vacuum space, but in aqueous solutions since most soft materials are diluted in water. Therefore, external fields that are effective in aqueous solutions should be chosen.
- The control of intermolecular interactions such as electrostatic or hydrophobic interactions, as well as physical parameters such as temperature and pH, is needed.
- A micro- to nanometer scale resolution is needed considering the characteristic lengths of self-assembled structures of soft materials.
- A milli- to microsecond scale resolution is needed considering the relaxation time of the self-assembled structures of soft matter.

Considering these requirements, existing techniques for the control of external fields are classified as 1.1 and 1.2. As shown in Figs. 1.1 and 1.2, AFM can realize manipulation at the nanometer or several-tens-of-nanometer scale, but the time resolution of moving probes is in the second scale (AFM) or the video frame rate (FM-AFM). In contrast, optical tweezers can achieve kHz order manipulation using galvanometer mirrors, but spatial resolution is limited to several hundreds of nanometers due to the diffraction limit of light. Therefore, challenging problems remain in spatiotemporal resolutions to realize the operando analysis of soft materials, and new techniques are needed.

1.5   Objectives of this thesis

The objectives of this thesis are to propose new analysis and fabrication techniques for soft materials that can achieve (i) spatial resolutions at the micro- to nanometer scale and (ii) the time resolution of spatial control at the milli- to microsecond scale. The contributions of this thesis are as follows:

- The formulation of virtual electrode techniques based on charged particle beams and the physical analysis of electrostatic, electrokinetic, and surface reaction phenomena induced by the virtual cathode
- The physical confirmation of electrostatic, electrokinetic, and surface reaction phenomena using an electron beam-induced virtual cathode display system
- The demonstration of the operand analysis of biomolecules, such as DNA and lipid molecules, and the realization of directed self-assembly using an electron beam-induced virtual cathode

1.6   Organization of this thesis

This thesis consists of seven chapters. The overview of this thesis is shown in Fig. 1.3. Overviews of each chapter are as follows: In Chapter 1 (this chapter), the fabrication and measurement techniques of soft matter are overviewed and the objectives of this thesis are described.

In Chapter 2, the concepts and advantages of the virtual electrode are overviewed and the physical realization of the virtual cathode display system using an electron beam (EB) is proposed. In addition, the physical effects of the EB-induced virtual cathode are described.

In Chapters 3–5, the basic mechanisms of the virtual electrode are studied. In Chapters 3 and 4, the environmental controls of electrostatics and electrokinetics are studied. By using these controls, the control of several physical parameters, such as the electric field, pH, temperatures, ionic concentrations and shear stress, has been achieved. In Chapter 5, we show that the virtual cathode can induce surface reactions and that nanoprocessing, such as the deposition and detachment of organic molecules, can be achieved by the virtual cathode.

In Chapters 4 and 6, we demonstrate several operando measurements and the directed self-assembly of soft matter, such as DNA molecules and lipid bilayers, based on the results in Chapters 3–5.

Finally, we conclude this thesis and discuss future directions based on this study in Chapter 7.
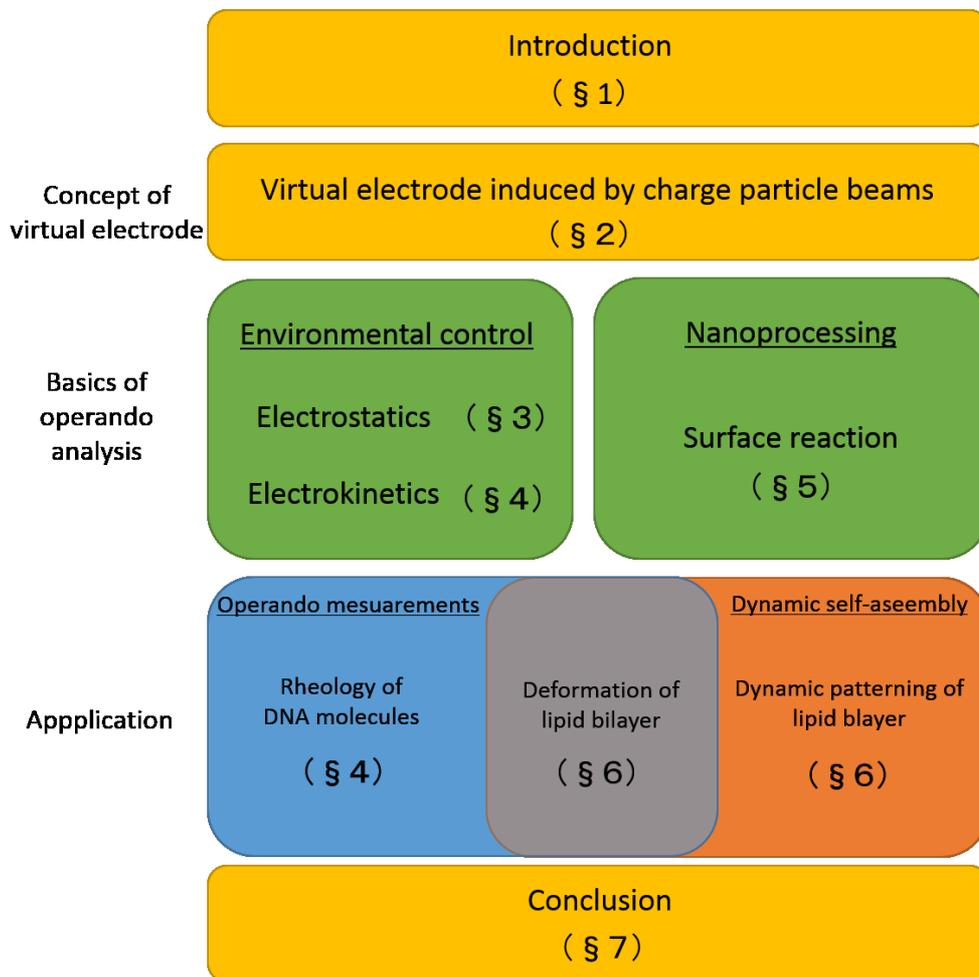
Fig. 1.3. Organization of this thesis

Chapter 2

Virtual Electrode System for Soft Materials Based on Charged Particle Beams

The aim of this chapter is to propose concepts related to the virtual cathode system technique based on charged particle beams. In Section 2.1, two approaches of virtual electrode techniques are overviewed, and the advantages and disadvantages of the two approaches are discussed. In Section 2.2, a virtual cathode display based on an inverted electron beam (EB) lithography system is proposed, and the physical effects of our display system are discussed. In Section 2.3, the relationship between acceleration voltage and physical effects of electron beams is discussed. In Section 2.4, the temperature rise around the EB-induced cathode is measured. Finally, the summary of this chapter is given in Section 2.5.

2.1 Overview of the virtual electrode display system

Electrodes are widely used for electrical measurements such as cyclic voltammetry or measurements of impedance and manipulations such as electrophoresis in biology or chemistry. For spatial control of an electric field, multielectrode arrays (MEAs) have been studied, especially in the field of neuroscience. However, electrodes cannot be changed on demand because electrodes are fixed after fabrication, and thus the degrees-of-freedom of electrical manipulation using electrodes are essentially limited.

In recent years, virtual electrode techniques have been studied to achieve more degrees-of-freedom of electrical manipulation. There are two types of virtual electrodes which are described as follows.

2.1.1 Optoelectric tweezers

Using optoelectric tweezer [23–26] is one way of generating a local virtual electrode by using photoconductive materials. The basic setup of optoelectric tweezers is shown as Fig. 2.1(A). In this setup, liquid samples are sandwiched between two parallel glass plates.

One plate is coated with indium tin oxide (ITO), and the other is layered with ITO, hydrogenated amorphous silicon (a-Si:H), and an insulator such as silicon nitride (SiN). The two ITO-coated glass plates are connected to a DC or AC power supply. When the hydrogenated amorphous silicon is irradiated by light, charged carriers such as holes and electrons are generated. Therefore, the electrical conductivity of the light-irradiated area becomes lower than that of the unirradiated area, and a voltage drop down in liquid samples is observed only in the light-irradiated area. As a result, a non-uniform electric field is generated, as shown in Fig. 2.1(A). This electric field generated by light illumination can be viewed as a virtual electrode. The main features of optoelectric tweezers are summarized as follows:

- The strength of the electric field can be controlled by changing the intensity of light.
- The shapes of virtual electrodes can be controlled by changing the illumination patterns. Scanning lasers with a galvano mirror, liquid crystal display, projectors, and digital micromirror devices have been used for the creation of illumination patterns.
- Using an AC power supply, electrokinetic manipulations such as dielectrophoresis or AC induced electroosmotic flows can be achieved.

2.1.2   Charged particle beams with liquid cells

Another approach in generating virtual electrodes is the use of charged particle beams such as electron beams(EBs) and focused ion beams, which are accelerated by external fields and have electric potential energy and kinetic energy. However, these beams require a vacuum environment for prevention of scattering. Thus, liquid cells are used to separate vacuum space from liquid samples. Fig. 2.1(B) shows the basic concepts of virtual electrode formation using charged particle beams with liquid cells. Using insulator such as SiN, the vacuum and liquid samples are separated, and the beams are irradiated from the vacuum space to the insulator. When the kinetic energy of the beams is sufficiently low, the charged particles are stopped with the insulator and an electric field would be induced by the stopped particles within the insulator. Thus, the electric field induced by the charged particles can be viewed as a virtual electrode. The main features of this virtual electrode are summarized as follows:

- The strength of the electric field can be controlled by the maximum range and dose amount of the beams.
- The shapes of the virtual electrodes can be controlled by the scanning beams.

Spatial resolutions can be improved when electron beams or focused ion beams are used, since their wavelengths are shorter than the wavelength of visible light. Moreover, the temporal resolution of their manipulations is in the micro- to millisecond range because of the small mass of the charged particles. This means that the temporal resolution is

(A) Optoelectric tweezer

(B) Charged particle beams with liquid cells
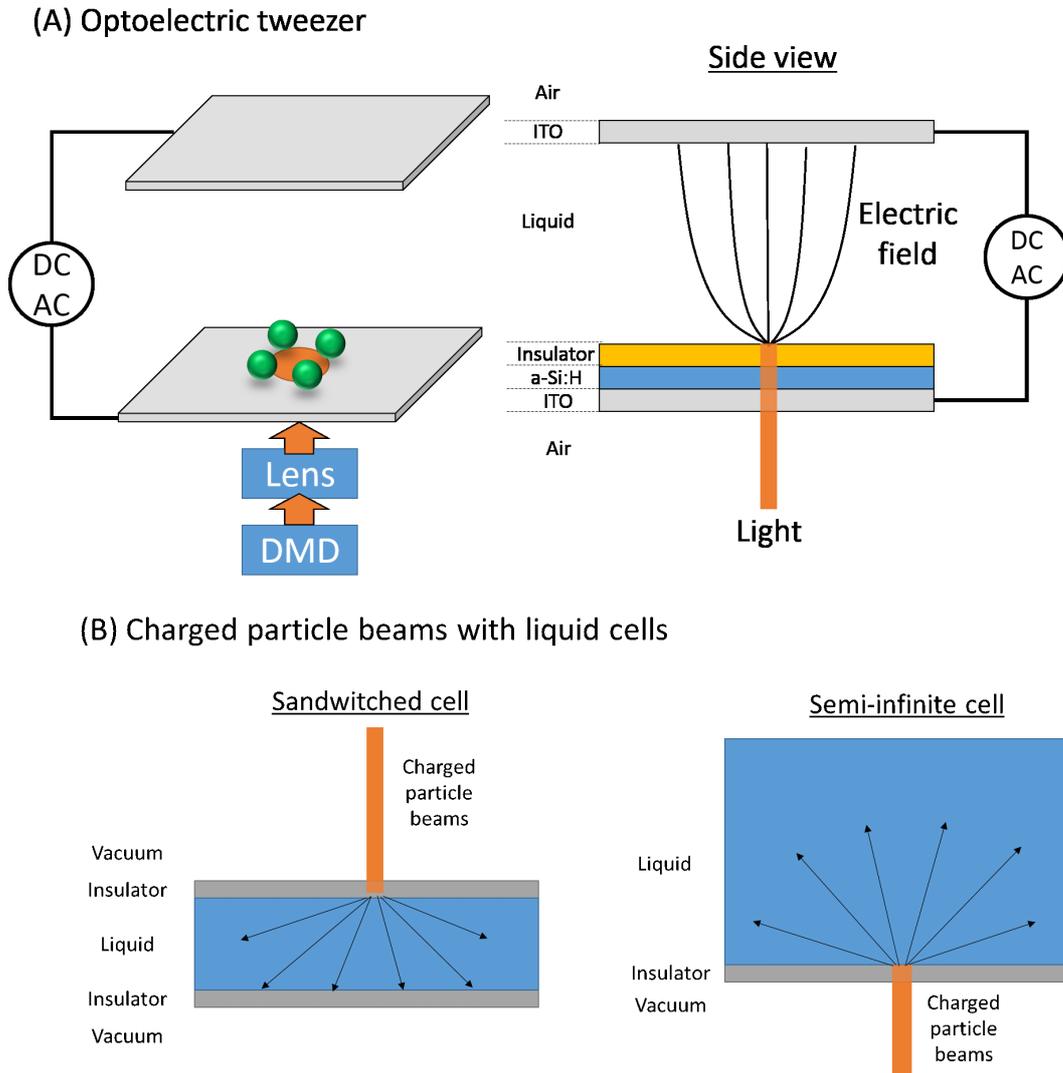
Fig. 2.1. Physical implementation of virtual electrode system.

high enough to control the soft matter. However, vacuum environments are needed in this approach.

Electron beams are often used for generation of virtual electrodes. Ogura and coworkers applied this virtual electrode technique to electrochemical microscopy of living cells, which had an 8-nm-resolution [27]. Moreover, Donev and coworkers achieved a 50-nm chemical deposition on the virtual electrode [28]. As described in Chapter 1, soft materials usually consist of nanometer- or micrometer-scale components. Therefore, an electron-beam-induced virtual cathode would be more suitable than light addressable electrodes given the spatial resolution of virtual electrodes.

2.1.3 Advantages and limitations of virtual electrodes

One of the advantages of the virtual electrodes is the designability of electrodes on-demand. As described in 2.1.1 and 2.1.2, the shapes or strength of virtual electrodes can be easily controlled by controlling only the illumination of a light pattern or scanning of the charged particle beams. Moreover, local point charges can be generated by spot illumination of light or irradiation of beams. Therefore, the design of a virtual electrode can be realized if an electric field or other physical parameters are subject to linear partial differential equations (PDEs) and the fundamental solutions (Green's function) to these equations are linear to the intensity of light or dose amount of the beams in accordance with the superposition principle. The details of designing virtual electrodes using Green's function are discussed in Chapter 3.

Another advantage of virtual electrodes is their surface smoothness. MEA or CCD arrays can achieve spatial control of an electric field, but their surfaces are not smooth. Smoothness of the surface is crucial for fabrication of soft membranes, such as supported lipid bilayers and a self-assembled monolayer, since the thickness of the membrane is on the order of nanometers. On the contrary, laser or charged particle beams can generate an electric field only by irradiation; hence, smoothness of the surface would be guaranteed. Consequently, such beam techniques can be applied to the manipulation of membranes.

In spite of such designability, there are some limitations with regard to the current virtual electrode techniques as follows:

- In the case of light techniques, both anode and cathode cannot be simultaneously generated on the light-illuminated plate. Similarly, the polarity of electrodes is basically fixed according to the charge of the beams when using beam techniques.
- Virtual electrodes are generated only at the surface of the insulator, and vertical control is basically limited within the electric double layer.

In this thesis, the target materials are soft materials, the size of which is on the order of nanometers or micrometers, and the Debye length of the electric double layer can range from 1 to 1000 nm in biological conditions. Therefore, the control of soft materials within the electric double layer would be possible using virtual electrode techniques.

2.2 Virtual cathode display system based on an electron-beam lithography system

In this thesis, an inverted electron beam processing system was used to make virtual electrodes in aqueous solutions. This system was constructed by Hoshino and coworkers in 2013 [29]. The overall view of the system is shown in Fig. 2.2. This system consists of an inverted electron beam microscope (Mini-EOC, Apco. Co.) and an epifluorescence

microscope (IM-3, Nikon), and they are placed coaxially. A 100-nm-thick SiN membrane (NT025C, NORCADA) is used to separate vacuum from the liquid sample. The liquid samples are observed with a fluorescence microscope which is equipped with a white light source (SOLA, Lumencor) and a highly sensitive scientific CMOS camera (pixel size = 6.5 μm $\times$ 6.5 μm, NEO sCMOS, Andor). Observation of the samples and the control of the electron beams are synchronized using a digital I/O board (BNC2120, National Instruments).

An electron beam is formed by accelerating electrons by applying an electric field. When an external acceleration voltage V is applied to electrons, the electrical potentials of the electrons under external electric field are converted into kinetic energy, and the electrons are accelerated. Therefore, the following conversation law of energy is satisfied.

$$eV = \frac{1}{2}m_e v^2,$$

where e is quantum of electricity, m_e is the mass of an electron, and v is the velocity of an accelerated electron.

According to quantum mechanics, electrons behave as both waves and particles. When it is assumed that electrons have kinetic energy $E(=\frac{1}{2}m_e v^2)$ and momentum p as particles and that the electrons have a frequency ν and wavelength λ as waves, the following two equations hold:

$$E = h\nu, \quad p = h/\lambda,$$

where h is the Planck's constant. From these equations and $p = m_e v$, the wavelength λ is calculated as follows:

$$\lambda = \frac{h}{p} = \frac{h}{m_e v} = \frac{h}{\sqrt{2m_e eV}}.$$

This wavelength is called as the "de Broglie wavelength." For example, the de Broglie wavelength of a 2.5 keV electron beam is about 0.017 nm, and this is much shorter than that of lasers (several hundreds of nanometers). Therefore, the spatial resolution of the electron beam-induced virtual cathode is expected to be much finer than that of optoelectric tweezers. However, the actual spatial resolution of the virtual electrode becomes thicker than the wavelength of electron beams because electrons are scattered when the electron beams are irradiated onto a solid, as described in 2.2.1.

2.2.1 Physical effects of an electron beam

When electron beams are irradiated onto a SiN membrane, electrons interact with atomic nucleuses and electrons bound by atoms within the membrane, and thus electrons are scattered. According to literature [30], the details of the scattering process are summarized as follows:

- When incident electrons (or primary electrons) interact with atomic nucleuses, elastic collisions between the electrons and the atomic nucleuses occur because
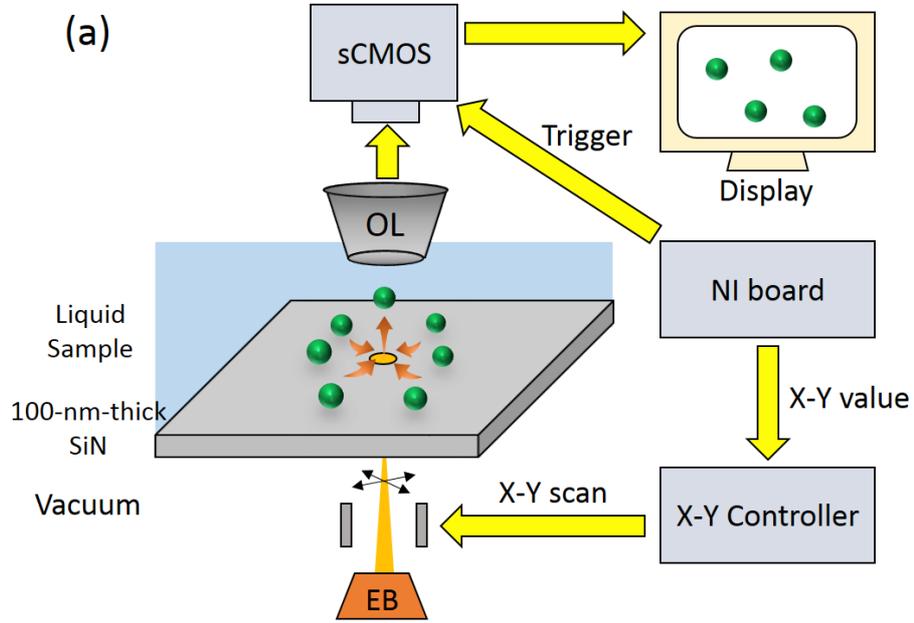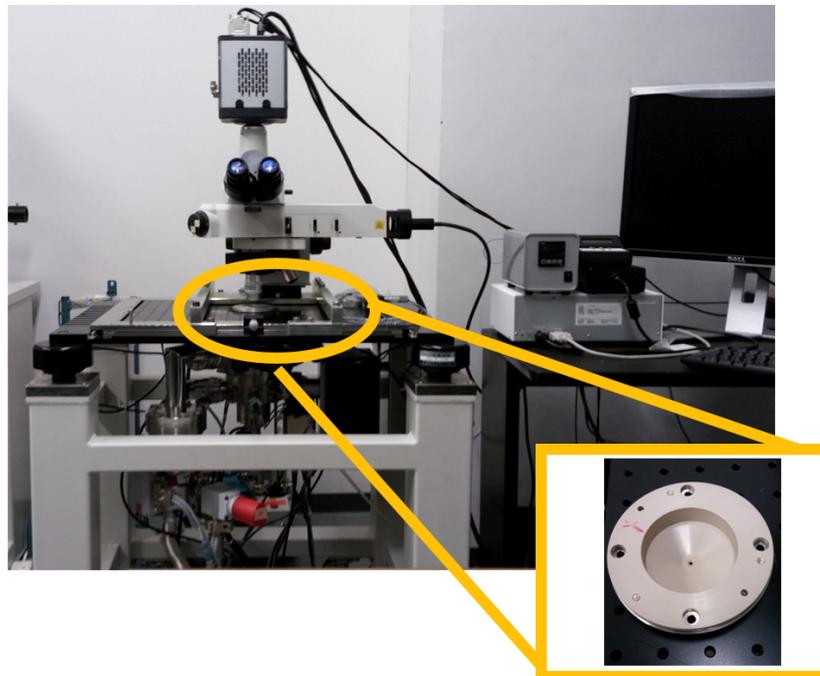
Fig. 2.2. Physical implementation of virtual electrode system using an inverted electron beam lithography system.

of the potential energy of the atomic nucleuses. By these collisions, kinetic energy is converted into thermal energy because of the energy loss during the collisions. Moreover, the directions in which the incident electrons move change, and bremsstrahlung X rays generated. Some electrons are backscattered to the vacuum space or forward-scattered to the liquid sample.

- When incident electrons interact with electrons bound by atomic nucleuses, the bounded electrons are ejected from their orbits, and thereby, vacancies are generated in the orbits. These ejected electrons are called "Auger electrons," and the vacancies are filled in by the external electrons in the external shell. Since the energy level of the inner shell is higher than that of the external shell, the energy difference before and after the filling of vacancies may induce the emission of X-rays or energy conversion to kinetic energy of the Auger electrons. Auger electrons are diffused within the membrane or scattered into the vacuum and liquid samples as secondary electrons. The ejection of electrons in the outermost orbit as Auger electrons induces a change of bonds between atoms.

Therefore, the kinetic energy of the accelerated electrons is converted into the following five energies during the scattering process:

1. Thermal energy in the SiN membrane and the liquid sample;
2. Kinetic energy of backscattered or forward-scattered primary electrons;
3. Kinetic energy of backscattered or forward-scattered secondary electrons;
4. Radiation energy of X-rays;
5. Chemical energy for the change of atomic bonds.

In addition, the stopped electrons within the membrane can electrically interact with atoms, ions, or molecules within the liquid sample.

In summary, irradiation of electrons onto a SiN membrane can induce the following physical effects on the liquid samples:

1. Thermal effects induced by loss of kinetic energy during the scattering process;
2. Electrical effects induced by negative charges of electrons;
3. Chemical effects induced by forward-scattered electrons.

Thermal and electrical effects can realize environmental control of soft materials such as temperature, pH, and electric field, whereas electrical and chemical effects can realize nanoscale processing such as chemical deposition and ablation of molecules and electrochemical deposition. Since these effects are induced simultaneously, an independent control of these physical effects is needed. To this end, thermal effects are evaluated in the next section, and electrical and chemical effects are evaluated in Chapter 5.
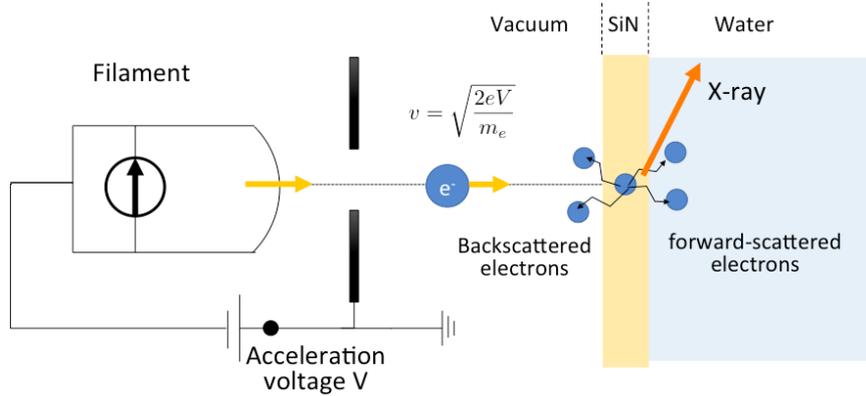
Fig. 2.3. Schematic views of acceleration and scattering of electrons.

2.3   Measurements of temperature rise during EB irradiations

To evaluate the thermal effects of scattered electrons, the temperature rise during the EB irradiations was measured using rhodamine B (RhB). RhB has been utilized as a thermosensitive fluorescent indicator in micro- and nanodevices [31–33]. At room temperature, the fluorescence intensity of a RhB solution exhibits an approximate linear relation to the solution temperature because the quantum yield of RhB decreases with an increase in the temperature [34, 35].

2.3.1   Materials and methods

EB-induced thermal changes on the SiN membrane at spot EB were measured using the fluorescence intensity of RhB as the thermosensitive probe. RhB (Wako) was dissolved in deionized ultrapure water at a final concentration of 0.02 mg/mL. It was observed that the temperature coefficient of the fluorescence intensity of a 0.02 mg/mL RhB water solution was about -2%/K at 25°C–30 °C under controlled bulk solution temperature using the lens-mounted heater and the fluorescent microscope. The RhB solution was pipetted on to the SiN membrane of the I-EBL system. The solution temperature was controlled at 25°C using the lens-mounted heater. EB was spotted to the SiN membrane with an acceleration voltage of 2.5 keV and beam currents of 4.3 and 13 nA for 1 s. The changes in the fluorescence intensity were observed by the fluorescence microscope with a filter (Ex: 540/25, Em: 605/55, TRITC, Nikon). The evaluation region was set to a circular region with a diameter of 1 μm, centering on the spot EB. The effect of photobleaching was corrected using a liner time function. The electrophoretic mobility of RhB molecules was not considered for these measurements and the following temperature estimation.

t = 1 s t = 2 s t = 3 s
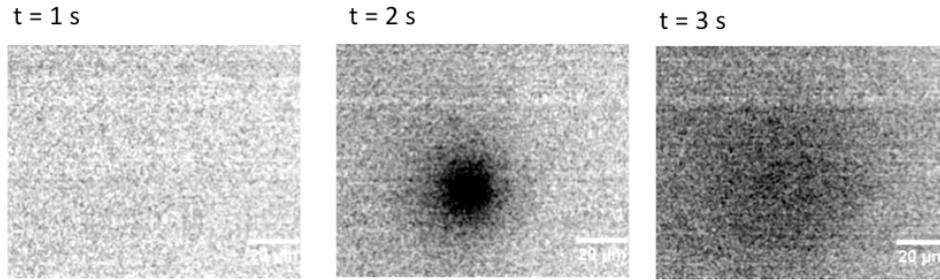
Fig. 2.4. Time lapse images of fluorescence intensity of rhodamine B(RhB) during EB irradiation. The EB was irradiated from 1 s to 2 s.

2.3.2 Results and discussion

Fig. 2.4 shows fluorescence images of RhB in pure water before and after the EB irradiations. The EB spot was irradiated from 1 to 2 s. During the EB irradiation, a decrease of the fluorescence intensity was observed, and a recovery of the intensity was observed after the EB irradiation. (It should be noted that the effects of photobleaching due to scattered electrons would be little as discussed in Chapter 3.)

The time response of the fluorescence intensity in the circular region is shown in Fig. 2.5. The fluorescence intensity was normalized by its value at $t = 0$, and the average of the normalized intensity in the circular region was plotted on the diagram. The maximum decrease in fluorescence intensity at the EB irradiation was about -1%. This means that the temperature increase at the spot EB was 0.5°C during the EB irradiation with an even beam current of 13 nA.

The relationship between the average of the normalized intensity and the distance from the EB spot is shown in Fig. 2.6. The acceleration voltage and beam currents were set at 2.5 keV and 4.3 and 13 nA, respectively. A 9×9 mean filter was applied to the fluorescent image, and the fluorescence intensity was normalized to its value at 100 ms before the start of the EB irradiation (correction of photobleaching was not performed). The intensity within 50 μm from the EB spot dropped after EB irradiation of 1 s. Therefore, a temperature rise was observed on the order of several micrometers.

According to the results of the thermal measurements, a rise in the temperature rise was observed, but the temperature change corresponding to 1 s of irradiation of the 2.5 keV EB was only about 0.5°C when the beam current was 13 nA. Therefore, the thermal effects due to the scattering of electrons would be small. This result means that the proposed virtual cathode technique can be applied to manipulations of proteins, since the denaturation of proteins occurs at temperatures above 40°C.

2.4   Conclusion of this chapter

In this chapter, the current techniques of virtual electrode were discussed, and the basic concept of a virtual electrode induced by charged particle beams was introduced. For the physical implementation of a virtual electrode, a virtual cathode display system using an inverted EB lithography system was proposed, and the physical effects of the EB-induced virtual cathode, such as electrical, chemical, and thermal effects, were discussed. By measuring temperature rise of RhB water solution, it was confirmed that the thermal effect around the EB-induced virtual cathode was small.
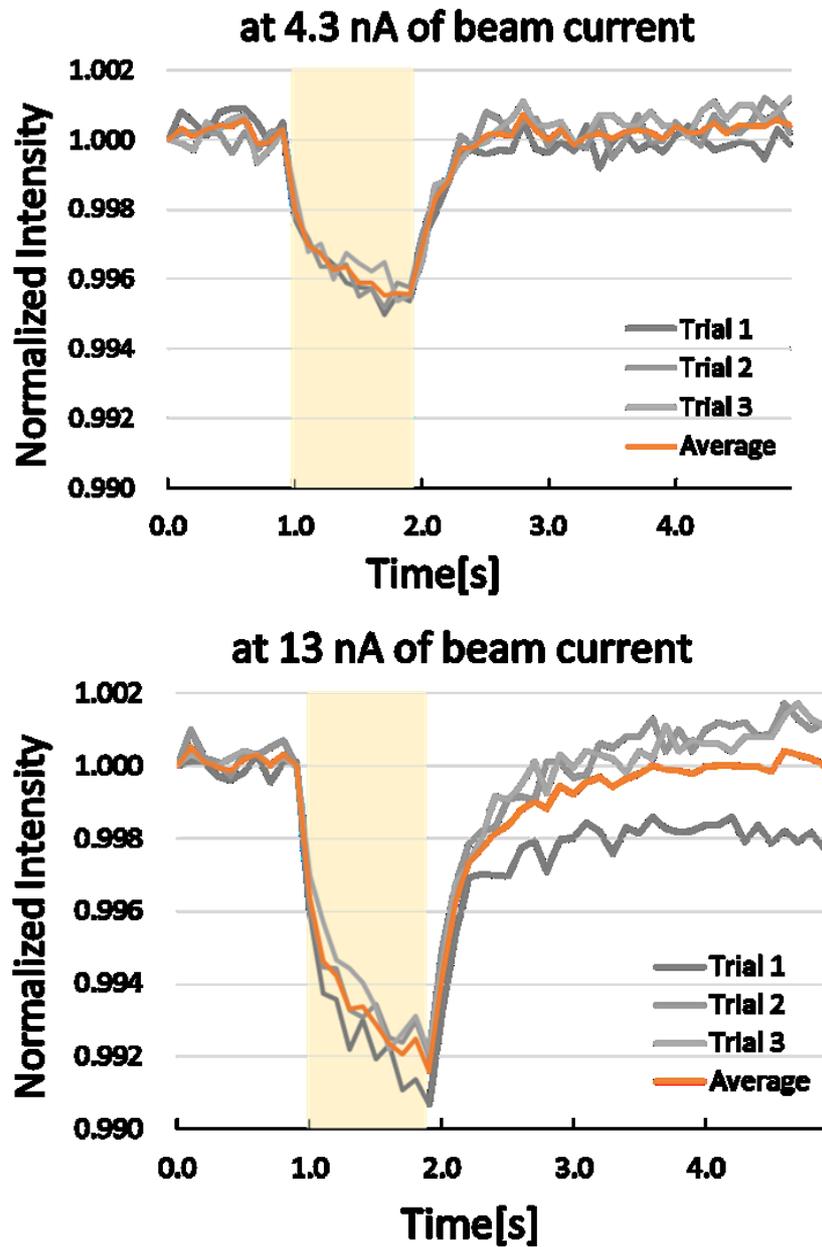
Fig. 2.5. Time responses of temperature changes during the spot EB irradiation at the spot. Rhodamine fluorescence intensity indicated a temperature change with a thermal coefficient of $-2\%/\text{K}$. Meshed period is duration of EB irradiation. The temperature changes were about 0.25 K and 0.50 K, which increased at beam currents of 4.3 and 13 nA, respectively.
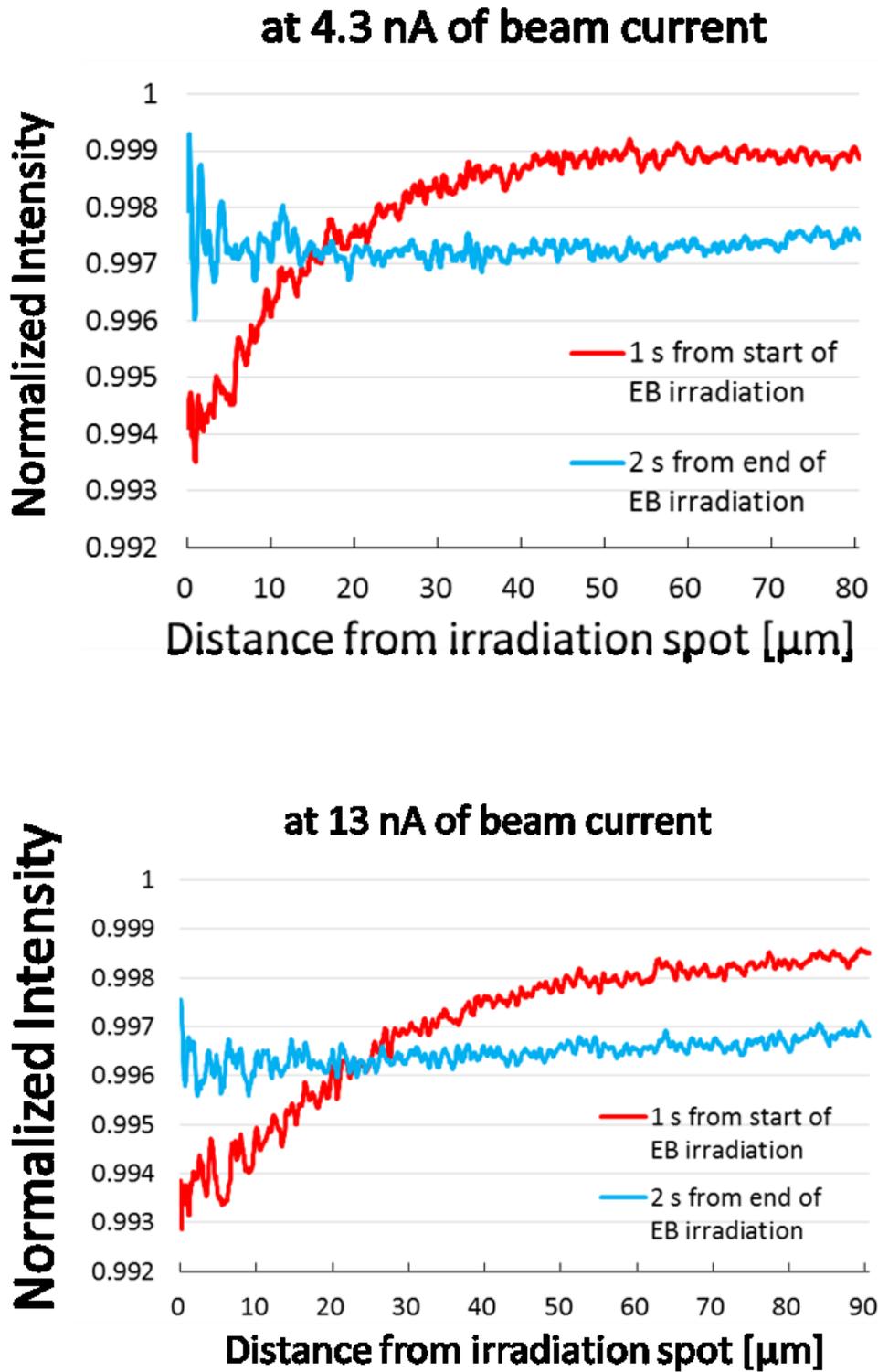
Fig. 2.6. Spatial profile of temperature change at the spot EB with beam currents of 4.3 and 13 nA at t=2.0 s of Fig. 2.5 (correction of photobleaching was not performed).

Chapter 3

Physical Model and Design of a Virtual Cathode in an Electrolyte Solution

The aim of this chapter is to derive physical models of an ideal cathode on a submicrometer scale in an electrolyte solution and to propose a design procedure for a virtual cathode based on the fundamental solutions of electric field and ionic concentrations around the virtual cathode. To this end, the physical conditions of the ideal virtual cathode are formulated in Section 3.1; then, the governing equations are solved to derive the fundamental solutions of the electric field caused by Ohmic currents and ionic concentrations around an ideal cathode at the submicrometer scale in an electrolyte solution in Section 3.2. In Section 3.3, a design procedure for a virtual cathode is proposed using the fundamental solutions. In Section 3.4, it is experimentally demonstrated that a pH increase and ionic shielding are induced around the EB-induced virtual cathode.

3.1 Physical conditions of a virtual cathode in a monovalent electrolyte solution

We consider a circular cathode (radius: a) on an insulator plane, as shown in Fig. 3.1. For the symmetry of the cathode, a cylindrical coordinate system (r, θ, z) is used in this chapter. It is assumed that the origin of the coordinate system is the center of the cathode and that a water solution with supporting electrolytes is filled in the region where $z > 0$. We assume that the supporting electrolytes are symmetrically monovalent (1:1), and we denote the cation and anion of the electrolytes as p and n respectively (Fig. 3.2). The counter electrode is assumed to exist at infinity. For simplicity, it is assumed that the surface of the insulator plane is not electrically charged and an electric double layer is not formed at the interface between the insulator surface and the water solution in this chapter. (The electrokinetic effects of the electric double layer around the cathode will be discussed in Chapter 4.)
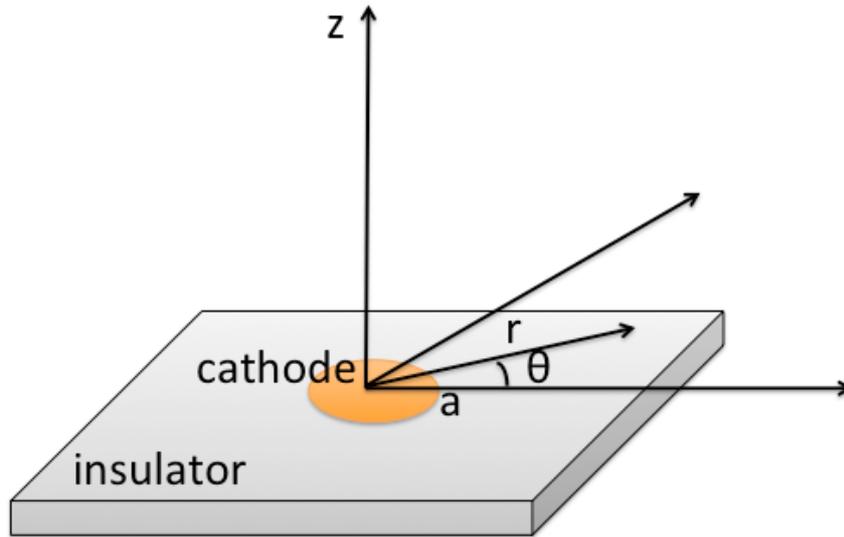
Fig. 3.1. Geometrical definitions of a circular virtual cathode.
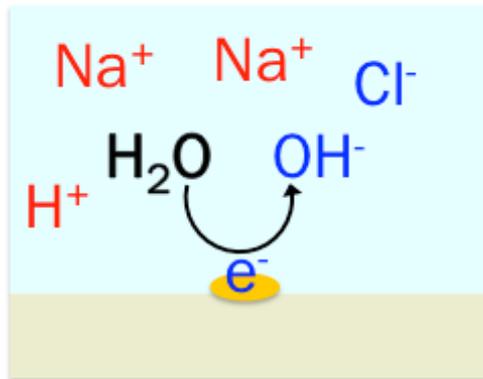
Fig. 3.2. Schematic view of ionic environment around a virtual cathode. In this figure, supporting electrolytes are NaCl. In addition, very small amount of protons and hydroxide ions exist due to ionization of water, but this can be neglected for the calculation of ionic concentration of the supporting electrolytes.

3.2   Fundamental solutions of electrochemical phenomena around a virtual Cathode

3.2.1   Electric field induced by Ohmic current

When the total amount of steady current through the circular cathode is I and the current flows through the solution isotropically, the current density j in the region where $r > a$ is calculated as follows:

$$j = \frac{I}{2\pi(r^2 + z^2)}.$$
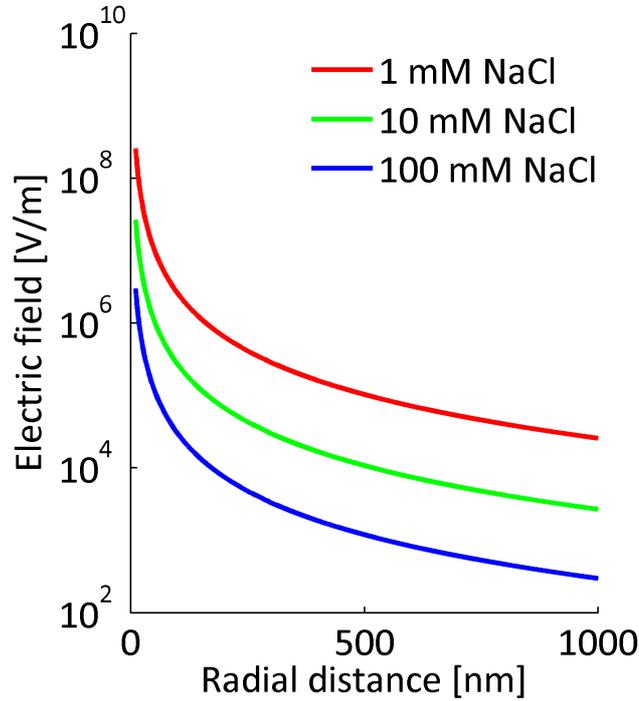
Fig. 3.3. Spatial distribution of the strength of the electric field caused by Ohmic currents flowing from the virtual cathode to the solution.

According to Ohm's law, the relationship between the electric field $E(=-\nabla\phi)$ and current density j can be written as

$$E = \rho j,$$

where ρ is the electrical resistivity of the solution. Thus, the electric field due to the Ohmic current is given by the following equation:

$$E = \frac{\rho I}{2\pi(r^2 + z^2)}$$

Fig. 3.3 shows the spatial distribution of the strength of the electric field caused by Ohmic currents in the NaCl solution according to the above equation. The electrical resistivities of 1, 10, and 100 mM NaCl solutions were calculated from the literature values for the molar conductivity of the NaCl solutions [36] and assumed to be 81, 8.4, and 0.94 Ωm, respectively. The electric field is weakened as the ionic concentration was high because of the effects of ionic shielding. Therefore, it is expected that the spatial resolution of the electric field can be finer using highly concentrated electrolyte solutions.

3.2.2   Electric double layer formation of ions

According to the previous subsection, a voltage drop is induced around the virtual cathode because of the Ohmic current. In this case, ionic shielding can be induced by supporting electrolytes in the solution, and the ionic concentration around the cathode can be

calculated based on Nernst-Planck equations. In case of monovalent electrolytes, the concentration of cations C_p and anions C_n should satisfy the following time-dependent differential equations:

$$\frac{dC_p}{dt} = -\nabla \cdot J_p$$
$$\frac{dC_n}{dt} = -\nabla \cdot J_n$$

where J_p and J_n represent the fluxes of cation p and anion n. The fluxes J_p and J_n can be calculated as follows:

$$J_p = -D_p \left(\nabla C_p + \frac{F}{RT} C_p \nabla \phi \right)$$
$$J_n = -D_n \left(\nabla C_n - \frac{F}{RT} C_n \nabla \phi \right)$$

where D_p and D_n represent the diffusion coefficients of cation p and anion n, respectively, and F, R, and T represent the Faraday' s constant, gas constant, and temperature of the solution, respectively. When the current and ionic concentrations are steady, the fluxes of the supporting electrolyte should be zero. It follows that

$$\nabla C_p + \frac{F}{RT} C_p \nabla \phi = 0$$
$$\nabla C_n - \frac{F}{RT} C_n \nabla \phi = 0.$$

Moreover, the spatial distribution of ionic concentrations should be symmetric with respect to the origin because of the symmetry of the cathode. Therefore, the above equations can be rewritten by introducing a new variable $\tilde{r} := \sqrt{r^2 + z^2}$ as follows:

$$\frac{dC_p}{d\tilde{r}} = \frac{F}{RT} \cdot \frac{\rho I}{2\pi \tilde{r}^2} \cdot C_p$$
$$\frac{dC_n}{d\tilde{r}} = -\frac{F}{RT} \cdot \frac{\rho I}{2\pi \tilde{r}^2} \cdot C_n$$

By integrating both sides of the above equation with respect to $\tilde{r}$, the fundamental solutions of the ionic concentration of the supporting electrolytes can be derived as follows:

$$C_p = C_\infty \exp \left(-\frac{F}{RT} \cdot \frac{\rho I}{2\pi \tilde{r}} \right)$$
$$C_n = C_\infty \exp \left(+\frac{F}{RT} \cdot \frac{\rho I}{2\pi \tilde{r}} \right),$$

where C_∞ represents the bulk concentration of the electrolytes.

When the total amount of current I is about -1 nA and the bulk concentration of the electrolyte C_∞ is about 10 mM, the relative change of the ionic concentration is about 5% as shown Fig. 3.4.
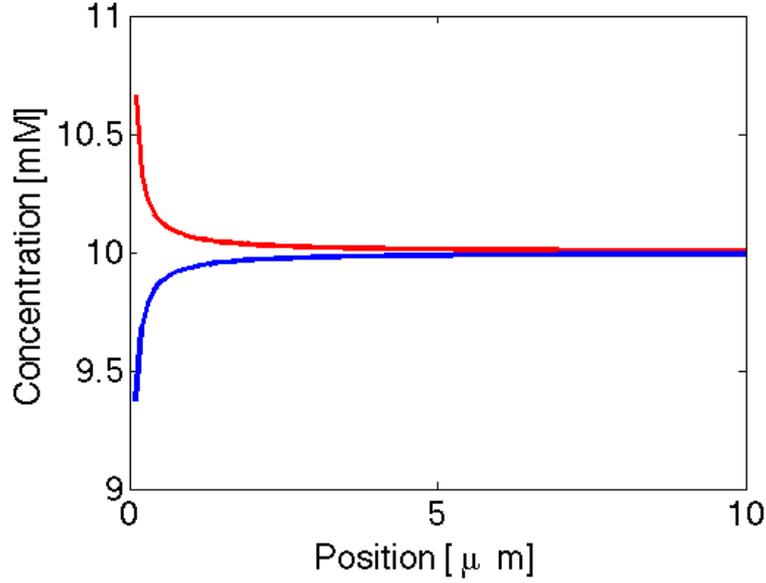
Fig. 3.4. Spatial distribution of cations and anions around the virtual cathode in 10 mM electrolyte solution. Red and blue lines mean the concentration of cations and anions, respectively.

3.2.3   Diffusion of hydroxide ions

When the anode–cathode voltage drop is sufficiently high, electrolysis of water occurs, and the following cathodic reaction is caused under neutral pH conditions:

$$2H_2O + 2e^- \rightarrow 2H^+ + 2OH^-.$$
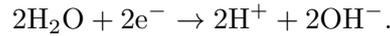
Therefore, the hydroxide ions are generated at the surface of the cathode and these ions diffuse through the solution. When the effects of electrophoresis are assumed to be neglected, the concentration of the hydroxide ions C_{OH^-} should satisfy the following diffusion equation:

$$\frac{\partial C_{OH^-}}{\partial t} = D_{OH^-}\left(\frac{\partial^2 C_{OH^-}}{\partial r^2} + \frac{1}{r}\frac{\partial C_{OH^-}}{\partial r} + \frac{\partial^2 C_{OH^-}}{\partial z^2}\right),$$

where D_{OH^-} represents the diffusion coefficient of a hydroxide ion. The boundary conditions of the above equation are as follows:

$$D_{OH^-}\frac{\partial C_{OH^-}}{\partial z} = -\frac{I}{FA} =: \varphi \quad (z = 0, 0 < r < a)$$

$$D_{OH^-}\frac{\partial C_{OH^-}}{\partial z} = 0 \quad (z = 0, r > a),$$

where $A := \pi a^2$ represents the area of the cathode.

Using Gauss's hypergeometric function, the steady-state solution of the above
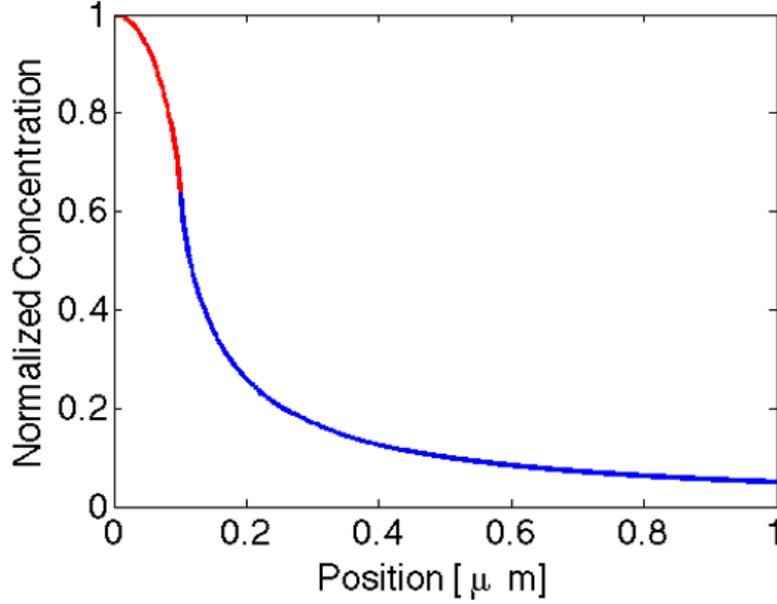
Fig. 3.5. Steady spatial distribution of the normalized concentration ($\frac{\varphi a}{D_{\mathrm{OH}}^-} = 1$) of hydroxide ions generated by cathodic reaction. Red and blue lines implied inside ($r < a$) and outside($r > a$) the virtual cathode, respectively.

equations can be described as follows [37]:

$$
C_{\mathrm{OH}^-} = \begin{cases} \frac{\varphi a}{D_{\mathrm{OH}^-}} \cdot {}_2F_1\left(\frac{1}{2}, -\frac{1}{2}; 1; \frac{r^2}{a^2}\right) & (z = 0, 0 < r < a) \\ \frac{\varphi a}{D_{\mathrm{OH}^-}} \cdot {}_2F_1\left(\frac{1}{2}, \frac{1}{2}; 2; \frac{a^2}{r^2}\right) & (z = 0, r > a) \end{cases},
$$

where

$$
{}_2F_1(a, b; c; x) = \sum_{n=0}^{\infty} \frac{(a)_n (b)_n}{(c)_n n!} x^n, \quad (x)_0 = 1, \quad (x)_n = \prod_{k=0}^{n-1}(x + k).
$$

Fig. 3.5 shows the steady-state solution of the normalized concentration ($\frac{\varphi a}{D_{\mathrm{OH}^-}} = 1$) of hydroxide ions.

The above fundamental solutions are useful in caluculating the physical parameters which depend on the electric field, pH, and ionic concentrations. These equations make it easy to couple other physical models. In Chapter 6, the fundamental solution of the electric field will be applied in calculation the deformation of soft matter.

3.3   Design of virtual cathode based on fundamental solutions

The aim of this section is to show that the above fundamental solutions can be applied to design the desired distribution of the electric field, pH or ionic concentration in two-dimensional space. As described in Section 3.2.1, the electric field induced by the Ohmic current is subject to linear partial differential equations. Therefore, the electric field induced by N virtual electrodes can be represented by the superposition of the fundamen-
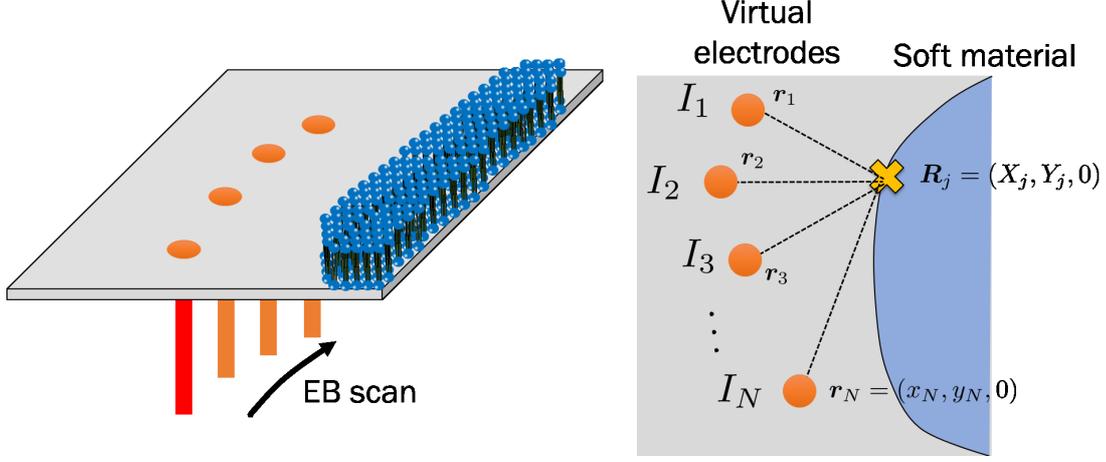
Fig. 3.6. Schematic view of generation of two-dimensional virtual cathode by scanning an EB.

tal solutions. When the i-th virtual electrode $(i = 1, 2, \cdots, N)$ is generated at position $\boldsymbol{r}_i = (x_i, y_i, 0)$, the electric field at position $\boldsymbol{R} = (X, Y, Z)$ can be represented as follows:

$$E(\boldsymbol{R}) = \sum_{i=1}^{N} G(\boldsymbol{r}_i, \boldsymbol{R}) I_i,$$

where I_i denotes Ohmic current flowing at the i-th virtual electrode and

$$G(\boldsymbol{r}_i, \boldsymbol{R}) = \frac{\rho}{2\pi \left((x_i - X)^2 + (y_i - Y)^2 + (z_i - Z)^2 \right)}.$$

On the contrary, when the value of the electric field at j-th position $\boldsymbol{R}_j$ is designated as $\hat{E}(\boldsymbol{R}_j)$ and N virtual electrodes are generated, the value of the current at the i-th virtual electrode I_i is determined by solving the following simultaneous linear equations:

$$\begin{bmatrix} \hat{E}(\boldsymbol{R}_1) \\ \hat{E}(\boldsymbol{R}_2) \\ \hat{E}(\boldsymbol{R}_3) \\ \vdots \\ \hat{E}(\boldsymbol{R}_N) \end{bmatrix} = \begin{bmatrix} G(\boldsymbol{r}_1, \boldsymbol{R}_1) & G(\boldsymbol{r}_2, \boldsymbol{R}_1) & G(\boldsymbol{r}_3, \boldsymbol{R}_1) & \cdots & G(\boldsymbol{r}_N, \boldsymbol{R}_1) \\ G(\boldsymbol{r}_1, \boldsymbol{R}_2) & G(\boldsymbol{r}_2, \boldsymbol{R}_2) & G(\boldsymbol{r}_3, \boldsymbol{R}_2) & \cdots & G(\boldsymbol{r}_N, \boldsymbol{R}_2) \\ G(\boldsymbol{r}_1, \boldsymbol{R}_3) & G(\boldsymbol{r}_2, \boldsymbol{R}_3) & G(\boldsymbol{r}_3, \boldsymbol{R}_3) & \cdots & G(\boldsymbol{r}_N, \boldsymbol{R}_3) \\ \vdots & \vdots & \vdots & \ddots & \vdots \\ G(\boldsymbol{r}_1, \boldsymbol{R}_N) & G(\boldsymbol{r}_2, \boldsymbol{R}_N) & G(\boldsymbol{r}_3, \boldsymbol{R}_N) & \cdots & G(\boldsymbol{r}_N, \boldsymbol{R}_N) \end{bmatrix} \begin{bmatrix} I_1 \\ I_2 \\ I_3 \\ \vdots \\ I_N \end{bmatrix}$$

In the above equations, it is assumed that I_i can take on any real number, but this assumption cannot be applied to the existing techniques of creating a virtual electrode because both the anode and cathode cannot be generated simultaneously and the total amount of the current is limited. To consider this restriction, the following optimization problem should be solved to calculate I_i in the case of an electron-beam induced virtual cathode:

$$\begin{aligned} minimize \quad & \frac{1}{N} \sum_{j=1}^{N} \left(\hat{E}(\boldsymbol{R}_j) - \sum_{i=1}^{N} G(\boldsymbol{r}_i, \boldsymbol{R}_j) I_i \right)^2 \\ subject\,to \quad & I_i \leq 0 \\ & \sum_{i=1}^{N} I_i \geq I, \end{aligned}$$
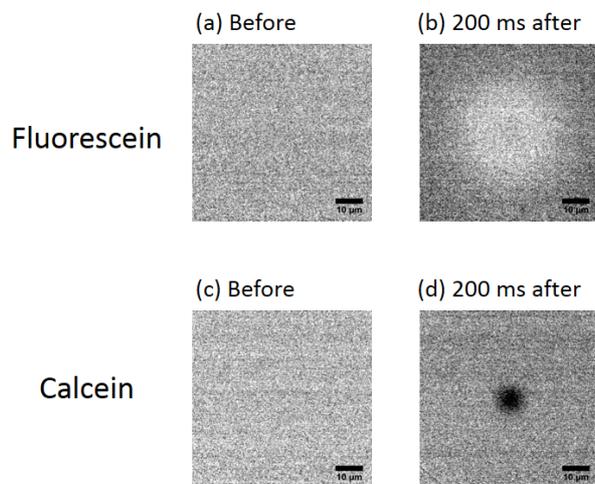
Fig. 3.7. Fluorescence images of fluorescein and calcein before and 200 ms after the EB spot irradiation.

where I denotes the maximum value of the current.

3.4   Measurements of pH and ionic concentration

To confirm the spatial expanse of the actual ionic currents and ionic shielding caused by the EB-induced virtual cathode, spatiotemporal changes of fluorescence intensities around the virtual cathode were observed in fluorescein and calcein water solutions.

3.4.1   Materials and methods

Fluorescein, NaCl, KOH, and HCl were purchased from Wako. Calcein was purchased from Tokyo Chemical Industry. Tris was purchased from Nacalai Tesque. For measurements of fluorescein and calcein water solutions, a filter cube (B-2A; Nikon, Ex: 450 nm, DM: 505 nm, BA: 520 nm) was mounted on the fluorescence microscope.

3.4.2   Results and discussion

Fig. 3.7 shows the fluorescence images of fluorescein and calcein before and 200 ms after the EB spot irradiation. The fluorescence intensity of the fluorescein increased during the EB irradiation, whereas the calcein intensity decreased. Fig. 3.8(a) shows the relative fluorescence changes of the fluorescein/NaCl/KOH solution (fluorescein: 0.5 mg/L, NaCl: 10 mM, KOH: 20 μM) after 200 ms EB irradiation; the increase in the fluorescence intensity was observed within 20 μm from the virtual cathode. This fluorescence increase was not observed in the fluorescein/Tris-HCl/KOH solution (fluorescein: 0.5 mg/L, Tris-HCl [pH 8.0]: 10 mM, KOH: 20 μM), as shown in Fig. 3.8(b). Considering the pH dependence of the fluorescence intensity of fluorescein, [38,39], the increase in fluorescence intensity around the virtual cathode exhibited proton currents. These currents are be

generated by electrolysis of water. It should be noted that the effects of photobleaching due to the scattered electrons would be small, because the fluorescence intensity of fluorescein in Tris-HCl buffer did not decrease. This would support the premise that the decrease in fluorescence intensity of rhodamine B (Section 2.3) was not due to the photobleaching but due to the temperature rise.

Fig. 3.8(c) shows the relative fluorescence change of calcein/NaCl solution (calcein: 20 mg/L, NaCl: 10 mM) after 100 ms EB irradiation, and a 0.1–0.4% decrease in the relative fluorescence intensity was observed within 3 μm from the EB spot. This decrease in the fluorescence intensity could be due to the electrical transportation of the fluorescein molecules because the fluorescein molecules are free acids and thus are negatively charged in water [40]. Additionally, the florescence intensity of calcein was almost constant between pH 5 and 9 [41]. In summary, ionic currents flowed on the scale of several tens of micrometers just after the start of EB irradiation, but the electric field was shielded within 3 μm from the virtual cathode. Since the magnitude of the electric field caused by the Ohmic currents around the virtual cathode depended on the amount of ionic currents, the spatial resolution of the electric field of the virtual cathode would become finer by lowering the beam current.

The pH increase around the EB spot would indicate that the stopped electrons within the SiN membrane could induce water splitting reaction ($2H_2O + 2e^- \longrightarrow 2OH^- + H_2$) and that some of the stopped electrons were discharged from the membrane as ionic currents. Since the water immersion lens was used in this experiment and some parts of the lens were made of aluminum, the lens might be the cylindrical anode. Considering that the working distance between the lens and the surface of the SiN was about 3 mm and the diameter of the EB-induced virtual cathode was about 120 nm [42], the spatial profile of the electric field around the EB spot was not affected by the existence of the anode(lens) in our system. Therefore the ionic current around the EB spot would flow isotropically.

3.5   Conclusion of this chapter

In this chapter, electrostatic effects of the virtual cathode were discussed. The physical setup of the virtual cathode in an electrolyte solution was formulated, and the fundamental solutions of the electric field, spatial distributions of electrolytes, and diffusion of hydroxide ions generated by cathodic reactions were calculated. Using these fundamental solutions, a design method for the virtual cathode was proposed to achieve the target electric field or ionic concentrations by solving optimization problems. Finally, it was demonstrated that an increase of pH and ionic shielding were induced around the EB-induced virtual cathode as predicted by the calculations of the fundamental solutions.
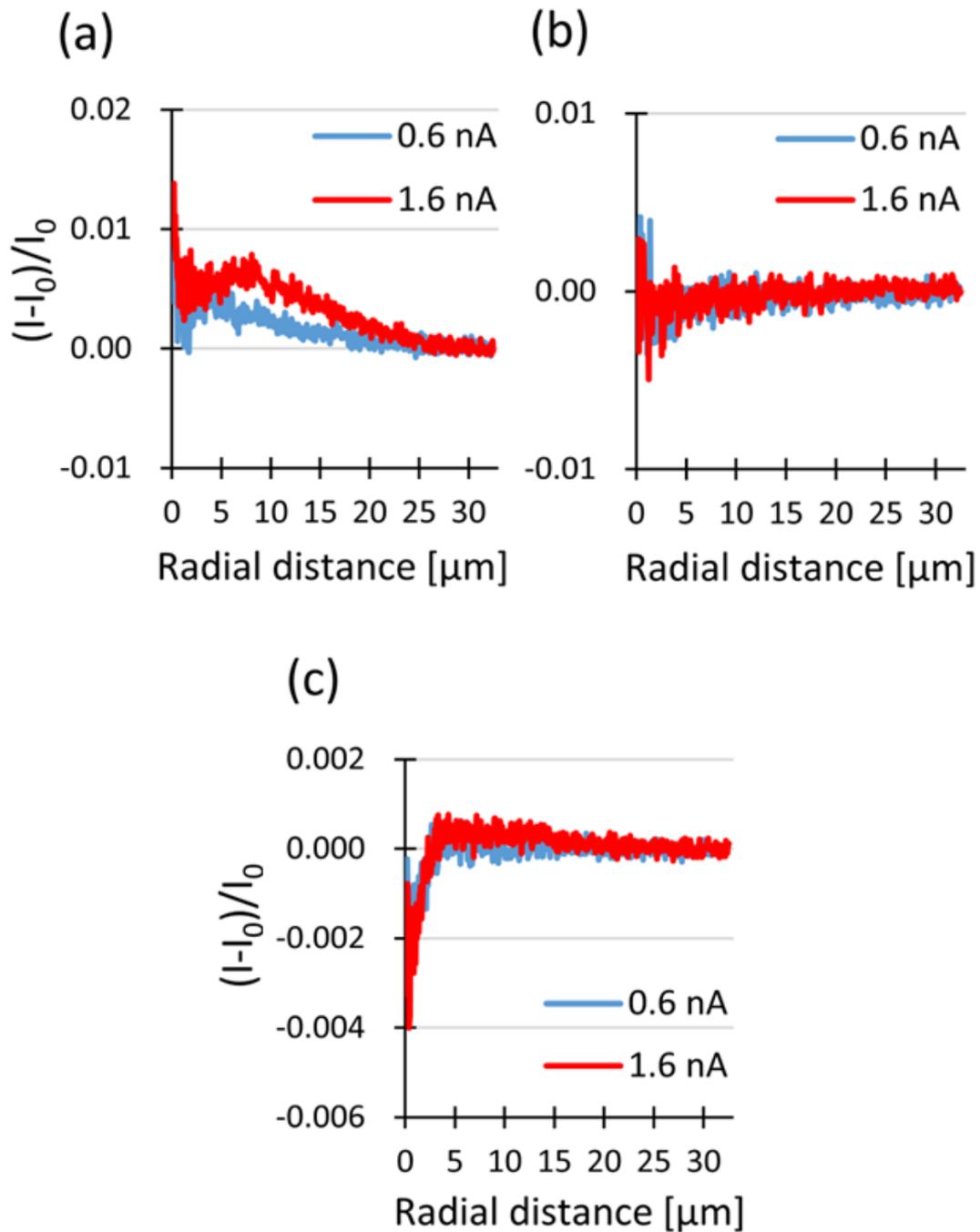
Fig. 3.8. Spatial profiles of fluorescence intensity changes in fluorescein and calcein solutions at 100 ms after the start of the EB irradiation. (a) Fluorescein/NaCl/KOH solution, (b) fluorescein/Tris-HCl/KOH solution, (c) calcein/NaCl solution. The acceleration voltage was set at 2.5 kV, and the beam current was set at 0.6 or 1.6 nA. The graph shows the average of the three experiments. I_0 indicates the fluorescence intensity at 200 ms before the EB irradiation. Photobleaching was compensated by the loss of the fluorescence intensity of the background (31.9-32.5 μm from the virtual cathode).

Chapter 4

Electrokinetic Transport Control in Nanofluidics Using a Virtual Cathode Display

In this chapter, we discuss electrokinetic phenomena such as electrophoreis and electroosmotic flow induced by the EB-induced virtual cathode. We show that the EB-induced negative charges could induce fluid flow, which was strong enough to manipulate 240-nm nanoparticles in water, and we verify that the main dynamics of this EB-induced fluid flow is electroosmosis caused by changing the zeta potential of the SiN membrane surface. Moreover, we demonstrate manipulation of a single nanoparticle,concentration patterning of nanoparticles, and dynamic control of strutures of DNA molecules by scanning EB.

4.1 Introduction

Manipulation techniques of biomolecules and cells in solutions are basic techniques for biochemical analyses. Especially, electrokinetic manipulations using electroosmosis, such as electrophoresis, dielectrophoresis or electroosmotic flow(EOF), have been widely studied and applied to lab-on-a-chip devices [43–47], because these manipulations are non-invasive and provide high-throughput. Moreover, electrical characteristics such as electrical charges or permittivity are applicable for manipulations of several types of biomolecules. However, the spatial resolution and degrees-of-freedom are restricted, since these manipulations use several electrodes fixed on an experimental system.

In order to achieve high degrees-of-freedom and resolution, hybrid opto-electrokinetic manipulation techniques [48–53] have been rigorously studied in recent years. These techniques use both electrodes and laser optics. Local illumination of light can cause a temperature rise (rapid electrokinetic patterning [48, 49]) or a change in an electric field (opto-electrohydrodynamic assembly [51] and opto-electrokinetic tweezers [52, 53]) around the illumination spot, and control of the electric field between the electrodes will enable direct and local control of fluid. By changing the illumination pattern of the light, spatio-temporal control of fluid can be achieved. These hybrid opto-electrokinetic manipulations have achieved spatio-temporal and high-throughput

manipulations of bio- and non-biomaterials [54–57], and these manipulations have been applied to immuno assay [58] and measurement of diffusion coefficient [59].

Although these opto-electric manipulation techniques have a lot of advantages as mentioned above, there are still fundamental limitations on spatio-temporal resolution. First the spatial resolution of laser optics is limited due to the diffraction of the light beams. In the case of opto-electrokinetic tweezers, the minimum size of a virtual electrode, which was generated by light illumination, was 1.52 μm when a digital micro-mirror device was used [52], and 2.8 μm when a liquid crystal display was used [60]. Second, the actual trapping region of the particles was several micrometers or more in length because the driving force of the particles or fluid exists outside the optically excited area. The rapid electrokinetic patterning [48, 49] achieved the manipulation of 2.0 to 0.1 μm particles, but the cluster size of the particles was about 5.0 to 10.0 μm. Also, the size of the trapping region by opto-electric tweezers [61] was also several micrometers or more in length. Third, the temporal resolution of optical scanning is also limited to about kilohertz order due to the mechanics of the lens. Thus opto-electrokinetic manipulations are not able to achieve control of fluid or particles at a single nano molecule level or a microsecond level. To overcome these limitations, we here apply the EB-induced virtual cathode technique to the electrokinetic manipulations.

4.2   Models: EB-induced electroosmosis

4.2.1   EB-induced electrophoresis and electroosmosis

The physical model for the generation of these EB-induced fluid flows is as follows. As shown in Chapter 2, some of the scattered electrons are charged within the SiN membrane, which is a dielectric. Since the electrons have negative charges, the atoms around the electrons are positively polarized and the atoms at the surface of the SiN membrane are negatively polarized. Therefore the negative charges are generated at the surface of the SiN membrane, and an electric field can be generated in liquid samples (Fig. 4.1 (a)). When the EB was irradiated to the SiN membrane continuously, the temporal variation of the EB-induced electric field becomes very small, and the EB-induced electric field can behave as a DC or a low-frequency electric field. Therefore, the EB-induced electric field can cause electrophoresis and EOF. When a spherical particle, which is inherently charged, exists in a liquid sample, the motion equation of the spherical particle is as follows:

$$m\ddot{\boldsymbol{r}} = \boldsymbol{F}_{\text{drag}}(\boldsymbol{r}) + Q\boldsymbol{E}(\boldsymbol{r}) = 6\pi\eta a(\boldsymbol{u}(\boldsymbol{r}) - \dot{\boldsymbol{r}}) + Q\boldsymbol{E}(\boldsymbol{r}),$$

where η represents the dynamic viscosity coefficient of water, m, a and Q represent the mass, radius and electric charge of the particle, respectively, and $\boldsymbol{u}(\boldsymbol{r})$ and $\boldsymbol{E}(\boldsymbol{r})$ represent the velocity of the EOF and the electric field induced by the EB at the coordinate $\boldsymbol{r}$, respectively. The distribution of the EB-induced electric field $\boldsymbol{E}(\boldsymbol{r})$ is modeled by Poisson equations under the condition that the scattered electrons exist in the SiN membrane (Details are shown in Appendix B). The velocity of the EOF $\boldsymbol{u}(\boldsymbol{r})$ satisfies the following
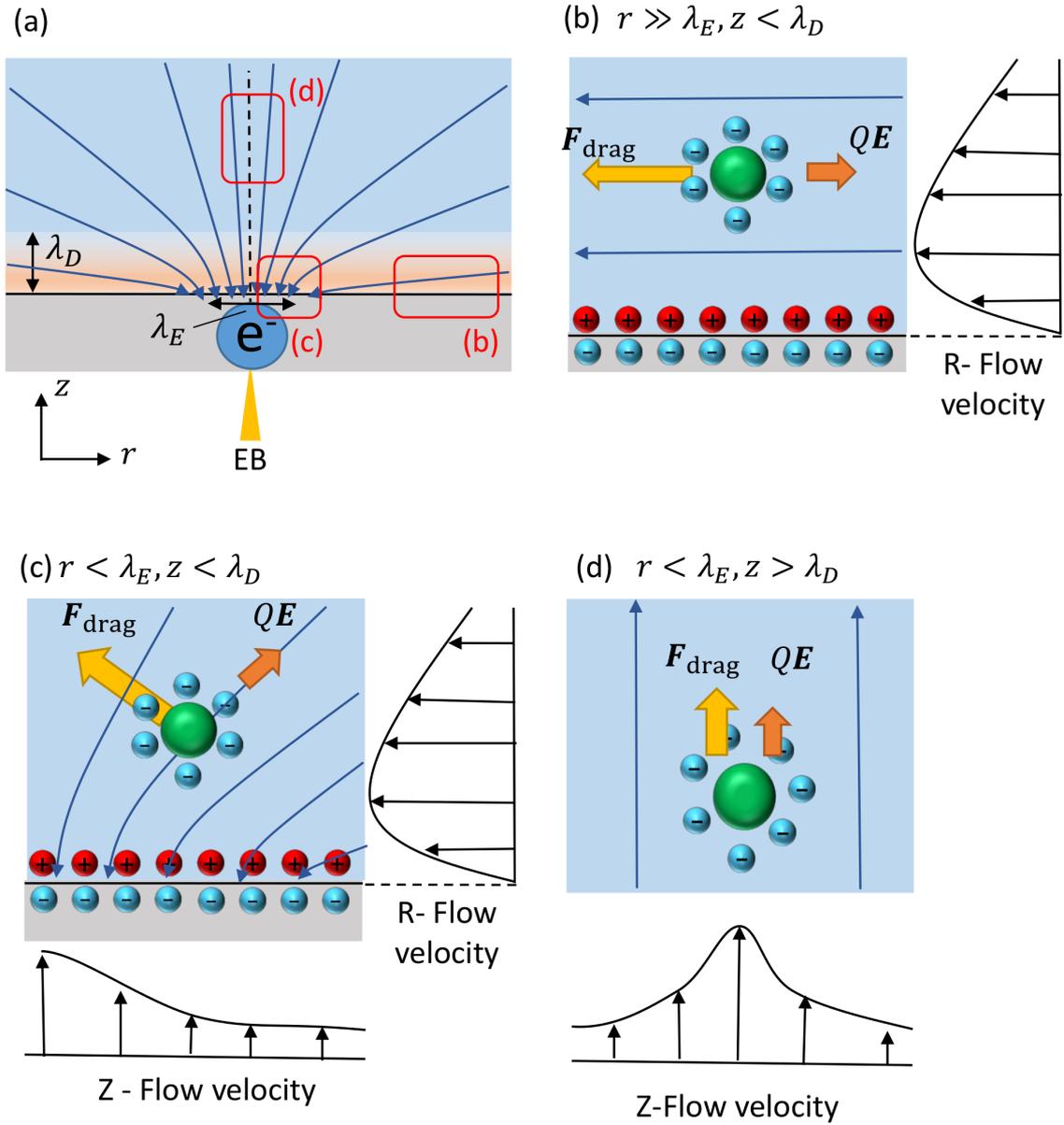
Fig. 4.1. Conceptual diagram of EB-induced virtual electrode and electroosmosis. (a) Distribution of electrical flux lines induced by negative charges of scattered electrons. λ_D and λ_E represent the Debye length of wet sample and the maximum of the radial range of the EB, respectively. (b) (c) (d) Electrical flux lines and direction of electrophoretic force ($Q\boldsymbol{E}$) and drag force of EOF (F_{drag}), provided that both the nanoparticles and the SiN membrane are negatively charged.

Navier-Stokes equation with external electrokinetic force [62] :

$$\frac{\partial \boldsymbol{u}}{\partial t} + (\boldsymbol{u} \cdot \nabla)\boldsymbol{u} = -\frac{1}{\rho}\nabla p + \frac{\eta}{\rho}\nabla^2 \boldsymbol{u} + \rho_e \boldsymbol{E}(\boldsymbol{r}),$$

where ρ, p and ρ_e represent the density, pressure and the space charge density, respectively. ρ_e is determined by the concentration distribution of cations and anions in the liquid sample, and the distribution can be modeled by Poisson-Boltzmann equation or Poisson-Nernst-Plank equation [62].

Electrophoretic force and drag force of EOF are the main driving force for manipulation of liquid samples in the proposed method. The direction of electrophoretic force is along that of the electric field, whereas the direction of drag force differs according to the position because EOF, the origin of drag force, is generated at the SiN membrane surface. For symmetry of the surface direction, the coordinate of the position $\boldsymbol{r}$ is hereafter represented in the cylindrical coordinate system (r, θ, z). In the region where r is sufficiently larger than the maximum of the radial range of EB (λ_e) and z is smaller than the Debye length of the liquid sample (λ_d) as shown in Fig. 4.1 (b), the electrical field is almost along the surface of the SiN membrane, thus the horizontal EOF, which is parallel to the SiN membrane, is generated. In the region where $r < \lambda_e$ and $z < \lambda_d$ (Fig. 4.1 (c)), vertical flows as well as horizontal flows are generated, because the EOFs are focused around EB spot and then fluid instability occurs. Due to these vertical flows, drag force and electrophoretic force are generated in the region where $r < \lambda_e$ and $z > \lambda_d$ (Fig. 4.1 (d)). It should be noted that the directions of drag force of the EOFs and the electrophoretic force depend on the surface charge of the particles and SiN membrane.

4.2.2   Simulations

In order to get the spatial distribution of scattered electrons by EB irradiation, we did Monte Carlo simulations using CASINO ver. 2.428 [63]. In these simulations, there were three layers, the vacuum layer, 100-nm-thick SiN layer and H_2O layer. An EB of 2.5 keV (beam radius, 25 nm) was irradiated from the vacuum to the SiN layer, and trajectories of scattered electrons were simulated. Detailed conditions of these simulations are described in Appendix A.

Since accelerated electrons had both kinetic and electrostatic energies and the EB kinetic energy was converted into thermal energy through the collisions of atoms, electrostatic and thermal effects induced by the EB were also simulated by the FEM simulator, COMSOL Multiphysics 4.4 (COMSOL Inc.). Electrostatics and species transport were combined to simulate the electric field profile, and heat transport and fluid dynamics were combined to simulate the temperature rise and thermal convection. Since the kinetic energy of electrons was so small (about 10 μW), we assumed that the temperature rise was slight and all the physical parameters used in the FEM simulations were spatially uniform. Detailed conditions of these simulations are described in Appendix B and C.

4.3 Materials and methods

4.3.1 Materials

To visualize the EOF, 240-nm yellow fluorescent polystyrene nanoparticles (FP-0252-2, Spherotech) were used. The nanoparticles were diluted in DI water, and 2.0×10^{-2} w/v % (Sample A) and 1.0×10^{-2} w/v % (Sample B) nanoparticle dilutions were prepared. A 1.0×10^{-1} w/v % (Sample C) nanoparticle dilution was also prepared by mixing 10 μL of 1.0 w/v % nanoparticle dilution and 90 μL of 0.1 w/v % Pluronic F-127 (Invitrogen) solution.

Two SiN membrane types were used, bare and PEI-coated. The PEI coating process was as follows. First, 10 μL of 0.1 w/v % polyethyleneimine (Sigma-Aldrich) solution was dropped using a micropipette onto a SiN membrane. After leaving this for 1 h at room temperature, the PEI solution was removed by sucking up the solution in a pipette. The SiN was washed with DI water several times and air dried.

4.3.2 Observation of nanoparticles and luminescence in EB irradiated liquid suspension

A 100 μL aliquot of Sample A was carefully dropped onto the surface of bare SiN membrane and a 100 μL of Sample B was dropped onto the surface of PEI-coated SiN membrane. Spot EB was irradiated onto each sample for 1 s, and the beam current of the EB was set at 4 nA. Fluorescent images of nanoparticles and EB-induced luminescence were acquired by the sCMOS camera. The spot EB irradiation onto Sample A was performed 3 times, and the spot EB irradiation onto Sample B was performed 10 times.

4.3.3 Two-dimensional manipulation of a single nanoparticle and patterning of concentration

We demonstrated two-dimensional manipulation of a single nanoparticle and patterning of concentration by rapid EB scans. To make it easier to observe concentration patterns of nanoparticles, a 10 μL aliquot of Sample C was dropped onto the surface of a bare SiN membrane. The beam current of the EB was set at 13 nA.

4.3.4 Two-dimensional manipulation of DNA molecules

Following previous studies [64], bacteriophage T4 GT7 DNA was dyed with YOYO-1 fluorescent dye, and then antioxidant and antifaders were added. Then, DNA and PEG#4000 (Average molecular weight: 2700-3500; Nacalai Tesque) were mixed with ultrapure water, and the final concentrations of the DNA and PEG were 35 nMbp and 2.5% (w/v), respectively. Finally, 1 mL of the sample solution was dropped onto a 100-nm-thick SiN membrane.

4.3.5   Image processing

All the images were processed using Image J (NIH). To suppress background noise, we averaged images for 1 s before EB manipulation, subtracted the averaged image from each frame of the video, and applied a 3×3 median filter to each frame of the video unless otherwise noted.

To measure flow velocity during EB irradiation, we summed up the results of each trial, suppressed background noise as mentioned above, and tracked gravity points of nanoparticles by using Move-tr/2D (Library Co.).

4.4   Results

4.4.1   Simulations of scattered electrons and their electric field in liquid sample

Fig. 4.2 (a) shows the simulated trajectories of scattered electrons; their accelerating voltage was set to 2.5 kV. Fig. 4.2 (b) shows the z-axial distribution of the scattered electrons. Only 0.03 % of the scattered electrons were transmitted to the liquid layer.

Fig. 4.2 (c) shows the electrostatic potential and electrical flux lines in the liquid layer, which were induced by the external electric field of scattered electrons in the SiN membrane. The electrical flux lines became dense around the EB spot, which means that the electric field was large. Figs. 4.2(d) and (e) show the x-axial and z-axial components of the induced electric field, where the decomposition of the electric field was represented as Fig. 4.2 (e). Each component had a peak at 100 - 200 nm, which meant that the volume force was mainly applied within 1 μm. The heat transport simulations showed that the 1 s irradiation of the 2.5 keV EB could only raise the temperature several degrees Kelvin, and the flow velocity around the wall was smaller than that of the actual flow (see Appendix C).

4.4.2   Observation of EB-induced fluid flow and SiN luminescence in DI water

Figs. 4.3(a) and (b) show time trajectories of nanoparticles (a) before and (b) during EB irrdation when the bare SiN membrane was used, and the nanoparticles moved toward the EB spot during the EB irradiation. The mean radial velocity of tracked nanoparticles was as shown in Fig. 4.3 (c). When the bare SiN membrane was used, the nanoparticles moved toward the EB spot, whereas they moved outward from the EB spot when the PEI-coated SiN membrane was used. During EB irradiation, the absolute values of mean velocity decreased monotonically over time, and moved in the opposite direction. The movement of particles returned to Brownian motion about 200 ms after the end of the EB irradiation.

In this study, the fluorescent nanoparticles were diluted using DI water, thus the background intensity of fluorescent images indicated the concentration around focal surface. The brightness within 20 μm from the EB spot decreased monotonically during
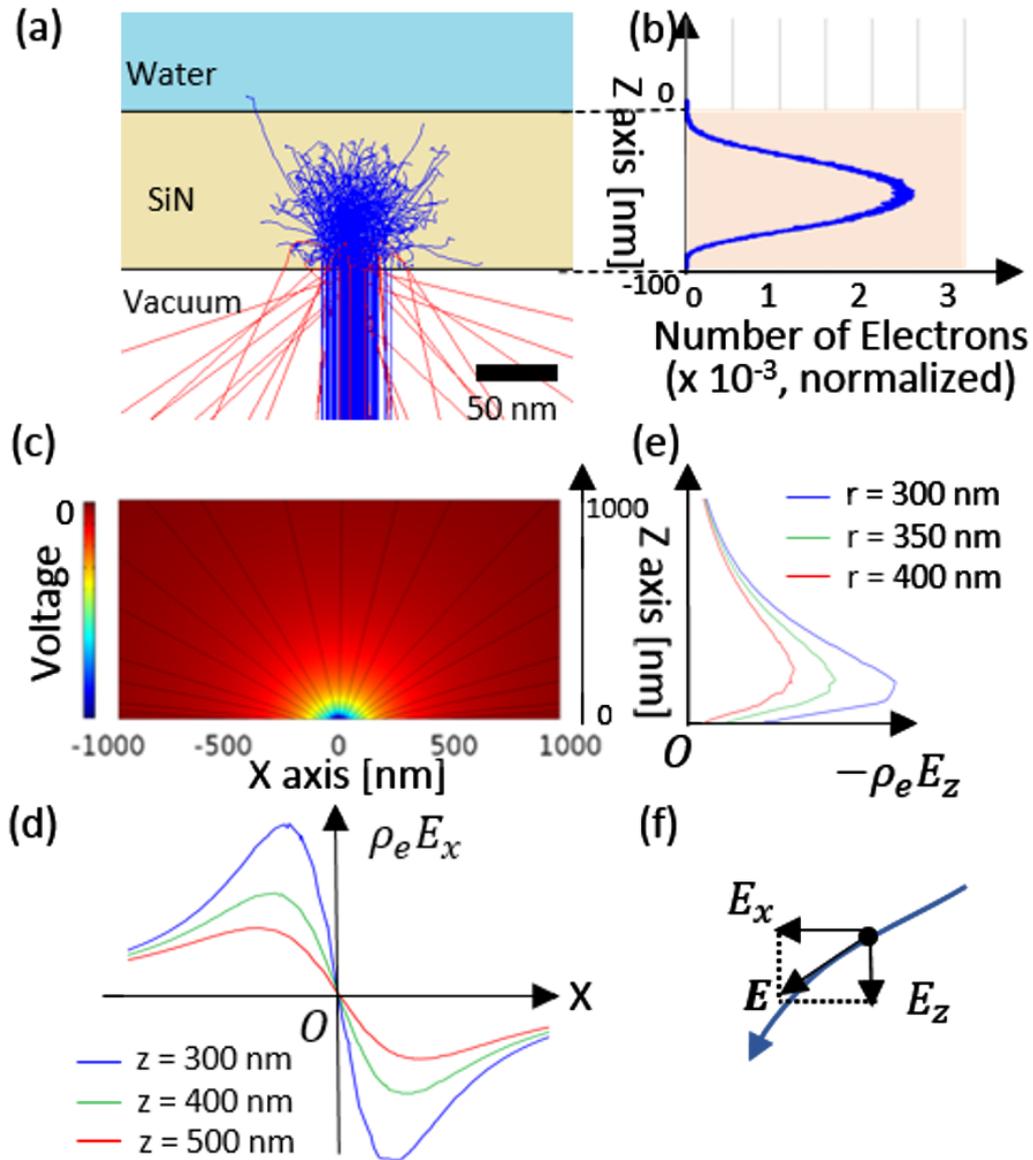
Fig. 4.2. Simulation results of scattered primary electrons and the electric field induced by the EB (X-Z plane view). (a) Simulated trajectories of scattered electrons (blue lines) and backscattered electrons (red lines) which were ejected from the vacuum space. (b) Z-axial distribution of scattered electrons (except backscattered electrons). (c) Simulated electrostatic field induced by scattered electrons. The color map represents the voltage and the black lines stand for the electrical flux lines. (d) (e) Distribution of x-axial component (d) and z-axial component (e) of volume force by EB-induced electric field. (f) Decomposition of electrostatic field.

the EB spot irradiation, which meant that the concentration around the EB spot was decreased. On the other hand, the brightness outside the 20 μm region around the EB spot did not change (Fig. 4.4(a)).

Figs. 4.4(b) and (c) show spatial dependence of the radial and tangential velocity 40 ms before and 40 ms after the start of the EB irradiation. The radial velocity decreased as a function of distance from the EB spot, whereas the tangential velocity was unchanged before and after the EB irradiation.

4.4.3   Observation of EB-induced luminescence in DI water

The intensity of EB-induced luminescence decreased over time (Fig. 4.5 (a)). The ratio of mean intensity of the luminescence to the initial intensity monotonically decreased during EB irradiation, and the luminescence was quenched just after the end of EB irradiation (Fig. 4.5 (b)).

4.4.4   Manipulation of solutes by scanning electron beam

Fig. 4.6 shows manipulation of a single nanoparticle movement. By scanning the EB triangularly, a single nanoparticle was rotated around a target point (Fig. 4.6 (a)). The coordinates of the gravity point of the tracked single nanoparticle were converted from Cartesian coordinates to polar coordinates where the origin position was set to the target point as shown in Fig. 4.6 (a), and the rotation angle was defined as the angle between the initial line of the polar coordinates and the line between the origin and the gravity point of the tracked nanoparticle. The variation of rotation angle from the manipulation was as shown in Fig. 4.6 (b). The nanoparticle was rotated counterclockwise during EB manipulation, whereas it had Brownian motion before and after EB manipulation. The scanning EB moved the single nanoparticle straightly, where the scanning angle between the direction of EB scan and the horizontal axis (θ_{obj}) was 88 deg (Fig. 4.6(c)). The absolute values of velocity and the angle of velocity are shown in Fig. 4.6 (d). The velocity peaked between 0.54 s and 0.60 s, when the difference between the angle of velocity and the scanning angle became almost zero.

Fig. 4.7 shows the spatiotemporal patterns of nanoparticle concentration by scanning "μ" and "Λ" patterns. The brightness of the scanned area decreased, and concentration patterns emerged as these letters.

4.4.5   Manipulation of DNA molecules by scanning electron beam

Spatiotemporal changes of DNA molecules in PEG#4000 water solution occurred as shown in Fig. 4.8. The acceleration voltage and beam current were set to 3.0 kV and 5.7 nA, respectively. DNA molecule (a) was in a random coil state, and it was repelled from the virtual cathode as soon as the EB irradiation started. On the other hand, molecule (b) was elongated during the EB irradiation, and split at $t =$0.9 s. Considering that all DNA molecules moved in the opposite direction of the electric field of the virtual cathode, this

repulsion of DNA molecules can be attributed to electrophoretic effects since the DNA molecules were negatively charged. Moreover, the elongation of the DNA molecule (b) due to the balance of the shear stress of the electroosmotic flow and electrophoretic repulsion force.
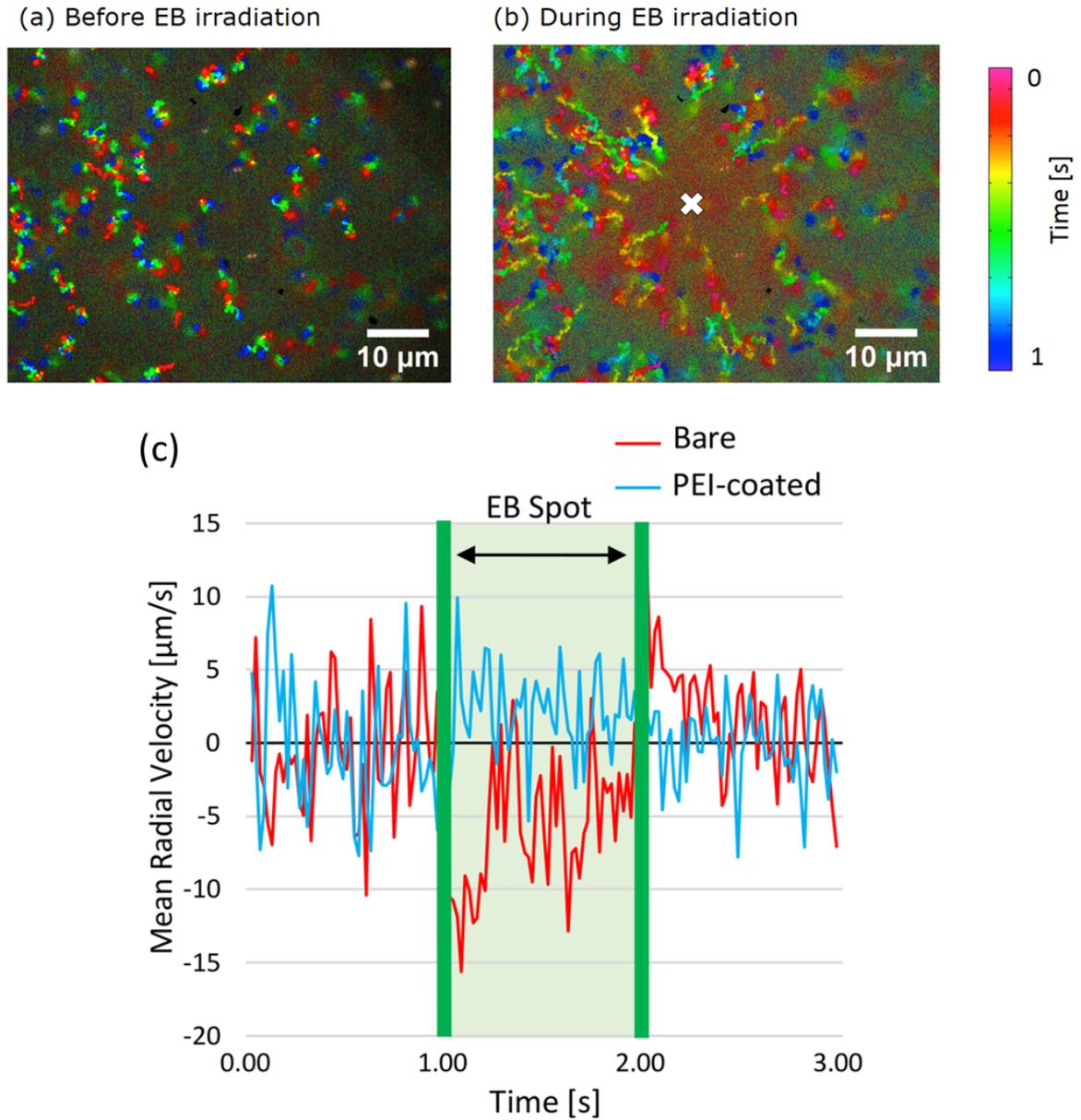
Fig. 4.3. Nanoparticle movements during EB irradiations. (a, b) Time trajectories of nanoparticles (a) before and (b) during EB irrdation when the bare SiN membrane was used. (c) Average radial velocity of 240-nm-diameter nanoparticles within 50 μm from the EB (mean $\pm$ SD (standard derivation), $n = 10$). Radial movement of a nanoparticle occurred during irradiation of the EB spot (1.0 s — 2.0 s), and its direction was reversed when the membrane had the PEI coating.
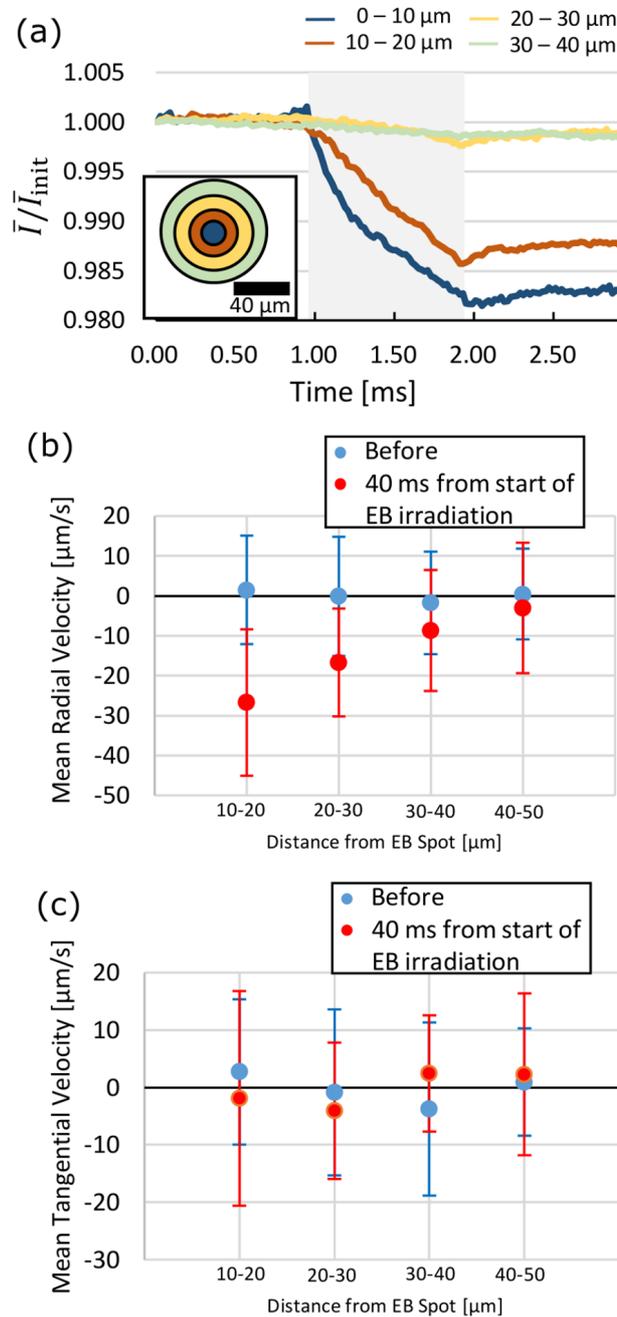
Fig. 4.4. Spatial dependency of EB-induced flow when a bare SiN membrane was used. (a) Relationship between distance from EB spot and intensity change over time. $\bar{I}$ means the averaged intensity over the area of each region, and $\bar{I}_{\mathrm{init}}$ means the initial value of $\bar{I}$ (the noise suppression was not performed). The intensity within 20 μm decreased during EB irradiation. (b) (c) Spatial dependence of the mean radial (b) and mean tangential (c) velocities 40 ms before and 40 ms after the start of the EB irradiation (mean $\pm$ SD , $n \geq 10$).
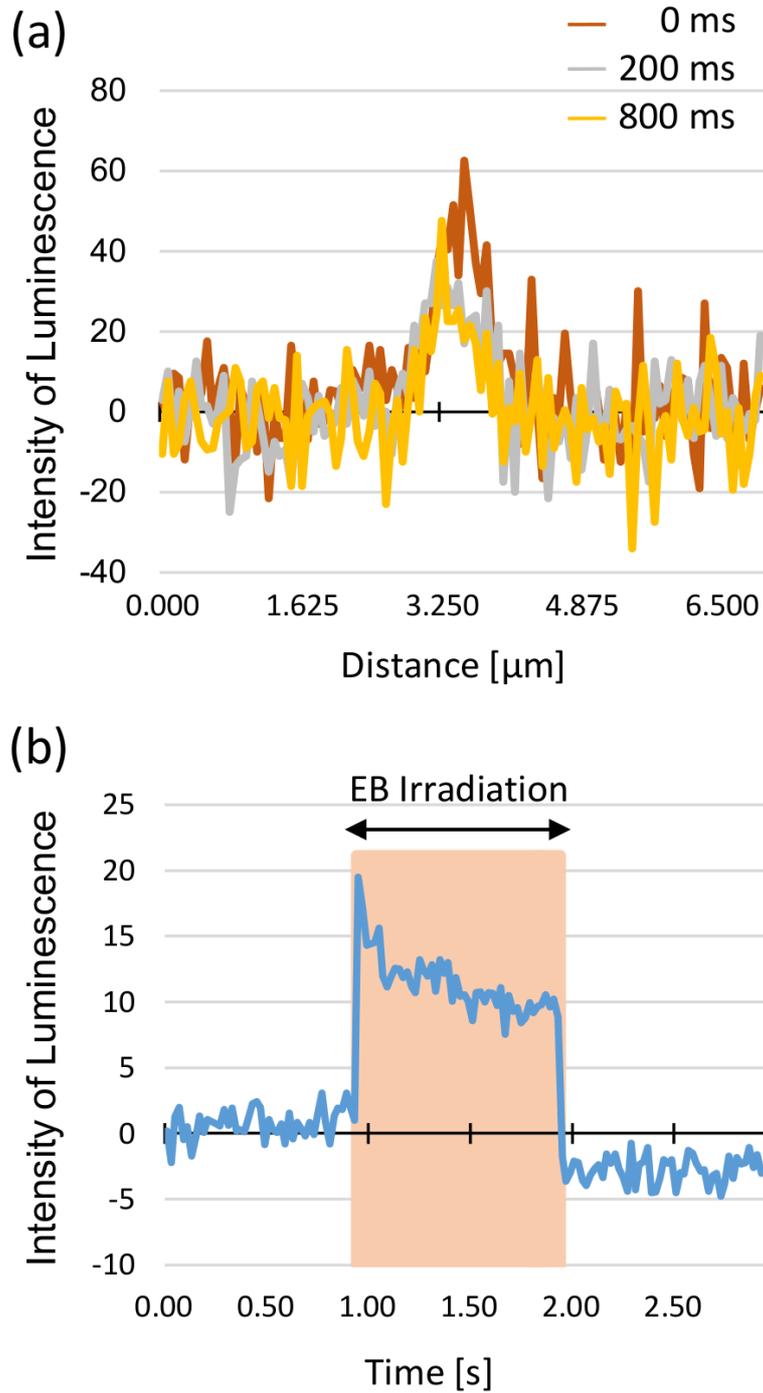
Fig. 4.5. Spatiotemporal transition of EB-induced luminescence. (a) Intensity of EB-induced luminescence after start of EB irradiation. As irradiation time passed, the height of the intensity peak decreased. (b) Averaged intensity of EB-induced luminescence within 0.5 μm from the EB spot.
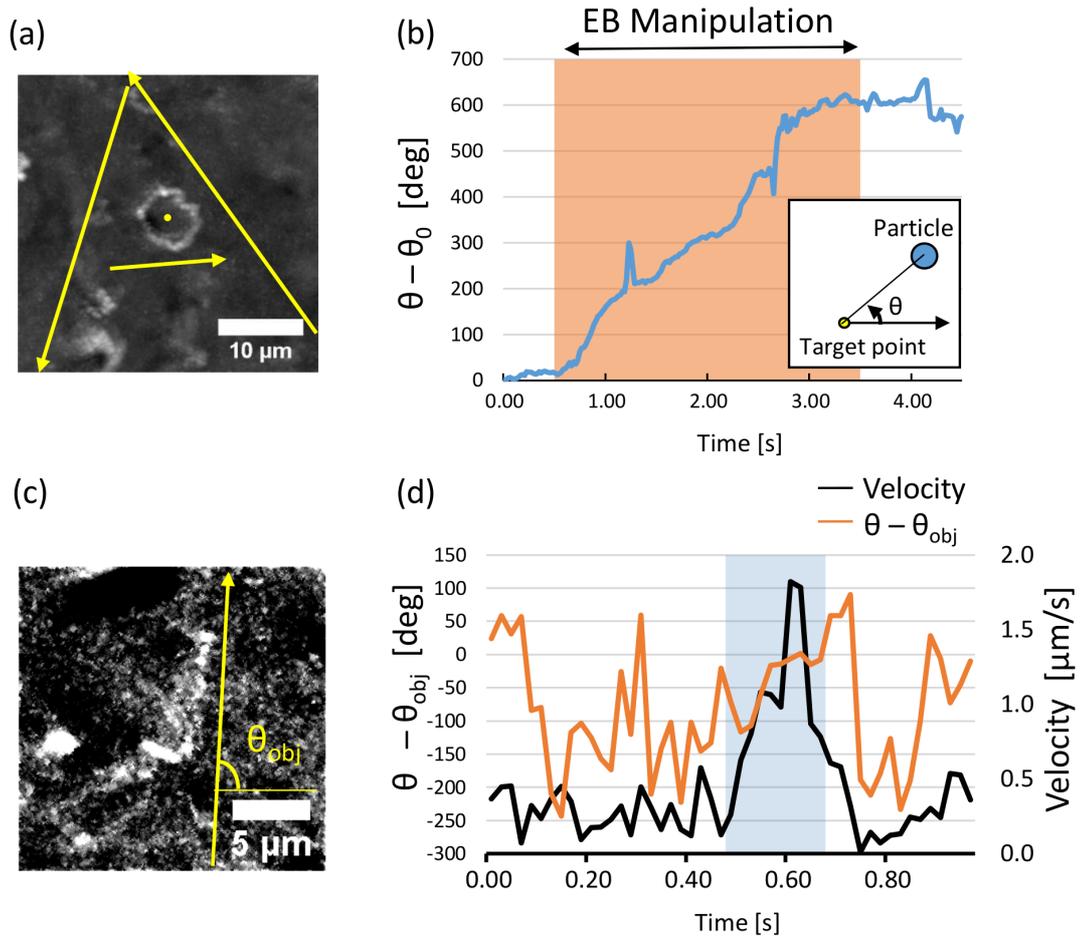
Fig. 4.6. Demonstration of rotational and translational manipulations of a single nanoparticle. (a) Trajectory of rotationally manipulated nanoparticle. Yellow circle indicates the target point of the rotational manipulation, and yellow arrows indicate the spatio-temporal pattern of the EB scan. (b) The rotation amount of the nanoparticle. When the nanoparticle was manipulated as shown in (a), the rotation amount monotonically increased. (c) Trajectory of translationally manipulated nanoparticle. Yellow arrows indicate the spatio-temporal pattern of the EB scan. (d) The error from the target angle (θ_{obj} =88 degrees) and velocity of the manipulated nanoparticle as shown in (c). The error decreased and the velocity was maximized between 0.54 s and 0.60 s.
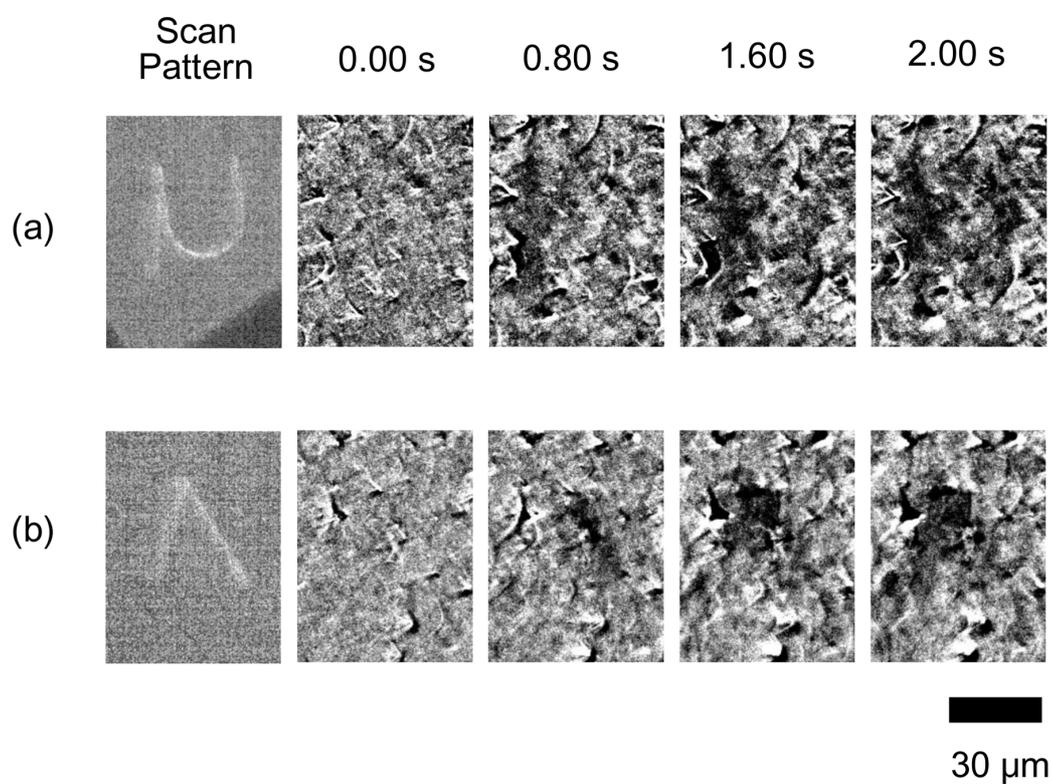
Fig. 4.7. Two-dimensional concentration patterning of (a) "μ" and (b) "Λ"shape patterns. (Left) Actual EB scan pattern. (Right) Temporal variation of fluorescence. Degradation of fluorescence was observed in the scanned area.
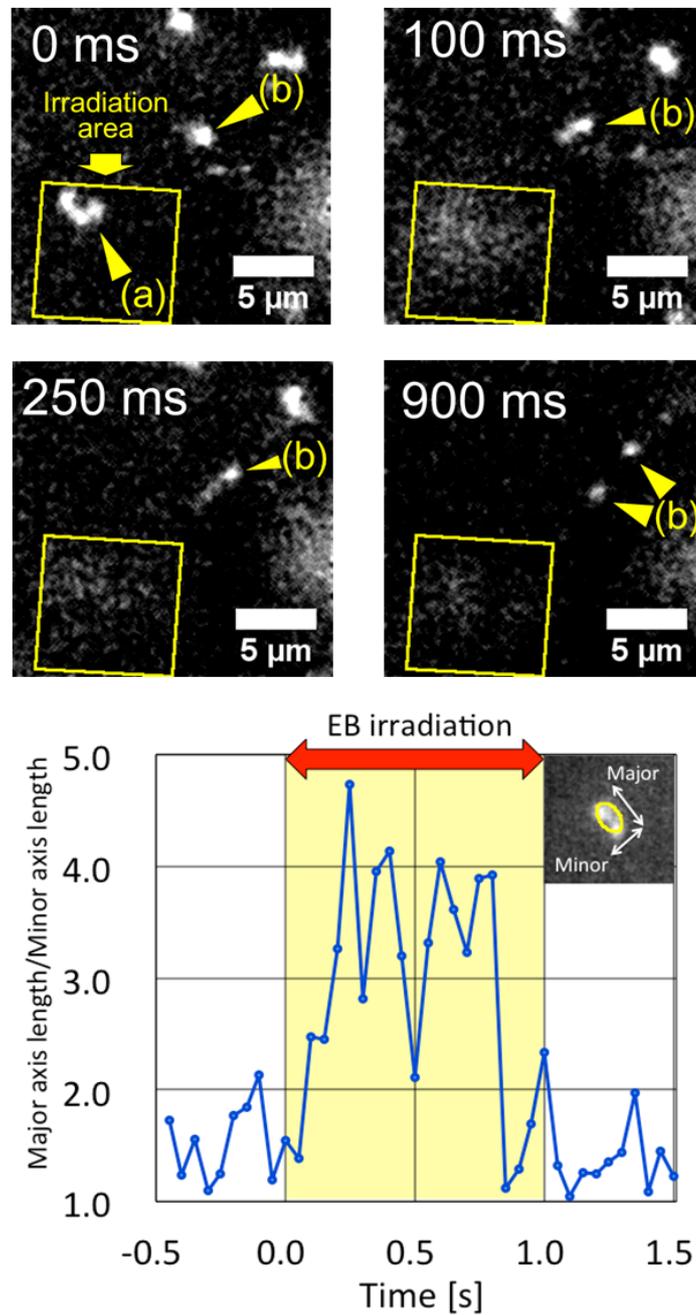
Fig. 4.8. Temporal changes of DNA molecules in PEG#4000 water solution. (Top) Time lapse images of the DNA molecules. The square virtual cathode was generated, and the yellow box indicates the irradiation area. (Bottom) Temporal change of the major axis of the DNA molecule (b). The shape of the DNA molecule was approximated with an ellipsoid using ImageJ.

4.5   Discussion

4.5.1   Existence of EB-induced EOF

In this study, we proposed a new control method and its physical model of electrokinetic transport in liquid samples by EB irradiation. The driving forces of manipulation in the proposed method were electrophoretic force and fluid drag force of EOF induced by the EB-induced virtual electrode. Actually, the radial movement of the particles and the reversing of the direction of this movement without the PEI coat on the SiN membrane surface implied the existence of EOF and ruled out the possibility that thermal convection was the main mechanism of bottom flow. Moreover the intensity decrease of particles around the EB spot implied the coexistence of EOF and electrophoresis. Besides the experimental results, the FEM simulations also supported our findings that the driving force of EOF could exist around the EB spot and the thermal convection could not affect particle transport in the observed region.

Since the zeta potential of the nanoparticles was about -4 mV (Manufacturer's information), the nanoparticles were negatively charged inherently, and were subject to electrophoretic force and the drag force of the electroosmotic flow when an electrostatic field was applied. In spite of the existence of these two forces, the drag force of EOF would be bigger than electrophoretic force around the surface of the SiN membrane according to the result that the direction of the movement of the nanoparticles was reversed when the bare SiN membrane was coated with PEI as shown in Fig. 4.3(b). The PEI coating could affect the zeta potential of the surface of the SiN membrane, which determined the direction of EOF, and could not affect the zeta potential of the nanoparticles. Therefore, the drag force of EOF would contribute to the reversal of nanoparticle movement when the PEI was coated on the SiN membrane, which indicated the drag force of EOF would be bigger than electrophoretic force. The electrophoretic force was small in the experiments, because the zeta potential of the nanoparticles was small (about -4 mV) in the experiments and the electrophoretic velocity of the nanoparticles were decelerated by the electric force applied to the excess cations (H^+) within electric double layer around the nanoparticles. If the nanoparticles are more charged, the electrophoretic effects due to the inherent charges and polarization charges due to the EB-induced electric field will become more significant. Our future work will include the details of inherent and polarization charges of highly charged nanoparticles during EB irradiation and their effects to the manipulation.

The direction of observed movement of particles was consistent with previous studies. These studies showed that the zeta potential of solid SiN in pH 7.0 aqueous solution was about -40.0 mV [65, 66], so the cations (H^+) in DI water were thought to be attracted to the bare SiN membrane when it was used, which meant that the spatial charge density ρ_e was positive near the surface of the bare SiN membrane. On the other hand, PEI is a cationic polymer [67], so the anions (OH^-) in DI water were thought to

be attracted to the PEI-coated SiN membrane when it was used, which meant that ρ_e was negative near the surface of the coated SiN membrane. The radial electric field E_r was negative, because the direction of the EB-induced electric field $\boldsymbol{E}$ was toward the EB spot. Thus the radial component of the driving force of EOF $\rho_e \boldsymbol{E}(\boldsymbol{r})$ was negative when the bare SiN membrane was used, and positive when the PEI-coated SiN membrane was used, which were consistent with the directions of actual movement of particles shown in Fig. 4.3 (b).

Since the EB-induced electric field was highly focused according to the FEM simulations, there was a possibility that cathodic reactions such as electrolysis of DI water occurred, and the anionic chemical species generated by the cathodic reactions might affect the movement of the nanoparticles during the EB irradiation. However, the effect of electroosmotic flow due to the electric field of electrons would be larger than that of the generation of anionic chemical species even if cathodic reactions had occurred during the EB irradiation, because our experiments showed the direction of particle movement was reversed when PEI was coated on the SiN membrane, and the PEI coating had nothing to do with cathodic reactions.

Therefore our results provided strong evidence supporting the physical model of the proposed method, which was based on EB-induced electroosmosis, and the possibility of manipulation of liquid samples by electrophoretic force and drag force of EOF. From the viewpoint of the manipulation mechanism, our method was quite different from that of hybrid manipulation methods using optics and electrodes [48–53], because our method could directly induce a focused electric field and easily control it. This direct control of an electric field implied that our manipulation method did not need any special coating or layer such as an indium tin oxide layer or photoconductive layer on an electrode or membrane, nor did it need a complicated control system for the optics and electrodes. Thus our manipulation method would achieve both simplicity of the experimental system and high-throughput of manipulation.

The Monte Carlo simulation results also implied that the proposed method could generate an EB-induced virtual electrode having a size of about 100 nm. This size was ten times less than that of opto-electric tweezers [52,53]. Therefore, the proposed method could be expected to achieve nanoscale manipulations of biomolecules, which would not be achievable by opto-electrical manipulations. Although the proposed method achieved the size of the virtual electrode as simulated, the experimental results showed that the nanoparticles within 30 μm from the EB spot moved in the radial direction during the irradiation. The spatial resolution of the proposed technique, however, was tens of micrometers and we could not achieved better spatial resolution than in previous studies. One of the reasons for this was the Debye length. In our paper, we used DI water as solvent in order to suppress the effect of electric shielding of ions. The Debye length of DI water is about 1 μm [62], so the range of the electrokinetic effect was large. Future work should include experiments with changes of the ion concentrations in the liquid suspension to shorten the Debye length and achieve better spatial resolution.

In our experiments, the EB was irradiated continuously, so the effect of dielectrophoresis was considered to be small. However, the FEM simulation results implied that the profile of the EB-induced electric field was non-uniform. Therefore, the dielectrophoretic force as well as electrophoretic force should be considered when the EB is manipulated at high frequency such as rapid and repeated EB scanning or blanking. Our future research will include dielectric phenomena of electron-beam manipulation and its effects on liquid samples.

Our findings indicated that the effect of electroosmosis should be considered in SEM observations for wet samples [68–71]. The accelerating voltages of these studies were higher than that in our study (2.5 keV), so the electric field generated by the scattered electrons would have induced EOF the same as in our experiments, and the fluid motion would affect the spatial resolution of images of wet samples. The SEM observation for solid materials was reported to be affected by the collisions of scattered electrons and their electrostatic force [72]. These facts implied that the effect of not only kinetic and electrostatic energies of the EB but also the EOF induced by the EB should be considered for SEM observations of wet samples to achieve better resolution.

4.5.2 Time response of EOF

The monotonic decrease of the average radial velocity and EB-induced luminescence during EB spot irradiation for 1 s implied that the strength of the EB-induced electric field, the driving force of electrophoresis and EOF would decrease. We thought that one of the reasons for this decrease was deceleration of electrons by negative charges of the SiN membrane. The negative charges of the SiN membrane induced an electric field not only in the liquid sample but also in the vacuum space, and the electrons were subjected to repulsion electrostatic force and decelerated by the EB-induced electric field, which would result in the deceleration of electrons. At the same time, the range of the EB also decreased, and thus the effect of the EB-induced electric field on the liquid sample decreased. This deceleration of electrons by charges of sample is known as "retarding" and it has been used to increase resolution of SEM images [73].

The return to Brownian motion 200 ms after the end of EB irradiation implied that the surface charge was released and there would be no external electric field due to this charge. This meant that the proposed method could easily switch the EB-induced electric field on and off at intervals of several hundreds of milliseconds. The return to Brownian motion after the end of EB irradiation, however, could have several causes. One possible cause would be the discharge of the injected electrons from the SiN membrane, such as secondary electron emission into a vacuum or leakage of current to the silicon nitride membrane and the liquid sample. This discharge of electrons would induce the change of the electric field. Another cause would be the sudden change of the electric field generated by induced-charge electroosmosis [74]. Future work should include study of the physical model for the discharge of electrons and its temporal effects on manipulation.

4.5.3 Two-dimensional control of electrokinetic transport

The proposed method achieved translational manipulation of a single particle as well as two-dimensional patterning of particle concentrations by using EB-induced electroosmosis. This meant the possibility exists for spatio-temporal manipulation of biomaterials the same as in opto-electrical manipulation methods [48–53]. Considering that the mass of electrons is very small and thus the time resolution of the EB scan can be achieved on a micro second scale, we expect that simultaneous generation of several virtual electrodes in the two-dimensional space by rapid EB scanning would be possible, and that the proposed method would provide high-throughput and more degrees-of-freedom than the opto-electrical manipulation methods [48–53].

The control rule of EB-induced electrodes, however, would be more complicated than that of the opto-electrical manipulation methods [48–53], because the EB spot generates both vertical and horizontal flows around the EB spot, and thus the trapping point cannot be generated by a simple EB spot irradiation, whereas the trapping point can be generated by the opto-electrical manipulation methods [48–53]. However, it would be possible to generate various electric field lines and stream lines of EOF by spatio-temporal arrangement of EB-induced virtual electrodes by rapid EB scanning in order to generate trapping points or get the desired control of particles. Therefore future work should include the design of an electric field by EB scanning to generate desired particle concentration patterns or to control particle movement.

4.5.4 Conclusion of this chapter

In this chapter, the electrokinetic phenomena around the EB-induced virtual cathode were investigated. We first presented a physical model of the proposed method, which was based on the electroosmosis induced by the negative charges of EBs in a SiN membrane. Second, we showed that the 2.5 keV EB could generate EOF in DI water, and that two characteristic flows could be generated, vertical flow around the EB spot and horizontal flow which was parallel to the surface of SiN membrane. These results were consistent with the presented physical model. We also showed the time-dependent behavior of the EB-induced EOF. Finally, we demonstrated applications of the proposed method to rotational and translational manipulations of a 240-nm-diameter polyethylene nanoparticle in two-dimensional space, and two-dimensional patterning of concentration of 240-nm-diameter nanoparticles. Moreover, elongation of DNA molecules was achieved by using shear stress of the EOF.

We expect the proposed method will enable both high-throughput and nanoscale manipulation of biomolecules to be achieved because of the smallness of the EB-induced virtual electrode, controllability of EOF and high response of the induced electric field.

Chapter 5

Surface Reactions of a Virtual Cathode and Their Applications to Patterning Molecules

The purposes of this chapter are to demonstrate in-situ control of surface reactions such as detachment and deposition of various molecules in aqueous solutions by EB-induced virtual cathode and to explore the main causes of detachment and deposition. To this end, an EB was irradiated onto biopolymers and sugar molecules at several accelerating voltages, and temporal changes of detachment and deposition of their molecules were observed by optical microscope. In addition, spatial distributions of scattered electrons were numerically simulated, and the main causes of detachment and deposition were determined from the results of the simulations and experiments.

5.1 Introduction

Patterning organic molecules on substrates has been one of the fundamental techniques in research fields such as biochemistry and bioengineering. [75, 76] For example, micro- and nanopatterns of proteins and biopolymers have been used for modifying cell-substrate interactions and locally controlling processes such as cell adhesion [77, 78], migration [79–81], and alignment [82, 83]. Moreover, for the dynamic control of cell adhesion, the in situ modification of a substrate in a cell culture has been achieved. [78, 80]

To pattern organic molecules on a substrate, researchers have adopted various methods, such as photolithography [9], soft lithography [10], and electron-beam lithography [84–87], and various materials, such as stimulus-responsive polymers [78, 88, 89]. Although these methods and materials have been successfully applied in the many research fields mentioned above, satisfying both the high spatial resolution and in situ controllability of patterning remains a problem to be solved. Conventional lithographic methods [9, 10, 84–87] have achieved high-resolution patterns on micro- and nanometer scales, but these patterns could not be changed after being fabricated. That is, the patterns on the substrate in a cell culture, for example, could not be changed once cell culturing was started. Stimulus-responsive polymers [78,88,89] were proposed as solutions

to the problem of controllability, but the variety of these materials was limited. Moreover, the spatial resolution of patterning was limited, since an electrode or light was used as the physical stimulus for the polymers. To overcome this limitation on the spatial resolution, we applied the EB-induced virtual cathode to patterning of organic molecules.

5.2   Materials and methods

5.2.1   Setup of virtual cathode system

A water-immersion objective lens (100x, NA=1.1, WD=2.5 mm, Nikon) was attached to the reflected-light microscope and focused on the surface of the SiN membrane. A LED white-light source (SOLA, Lumencor) was used for epi-illumination, and a polarizing unit (Nikon) and a fluorescent filter block (Ex: 540/25, Em: 605/55, TRITC, Nikon) were attached to observe samples by polarized light microscopy and fluorescence microscopy, respectively. The accelerating voltage of the EB was set at 2 to 3 kV, and the beam current was set at 4 to 13 nA. The EB was scanned on the SiN membrane in a rectangular shape. The scanning rate was 73 ms per frame.

5.2.2   Detachment of MPC polymers

To demonstrate detachment of organic molecules from the SiN membrane, the membrane was coated with 2-methacryloyloxyethyl phosphorylcholine polymers (MPC polymers) [90]. The coating procedure was as follows: 10 μL of 0.2 % (w/v) MPC polymer, that is, poly(MPC-co-n-butyl methacrylate) (PMB 30) solution in ethanol was dropped by micropipette onto a SiN membrane and left in ethanol vapor for more than 30 minutes at room temperature to volatilize the solvent completely. Then, another 10 μL of 0.2 % (w/v) MPC polymers solution in ethanol was dropped onto the SiN membrane and left in ethanol vapor for more than 30 minutes. While the coated membrane was being irradiated by the EB, 1 mL of ultrapure water was dropped onto it.

The MPC polymer was stained with rhodamine B. The staining procedure was as follows: A sufficient quantity of 0.02 % (w/v) rhodamine B (Wako Junyaku) solution in ultrapure water was dropped onto the MPC polymer-coated SiN membrane to cover it with the rhodamine B solution. After the membrane was left for several minutes at room temperature, the dye solution was sucked up by pipette, and the membrane was washed with ultrapure water several times.

5.2.3   Deposition of organic molecules

To demonstrate deposition of organic molecules, 1 % (w/v) D(+) glucose (Sigma-Aldrich) solution, 1 % (w/v) sucrose (Wako Junyaku) solution, and 0.1 % (w/v) polyethyleneimine (Sigma-Aldrich) solution were prepared. 1 mL of 1 % (w/v) glucose solution, 1 mL of 1 % (w/v) sucrose solution, and 600 μL of 0.1 % (w/v) polyethyleneimine (PEI) solution were dropped onto each bare SiN membrane. The deposition was observed by polarized

light microscopy (crossed-Nicols).

5.2.4   Monte Carlo simulation of transmission of electrons

The scattering process of electrons at accelerating voltages of 2 to 3 kV was simulated, and maximum range of electrons was estimated by using a Monte Carlo simulator, i.e., CASINO ver. 2.48 [63]. The geometrical and material setups of the simulations are shown in Fig. 5.1(a). In each simulation, 10^7 electrons were simulated, and each electron was simulated until its kinetic energy dropped below 50 eV.

5.3   Results

5.3.1   Simulation of scattered electrons

Simulated z-axial maximum ranges of scattered electrons (excluding backscattered electrons), under accelerating voltages of 2.0, 2.5, and 3.0 kV, are shown in Fig. 5.1(b). When the accelerating voltage was set at 2.0 kV, no electrons could reach the water layer. On the other hand, some electrons could reach the water layer when the accelerating voltage was set at 2.5 and 3.0 kV, and the number of electrons transmitted to the water layer increased as the accelerating voltage increased. The ratio of transmitted electrons to total injected electrons was shown in 5.1(c).

5.3.2   Observation of detachment of MPC polymers

Fluorescent images and average-intensity profiles of the MPC polymer-coated SiN membrane after it was scanned with the EB for 5 s are shown in Fig. 5.2(a). The fluorescence intensity of the EB-scanned area decreased compared with that of the unscanned surrounding area, and the boundary between the scanned and unscanned areas shows a sharp decrease in fluorescence intensity. The decrease in fluorescence occurred when the membrane was irradiated with EBs with accelerating voltages in the range of 2.0 to 3.0 kV, as shown in Fig. 5.2(b). In these experiments, the beam current was set at 4 to 5 nA. It is noted that the membrane was stained with rhodamine B after the EB irradiation; thus, the primary electrons of the EB did not give any chemical effects to the rhodamine B molecules.

 The temporal change of the MPC polymer-coated membrane during EB scanning is shown in Fig. 5.3(a). The membrane was stained with rhodamine B before being irradiated by the EB, and the accelerating voltage and beam current were set at 2.5 kV and 13 nA, respectively. Spatiotemporal change of the ratio of average fluorescence intensity to the initial value is shown in Fig. 5.3(b). In the 5-μm-square scanned area (inner area), average fluorescence dropped by 9 % after 5-s EB scanning, and it then recovered after over 40 s. Average fluorescence intensity outside the scanned area (outer area) also decreased, but it recovered after only 10 s, and its final value was 1.3% less than the initial value. It is noted that fluorescence intensity of rhodamine B decreases
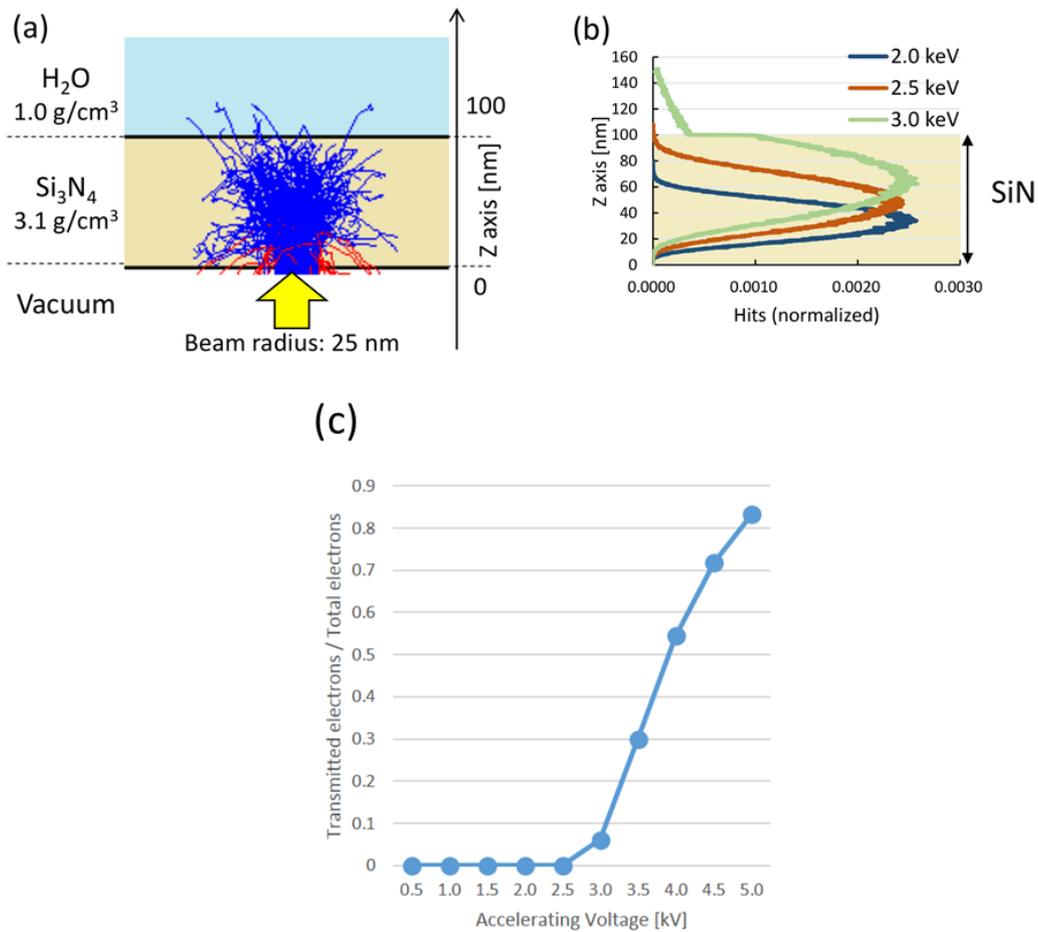
Fig. 5.1. Monte Carlo simulations of scattered electrons with various accelerating voltages. (a) Simulation conditions for scattered electrons. (b) Maximum range of scattered electrons with acceleration energies of 2.0, 2.5, and 3.0 keV. The 2.0-keV EB could not reach the water layer, whereas the 2.5- and 3.0-keV EBs could reach the water layer. (c) Ratio of transmitted electrons to total injected electrons

as temperature rises [35, 91], and that temperature rise of water around an EB spot was confirmed as shown in Chapter 2; thus, the decrease in the fluorescence intensity outside the scanned area would be due to the temperature rise and would have little to do with the detachment of MPC polymers.

5.3.3   Observation of deposition of sugars and PEI polymers

When a 2.5-keV EB was irradiated onto the 1%-glucose solution and the 1%-sucrose solution, some depositions on the SiN membrane were observed. Temporal change of bright-field images before and during the 5-s EB irradiations onto the ultrapure water, glucose, and sucrose solutions are shown in Fig. 5.4(a). The beam current was set at 13 nA. Temporal variations of mean brightness within 9.75 μm from the center of the

scanning area are shown in Fig. 5.4(b). The brightness of the SiN membrane monotonically decreased when the ultrapure water was used. On the other hand, when glucose and sucrose solutions were used, the brightness of the SiN membrane decreased from 1 to 3 s and then increased from 3 to 5 s.

When 2.5- and 3.0-keV EBs were irradiated onto 0.1% PEI solutions, some depositions were also observed. Bright-field images before and after the 5-s EB irradiations are shown in Fig. 5.5(a), and temporal changes of the ratio of brightness to initial values are shown in Fig. 5.5(b). The beam current was set at 4 to 5 nA. In the cases of irradiation by 2.5- and 3.0-keV EBs, the brightness of scanned area decreased, whereas in the case of irradiation by a 2.0-keV EB, it stayed almost the same as the initial state. The decrease of brightness during 3.0-keV EB irradiation was twice as much as that during 2.5-keV EB irradiation.
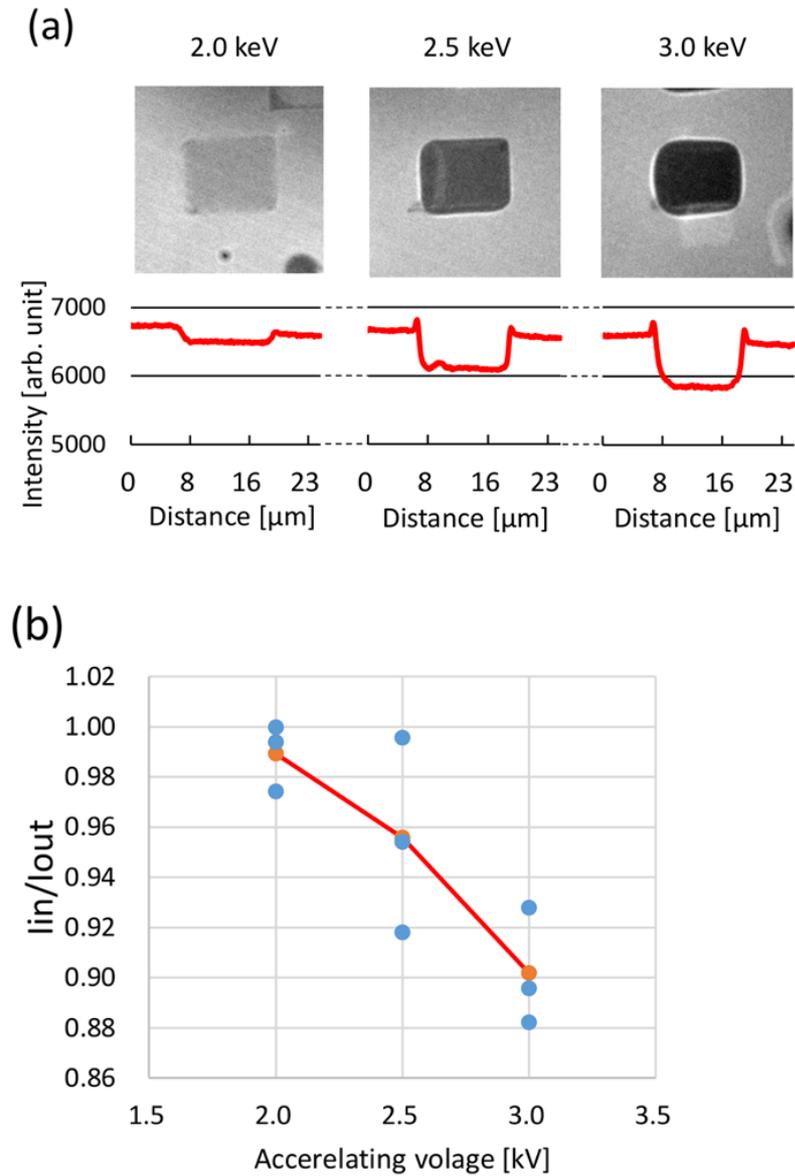
Fig. 5.2. Decrease in fluorescence intensity of rhodamine B on MPC-coated SiN membrane after EB irradiation. (a) Fluorescent images (top) and average intensity profiles (bottom) after 2.0- to 3.0-keV EB irradiations. (b) Relationship between accelerating voltages and intensity ratios of scanned area (5-μm square) to unscanned area (14- to 16-μm square). I_{in} and I_{out} are average intensities of the scanned area and unscanned area, respectively. The red line indicates average trial values for each accelerating voltage.
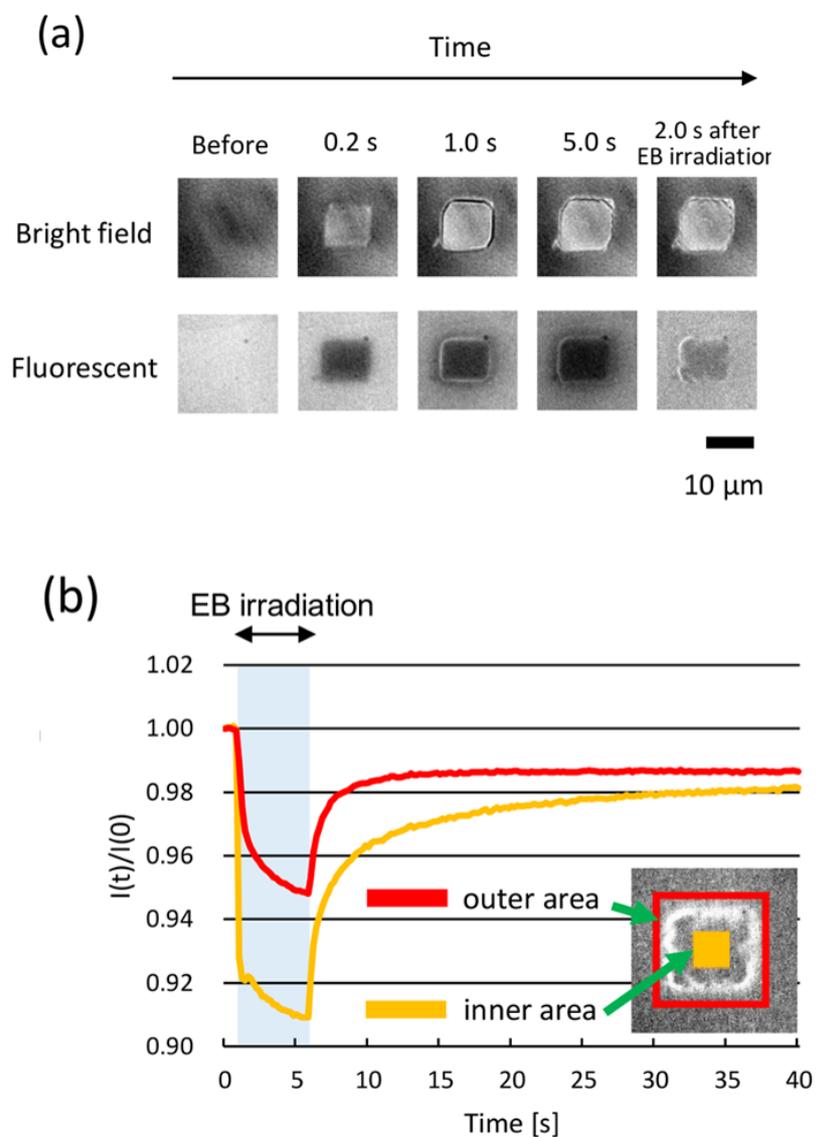
Fig. 5.3. Spatiotemporal changes of the surface of MPC-coated SiN membrane during EB irradiations. (a) Time-lapse images of MPC-coated SiN membrane during and after EB irradiation; bright-field (top) and fluorescence (bottom) microscopy. (b) Temporal changes of average fluorescence intensity of inner area (5-μm square) and outer area (14- to 16-μm square). $I(t)$ is average fluorescence intensity over the region at time t.
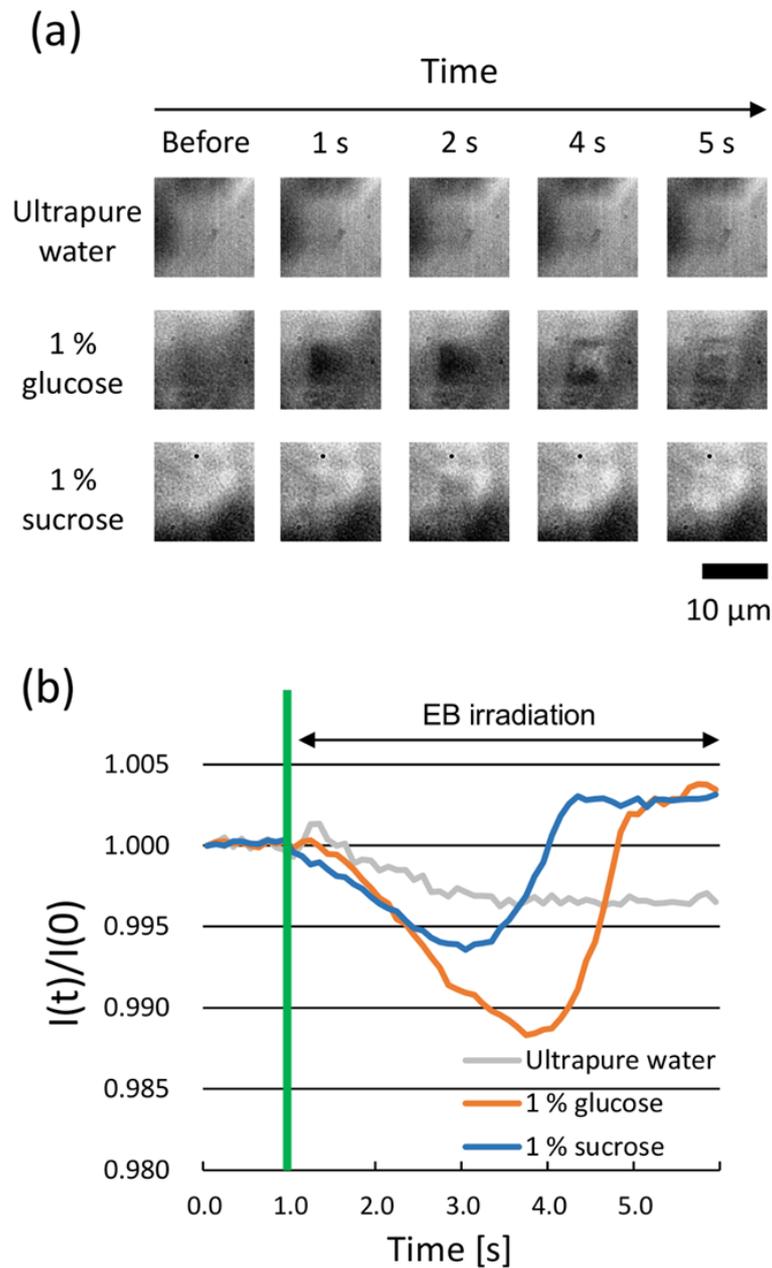
Fig. 5.4. Spatiotemporal changes of the surface of a bare SiN membrane during EB irradiations onto ultrapure water, glucose, and sucrose solutions. (a) Time-lapse images of deposition of sugars during EB irradiations in bright-field microscopy. (b) Temporal changes of average gray values of 9.75-μm square region from the center of the scanning area. $I(t)$ is the average gray value over the region at time t.
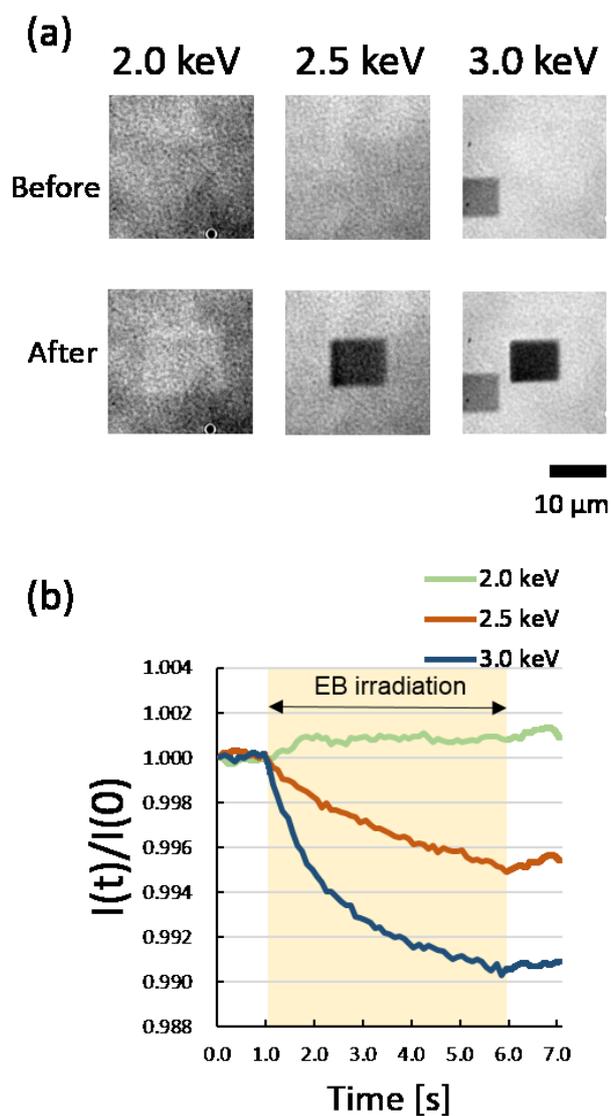
Fig. 5.5. Spatiotemporal changes of the surface of a bare SiN membrane during EB irradiation onto a PEI solution. (a) Bright-field images before and after 2.0 to 3.0 keV EB irradiations onto a PEI solution. (b) Temporal changes in average gray values of the acquired images. $I(t)$ is the average gray value at time t.

5.4   Discussion

5.4.1   Detachment phenomenon and electric field of an EB

The experimental results presented in Section 5.4.2 showed that 2.0- to 3.0-keV EB irradiation could decrease fluorescence intensity of rhodamine B stained on MPC polymer layer. This decrease in fluorescence intensity of the EB-scanned area implies that the EB irradiation reduces the density of MPC polymers, since the fluorescence indicates the density of MPC polymers on the SiN membrane. It is therefore concluded that the MPC polymers coated on the SiN membrane can be detached by EB scans. Moreover, the fluorescence intensity was shown to temporally recover, possibly due to migration of MPC polymer chains and rhodamine B molecules, and re-adsorption of rhodamine B molecules in water to remaining MPC polymers. This phenomenon, however, needs to be clarified through further studies.

   According to Chapters 2,3 and 4, at least three possibilities can be raised for the detachment phenomenon of MPC polymers: (1) electrical effects of the electric field induced by trapped electrons, (2) chemical reactions due to primary electrons of an EB, and (3) temperature rise by scattering of accelerated electrons. However, the latter two possibilities can be ruled out for the following reasons. In consideration that even a 2.0-keV EB can decrease fluorescence intensity, as shown in 5.2, the detachment of MPC polymers cannot be due to the chemical effects of accelerated primary electrons of an EB because the Monte Carlo simulations demonstrated that primary electrons of a 2.0-keV EB cannot be transmitted to a water layer (Fig. 5.1(b)). In addition, the numerical simulations (Appendix C) showed that 1-s EB irradiation only raised the temperature of the substrate and liquid sample 3 to 4 degrees Kelvin when accelerating voltage and beam current were 2.5 kV and 4 nA, respectively.

   In light of the results described above, the detachment of MPC polymers is supposed to be due to the electrical effects of the EB (such as electrophoresis or concentration of cations). It would be possible to deform polymer chain entanglements in MPC polymer layer by the electric field of trapped electrons within the SiN membrane. This change of intermolecular interactions would be one of the reasons for the detachment of MPC polymers. However, the magnitude of electrical effects of an EB compared to other intermolecular interactions (such as van der Waals forces or hydrophobic forces [92]) remains a question. In the case of MPC polymers, strong attraction forces are exerted between the polymers and the SiN membrane, because the polymers have a hydrophobic part, and the surface of the SiN membrane is also hydrophobic. Electrical effects of an EB could change ionic interactions between the polymers; however, it was unclear from our results whether the electrical effects of an EB surpassed the strong hydrophobic interaction between the MPC polymers and the SiN membrane. Accordingly, future studies should focus on the relationship between the electrical effects of an EB and other intermolecular interaction

forces.

The proposed detachment method could be applied to other polymers and organic molecule. Considering that the previous research achieved EB manipulation of living cells in cell culture [93, 94], it would be possible to fabricate a cell-adhesion area in cell culture in-situ by detaching adsorbed molecules on a SiN membrane with EB scans. Moreover, it would be possible to detach molecules on the nanoscale in electrolyte solutions such as cell media because of the Debye shielding by concentration of cations.

5.4.2   Deposition phenomenon and primary electrons of an EB

The experimental results presented in Section 5.4.3 showed that some depositions were generated by 2.5- to 3.0-keV EB irradiations, and that the patterns of brightness of the depositions differed. Since the samples contained only ultrapure water and organic molecules, it is supposed that the depositions were made from the organic molecules in the samples. Moreover, a 2.0-keV EB could not generate depositions made from PEI. Since the numerical simulations showed that primary electrons of a 2.0-keV EB could not be transmitted to the water layer, the deposition phenomenon possibly has a relation with the transmission of primary electrons into the water layer. It is therefore supposed that the deposition phenomenon is due mainly to the chemical reactions induced by the primary electrons of the EB rather than the electrical effects of the EB. The chemical reaction induced by EB irradiations could be explained by previous researches [84–87]. For example, it was reported that low-energy electrons could cause crosslinking reactions of poly(ethylene glycol) (PEG) polymers on a silicon surface by EB irradiation [84, 85]. Similar crosslinking reactions would be generated in the EB system used in the current study, since the transmitted and secondary electrons stopped around the interface between a water layer and a SiN membrane according to the numerical simulation (Fig. 5.1(b)). The details of the chemical reactions induced by an EB will be studied in future studies.

It is concluded from the above discussion that the proposed technique for depositing PEI polymers, which have been used for biochemical techniques such as cell adsorption [95], immobilization of enzymes [96] and gene delivery systems [97], can therefore be applied to fabrication of polymer deposition in solutions for in-situ biochemical analysis. In addition, it would achieve about 120 nm resolution according to our previous studies of the deposition made from EDOT. [94] Therefore, the proposed technique would achieve both of in-situ and nanometer scale fabrication of cell scaffolds in cell culture, which could not be achieved by the previous studies of conventional lithographic methods [9, 10, 84–87] and stimuli-responsive polymers [78, 88, 89]. However, the physical and chemical properties of the depositions are still unknown; thus, further studies are needed to determine these properties and to apply them to biochemical analysis. To this end, our future studies will include measuring physical features such as thickness and elasticity and chemical features such as composition, binding energy, and functionality as organic molecules.

5.5   Conclusion of this chapter

In this chapter, we demonstrated surface reactions such as detachment and deposition of various molecules in aqueous solutions. MPC polymers were detached from a SiN membrane, and glucose, sucrose, and PEI polymer molecules were deposited on the membrane in water by EB irradiation. In addition, the results of experimental and numerical simulations suggest that the detachment phenomenon of MPC polymers is due to the electrical effects of the EB and that the deposition phenomenon of the PEI polymers is due to chemical reactions induced by kinetic energy of the EB. Therefore, these two surface reactions could be controlled by changing acceleration voltages. It is expected that the proposed method of the detachment and deposition of organic molecules will be applied for in-situ fabrication of cell scaffolds or biochemical analysis on the nano-meter scale.

Chapter 6

Electromechanical Control of Lipid Membrane Morphology and Domains

6.1 Introduction

Surfaces of living cells are made of lipid bilayers that have some important roles to maintain cell activities. For example, lipid bilayers separate a cell from the outer environment and maintain concentrations of ions and molecules by passive and active transportation of water, ions, and small molecules using membrane proteins such as ion channels and pumps. It is thought that lipid molecules and membrane proteins on the membrane are not distributed uniformly but localized by forming domain structures called as "lipid rafts." Moreover, cell membranes can be easily deformed by a cytoskeleton such as actin filament, because the membranes have fluidity. Therefore, studies on lipid rafts and mechanical properties of lipid bilayers are very important to understand the mechanism of various self-assembled structures of living cells. For these studies, manipulation techniques of lipid bilayers have been widely studied as follows.

6.1.1 Mechanical measurements of lipid bilayers

To study the viscoelasticity of lipid bilayers, micropipette aspiration of giant vesicles [98,99] and optical or optoelectric tweezers [23–26] have been used. These techniques have enabled average viscoelastic features of vesicles, since applied forces to the lipid membrane can be analytically calculated (micropipette aspiration) or can be easily measured (optical tweezers). However, these techniques are not suitable for spatiotemporal dependencies of the viscoelasticity. In case of micropipette aspiration, a micropipette is fixed, and control of the aspirated area of the target vesicles is difficult. In case of optical tweezers, attachment of microbeads is needed since the trapping force of lipid molecules is low, and spatially selective control of the attachment is difficult. In addition, previous techniques cannot be used to achieve operando analysis of mechanical properties such as pH or electrical stimuli.

6.1.2   Formation and patterning of solid supported lipid bilayers

To study membrane proteins and lipid rafts, solid supported lipid bilayers (SLBs) [100] as well as vesicles have been used, since reproducibility and size control of vesicles are difficult and plane structures are useful for quantification by fluorescence microscopy and atomic force microscopy. For fabrication of solid supported lipid bilayers, vesicle fusion techniques and self-spreading techniques [101–103] have been established. Many researchers have achieved various measurements such as membrane electrophoresis for separation of membrane protein [104–106], observation of lateral diffusion of a single molecule on a SLB [107], observation of reaction-diffusion waves in Min protein systems [108], and so on. Especially, self-spreading techniques have achieved measurements of temporal dynamics of intermolecular interactions such as fluorescence resonance energy transfer.

For large-scale measurements, the patterning techniques of SLBs have been also studied. Photolithography [109]; soft-lithography, such as micro contact printing [110] and dip-pen nanolithography [111]; and lasers [112, 113] have been applied to achieve the patterning of SLBs. However, these patterning methods can achieve only static patterning. To achieve temporal or spatial measurements of dynamics on SLBs, dynamic patterning and spreading control of self-spreading SLBs are needed.

6.1.3   Objectives of this chapter

As described above, dynamic control techniques of lipid membranes are needed to carry out spatiotemporal measurements and operando analysis of lipid membranes. To control a two-dimensional flow of the lipid membrane, the following manipulations are necessary:

1. Patterning the lipid membrane to control the existence area of the lipid membrane;
2. Controlling the surface energy of the SiN membrane to change the spreading speed of the SLBs;
3. Exerting stress on the SLBs to deform their edges.

The objective of this chapter is to demonstrate that the EB-induced virtual cathode can achieve the above three manipulations of lipid membrane, and to apply the EB-induced virtual cathode to the directed self-assembly of the morphology and domains of the artificial lipid membrane.

6.2   Physical models of self-spreading supported lipid bilayers

Self-spreading SLBs are generated as shown in Fig. 6.1. First, a solid support, such as glass, is hydrophilized by a piranha solution, and dried lipid film is spotted on the solid using a glass capillary. Then, water solution is statically dropped on the solid. If the surface energy between the water solution and the solid is lower than surface energy between the SLB and the solid, lipid bilayers start spreading spontaneously, and an SLB
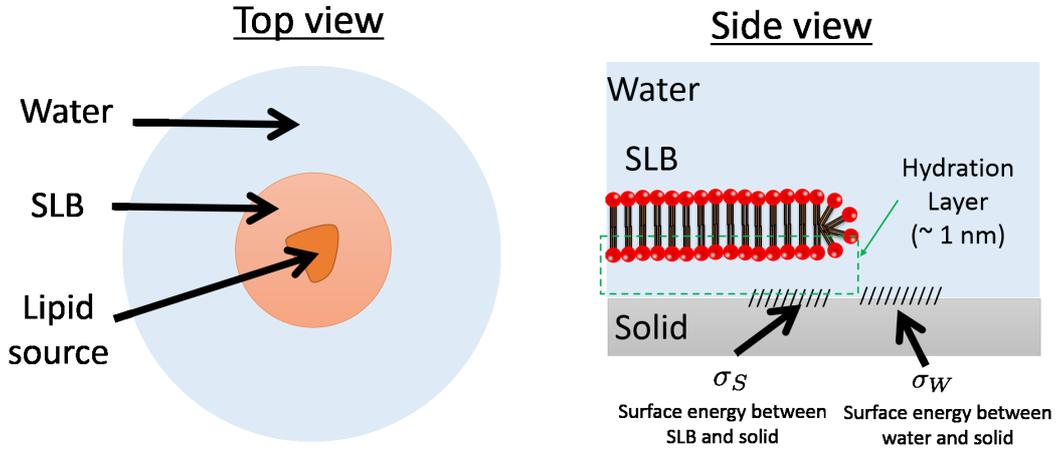
Fig. 6.1. Schematic view of self-spreading supported bilayer.

is generated on the solid. SLBs are usually visualized by attaching fluorescent molecules. Single and stacked bilayers can be distinguished by the discretized peaks in the histogram of the fluorescence intensity [102] or the increase of the fluorescence intensity at the edge of the membrane. There is a 1 nm gap between the SLB and the solid support called as "hydration layer," which is formed due to the hydrophilic surface and the hydrophilic head groups of the lipid molecule. [114, 115] Spreading phenomena of SLBs depend on ionic strength of the water solution due to repulsion force of the electric double layers between the SLB and the solid. [102] When pure water was used, a single SLB is formed, whereas stacked SLBs called "lobes" are formed when ionic strength of the water solution is high (1 mM to 1 M) because the repulsion force of the electric double layers is weakened due to ionic shielding.

Since SLBs have fluidity on the solid support, SLBs can be considered as constituting a two dimensional fluid in water. According to [101, 116], the two-dimensional flow of the SLB can be modeled as the following Stokes equation.

$$\zeta \boldsymbol{v} = \nabla \sigma - \mu \nabla^2 \boldsymbol{v}, \tag{6.1}$$

where $\boldsymbol{v}$ is the membrane velocity, σ is membrane tension, $\zeta(\approx 10^7 \, \mathrm{Pa \cdot s/m})$ is the friction coefficient, and μ is the membrane viscosity. Since the length of the SLB is above 30 nm, the viscous force can be negligible [116] and the above equation becomes

$$\zeta \boldsymbol{v} = \nabla \sigma \tag{6.2}$$

Since the membrane flow is an incompressible flow, $\boldsymbol{v}$ satisfies $\nabla \cdot \boldsymbol{v} = 0$. It follows that the membrane pressure σ satisfies Poisson's equation:

$$\nabla^2 \sigma = 0. \tag{6.3}$$
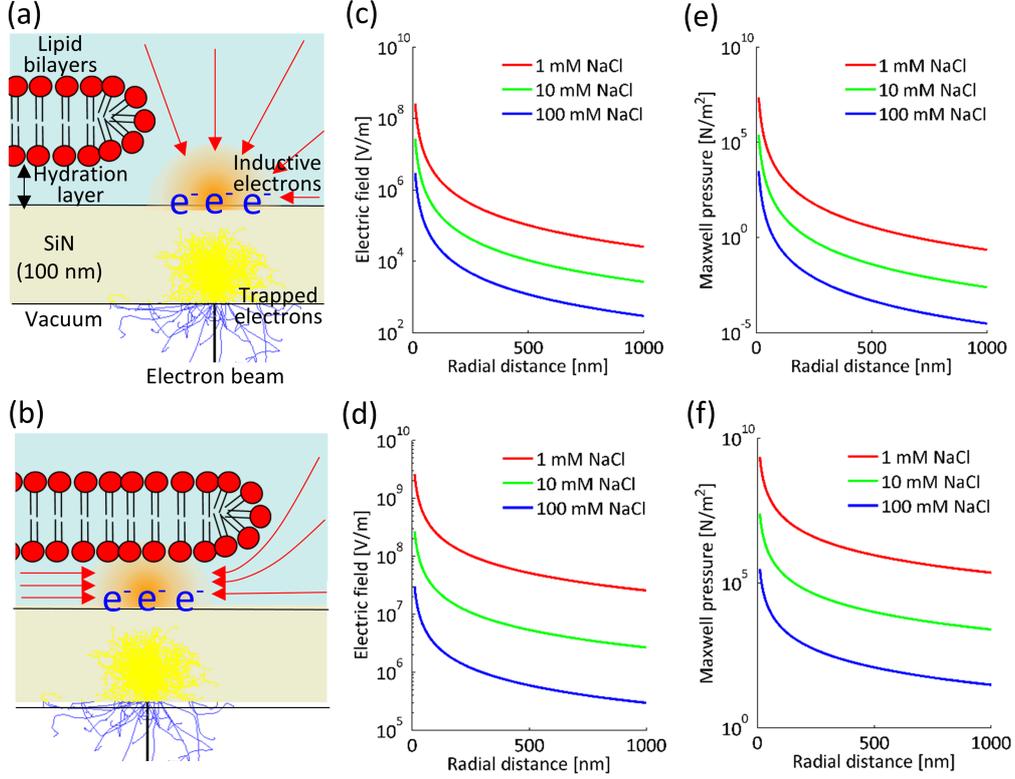
Fig. 6.2. Mechanical manipulation mechanism of EB-induced virtual cathode for lipid bilayers. (a,b) Schematic view of the mechanical manipulation mechanism of EB-induced virtual cathode. Red arrows indicate the direction of the electric field. (c-f) Spatial distribution of the electic field (c,d) and Maxwell stress (e,f) caused by electric currents flowing from a virtual cathode to the solution. (a,c,e) Virtual cathode exists outside the virtual cathode. (b,d,f) Virtual cathode exists inside the virtual cathode.

The boundary condition of the pressure at the interface between the two fluids is calculated from the balance of two-dimensional Laplace's pressure as follows:

$$\sigma = \lambda \kappa \tag{6.4}$$

where λ is the line tension at the interface and κ is the curvature at the interface. The normal velocity of the interface between the two fluids V is calculated from the pressure p:

$$V = \frac{1}{\zeta} \nabla p \cdot \boldsymbol{n}, \tag{6.5}$$

where $\boldsymbol{n}$ is the unit normal vector of the interface.

When the electric field $\boldsymbol{E}$ exists at the interface of the fluids, Maxwell stress P_M is applied to the interface

$$P_M = \frac{1}{2}|\epsilon_1 - \epsilon_2||\boldsymbol{E}|^2,$$

where ϵ_1 and ϵ_2 are dielectric constants of the fluid 1 and 2, respectively. Therefore, deformation of the boundary can be achieved by applying an external electric field if the two fluids have different dielectric constants. In case of lipid membrane flows, the relative permittivities of the lipid bilayers and water were about 2 and 80, respectively, thereby resulting in the pressure on the lipid bilayers. Therefore, the above boundary condition is modified as follows:

$$\sigma = \lambda \kappa + P_M h, \tag{6.6}$$

where h is the thickness of the SLB. The electric field of the virtual cathode depends on its location. When the virtual cathode exists outside the SLB (Fig. 6.2 (a)), the current density at position r from the virtual cathode is $j = I/(2\pi r^2)$ caluculated in Section 3.2, and thus the corresponding electric field is

$$E(\boldsymbol{r}, \boldsymbol{r}_i) = \frac{\rho I}{2\pi |\boldsymbol{r} - \boldsymbol{r}_i|^2}, \tag{6.7}$$

where ρ is the electric resistivity, I is the Ohmic current, and $\boldsymbol{r}_i$ indicates the position of the i-th virtual cathode. When the virtual cathode exists inside the virtual cathode, the current flows through the hydration layer between the SLB and the solid (Fig. 6.2 (b)). Thus, the current density at position r from the virtual cathode becomes $j = I/(2\pi r d)$, where d denotes the height of the hydration layer. The electric field is described as follows.

$$E(\boldsymbol{r}, \boldsymbol{r}_i) = \frac{\rho I}{2\pi d |\boldsymbol{r} - \boldsymbol{r}_i|}. \tag{6.8}$$

Figs. 6.2 (c-f) show the spatial profiles of the electric field and the Maxwell pressure. In Fig. 6.2, it is assumed that the thickness of the lipid bilayer was about 4 nm, the Ohmic current was 2 nA, and the thickness of the hydration layer was 1 nm. The electric field of the virtual cathode inside the lipid bilayer is much higher than that of the virtual cathode outside the lipid bilayer. In both cases, the Maxwell stress is above 10^{-7} J/m^2 within 100 nm from the virtual cathode. According to Bar-Zib et al. [24], a surface tension of $10^{-6} - 10^{-7}$ J/m^2 is suitable for shape transformation of the lipid bilayer. Therefore, it is expected that the electric field due to the Ohmic drop is strong enough to deform lipid bilayers and that the surface tension energy is localized at the submicrometer level.

6.3   Materials and methods

6.3.1   Chemicals

1,2-dioleoyl-sn-glycero-3-phosphocholine (DOPC), 1,2-dipalmitoyl-sn-glycero-3-phosphocholine (DPPC), and Texas Red 1,2-dihexadecanoyl-sn-glycero-3-phosphoethanolamine, triethylammonium salt (TR-DHPE) were purchased from Avanti Polar Lipid. Cholera Toxin Subunit B (Recombinant), Alexa Fluor 488 Conjugate (CTB488) was purchased from ThermoFisher. Monosialoganglioside GM1 from bovine brain was purchased from Sigma-Aldrich. POLARIC-500c6F was purchased from GORYO Chemical Inc. Cholesterol,
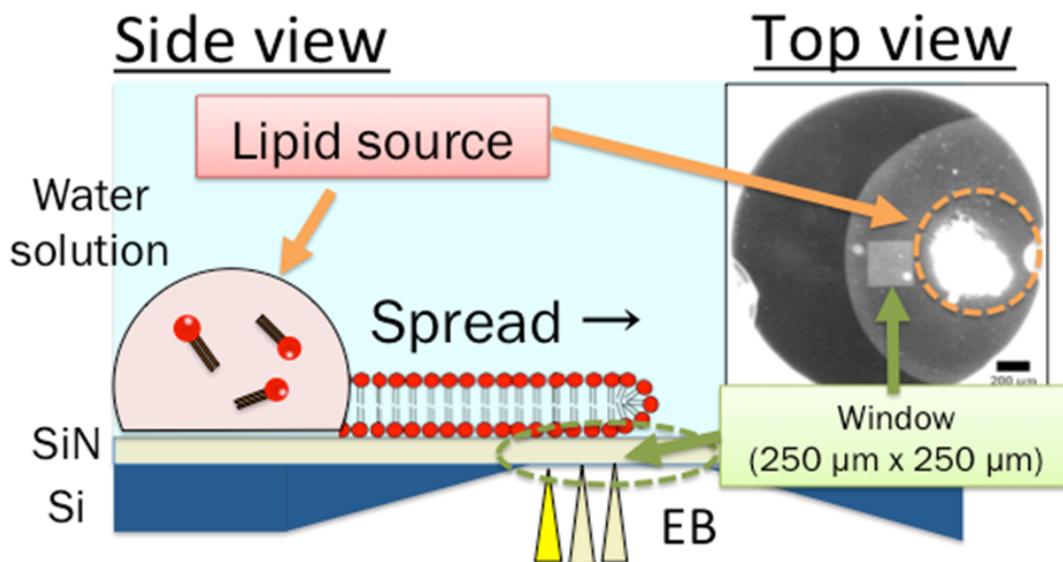
Fig. 6.3. Formation of SLBs on a hydrophilized SiN membrane by self-spreading techniques.
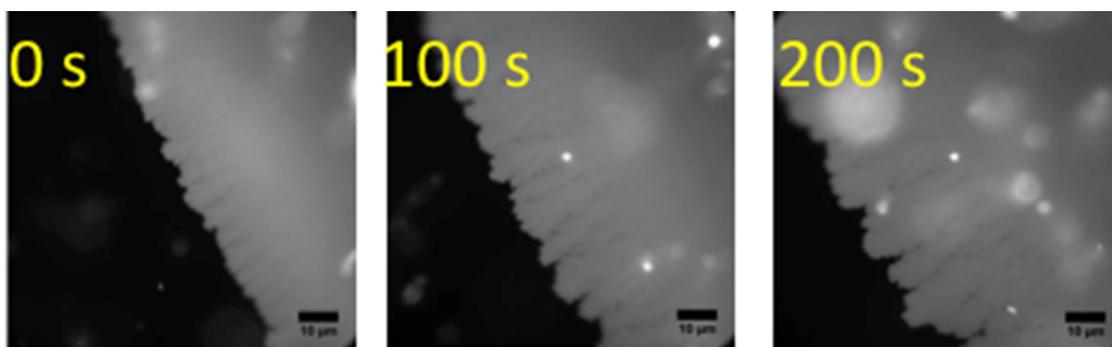
Fig. 6.4. Time lapse images of self-spreading of DOPC lipid bilayers.

ethanol, chloroform, and NaCl were purchased from Wako. Milli-Q water was used for all experiments in this chapter.

6.3.2   Sample preparation

The preparation of the lipid bilayers was carried out as shown in Fig. 6.3. The surface of the SiN membrane was hydrophilized by a 30 s treatment with a corona discharger (CFG-500; Shinko Electric & Instrumentation Co., Ltd.). Dried film of lipid mixtures were placed on the hydrophilized SiN membrane, and 1 mL of pure water or NaCl water solution was dropped on the membrane slowly. To spread the lipid bilayers, samples were placed at room temperature (24°C) in case of DOPC and Texas Red DHPE mixtures or DOPC and POLARIC mixtures, and samples were heated up to 70°C for 30 min using
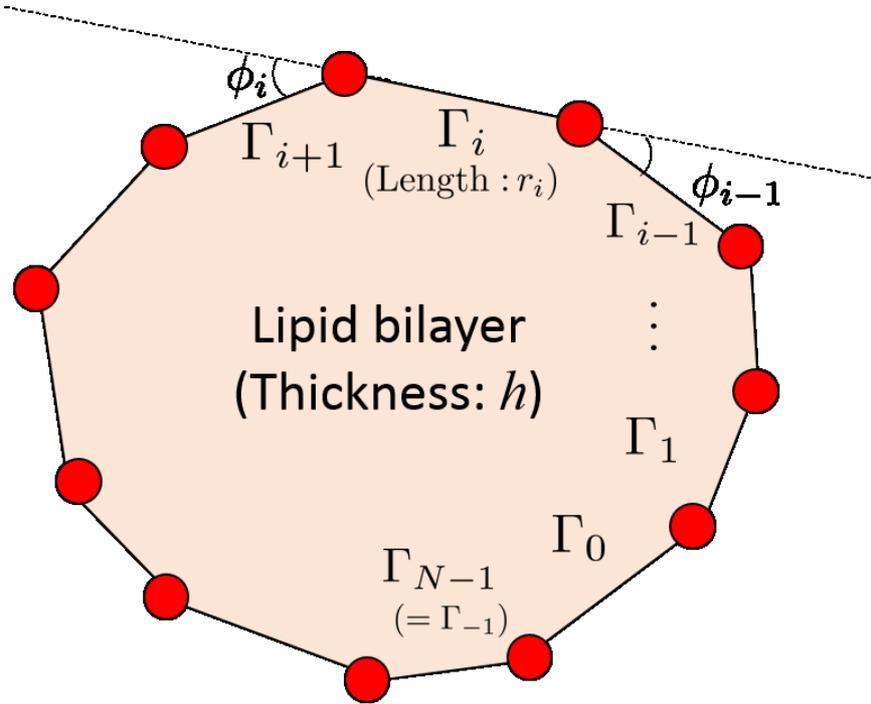
Fig. 6.5. Approximation of the SLB by a closed polygon curve

a hot plate in case of DOPC, DPPC, cholesterol, and Texas Red DHPE mixtures and DOPC, DPPC, cholesterol and ganglioside GM1 mixtures. Self-spreading of SLBs was observed as shown in Fig. 6.4. TR-DHPE was observed with Texas Red Filter (Ex: 532-587, DM: 595, BF: 608-683; Nikon).

6.3.3   Image processing

ImageJ (NIH) was used for image processing. To obtain the edges of the lipid bilayers in Fig. 6.13, the image was first filtered by a 5×5 mean filter and then binarized using Otsu' s method. Finally, the edge of the lipid bilayer was tracked using the Wand tool in Image J.

6.3.4   Numerical simulation of the surface deformation of the SLB

To verify whether the Maxwell stress is strong enough to deform the SLBs, we conducted simulations of the deformation of the SLBs. The equations (6.2), (6.3) and (6.6) are equivalent to Hele-Shaw flow [117], which is a penetration flow into a porous media. Hele-Shaw problems can be solved by tracking the interface. In this thesis, the Hele-Shaw problems were solved using the charge element method proposed by Sakakibara et $al.$, [118].

In this simulation, the interface was approximated by a closed polygon line as shown in Fig. 6.5. The number of the vertices is N, and the position of the i-th vertex $(i = 0, 1, \cdots, N - 1)$ is $(\boldsymbol{x}_i = (x_i, y_i)^T)$. The edge between two vertices $\boldsymbol{x}_i$ and $\boldsymbol{x}_{i+1}$ is

represented by

$$\Gamma_i = \{(1 - \lambda)\boldsymbol{x}_i + \lambda\boldsymbol{x}_{i+1} | \lambda \in [0, 1]\} \quad (i = 0, 1, \cdots, N - 1). \tag{6.9}$$

The curvature of the i-th edge Γ_i k_i is approximated by $k_i = \frac{\tan(\phi_i/2)+\tan(\phi_{i-1}/2)}{r_i}$, where ϕ_i is the angle between the edge Γ_i and Γ_{i+1}, and $r_i = |\boldsymbol{x}_{i+1} - \boldsymbol{r}_i|$. The boundary condition 6.6 is approximated by

$$\sigma = k_i + \lambda h \sum_{l=1}^{N_c} E(\boldsymbol{R}_i, \boldsymbol{r}_c{}^{(l)}) \tag{6.10}$$

,where $\boldsymbol{R}_i = (\boldsymbol{x}_{i+1} + \boldsymbol{x}_i)/2$ and $\boldsymbol{r}_c{}^{(l)}$ is the position of l-th virtual cathode $(l = 1, 2, \cdots, N_c)$. Poisson's equation $\nabla^2\sigma = 0$ under the boundary condition (6.10) is solved by the modified charge element method; the differential equation (6.2) is solved by the Runge-Kutta method (Details are described in [118]). The electric field is defined by (6.8) when the virtual cathode exists inside the polygon, and defined by (6.7) when the virtual cathode exists outside the polygon.

In our simulation, the SLB was approximated by 50 μm-radius-circle and its thickness was set at 8 nm (double bilayer). We examined three patterns of virtual cathodes: (i) A single virtual cathode was located inside the SLB. (ii) A single virtual cathode was located 100 nm outside the SLB. (iii) Two virtual cathodes were located inside the SLB. The position was defined as

$$\boldsymbol{r}_c{}^{(1)} = R(\cos\theta, \sin\theta)^T, \quad \boldsymbol{r}_c{}^{(2)} = R(\cos(-\theta), \sin(-\theta))^T, \tag{6.11}$$

where $R = 46\,\mu$m and $\theta \in [3°, 20°]$. The number of the vertices N is 200. The stepsize of the Runge-Kutta method Δt is 1.25×10^{-5} s for (i) and (ii) and 1.25×10^{-6} s for (iii).

6.4 Results and discussion

6.4.1 Dynamic patterning of SLBs

Fig. 6.6 shows the spatiotemporal changes of the DOPC lipid bilayers with 1mol% TR-DHPE in 10 mM NaCl water solution. Acceleration voltage of an EB was 2.5 kV, and the EB was scanned in a rectangular shape. When an EB was irradiated, a decrease in fluorescence intensity was observed. Especially, the intensity decreased more as the dose amount increased, as shown in Fig. 6.7 (a). Behaviors of the fluorescence intensity after the irradiation depended on dose amount of electrons. When the dose amount was 2000 pC, the fluorescence intensity recovered from the outside of the irradiated area (Fig. 6.6 (a)). The edge of the recovered area was clearly observed, and the fluorescence intensity at the edge of the recovered area became higher than that at the unirradiated area ($t = 8$ s), and finally the fluorescence intensity recovered to the same value before the irradiation ($t = 12$ s). Recovery speed depended on the dose amount, and the speed became higher as the

dose amount increased (Fig. 6.7 (b)). On the contrary, such recovery of the fluorescence intensity after the EB irradiation was not observed when the dose amount was 500 pC (Fig. 6.6 (b)). When the dose amount was 60 pC, the recovery of the fluorescence intensity after the irradiation was observed. But the sharp edge of the recovered area was not observed contrary to the result in which the dose amount was 2000 pC (Fig. 6.6 (c)).

To investigate the fluidity of the photobleached area, a grid pattern of the virtual cathode was generated onto the DOPC lipid bilayers with 1mol% TR-DHPE in 100 mM NaCl water solution, as shown in Fig. 6.8. When the total amount of the dose amount was 1000 pC for the grid pattern of the virtual cathode, the fluorescence intensity inside the grid pattern decreased, as compared to the intensity outside the grid pattern. Then, the EB spot was irradiated on the grid pattern as shown in Fig. 6.9, and the recovery of the fluorescence intensity was observed inside the grid (B) as well as the EB-irradiated area. On the other hand, the fluorescence intensities outside the grid pattern (A) and inside the grid (C) decreased due to the fluorescence observation.

Finally, we demonstrated dynamic patterning of DOPC bilayers with 1mol% TR-DHPE in 100 mM NaCl water solution, as shown in Fig. 6.10. Before the patterning, a completely photobleached area was generated and it was confirmed that the recovery of the fluorescence intensity did not recover after the EB irradiation ($t = 0$). Then, a spiral virtual cathode was generated within the photobleached area such that one end of the spiral was in contact with the outside of the photobleached area. After the generation of the spiral virtual cathode, recovery of the fluorescence intensity started from the outside, and the fluorescence intensity recovered along the spiral as shown in Fig. 6.10.

In these experiments, fluorescent molecules (Texas Red) were attached to lipid molecules and thus the recovery of the fluorescence indicated the existence of lipid molecules with unphotobleached fluorescence molecules. In other words, the recovery of the fluorescence intensity indicated lateral migration of lipid molecules with unphotobleached fluorescence molecules, and this was possible when the SLBs had fluidity. Considering that the decrease of the fluorescence intensity depended on the dose amount and that the recovery of the fluorescence intensity was not observed when the dose amount was between 60 pC and 180 pC (Fig. 6.6(a)), it is considered that the SLBs did not lose their fluidity after the EB irradiation, and that the EB affected only the photobleaching of the fluorescent molecules.

Meanwhile, the recovery of the fluorescence intensity was not observed when the dose amount was 500 pC (Figs. 6.6 (b)), and more injection of electrons resulted in the recovery of the fluorescence intensity (Fig. 6.6 (c)). According to the results of grid pattern (Figs. 6.8 and 6.9) and spiral pattern (Fig. 6.10), it can be understood that the photobleached area which did not recover after the EB irradiation did not have fluidity, and re-spreading of the SLBs could be achieved by irradiating an EB to the photobleached area for the following reasons. The speed of the photobleaching inside the grid was faster than that outside the grid (Fig. 6.8) because the photobleached molecules outside the grid could freely diffuse and the exchange of the photobleached molecules with the unphotobleached

molecules occurred outside the microscopic field. However, the photobleached molecules inside the grid could not diffuse across the grid. The recovery of the fluorescence intensity inside the grid after the EB spot irradiation (Fig. 6.9) would be because the fluidity of the SLBs recovered only on the spot irradiated area, and the photobleached molecules inside the grid and unphotobleached molecules outside the molecules could diffuse freely across the EB spot irradiated area. Re-spreading of the SLBs could also be supported by the result that the spiral virtual cathode induced the recovery of the fluorescence intensity, and it started from the edge which was in contact with the unphotobleached area.

The recovery speed of the fluorescence intensity increased as the dose amount was 1000 pC to 2000pC, but the recovery speed was almost saturated when the dose amount was above 2000 pC. The spreading speed of the SLB depended on the friction constant between the SLB and the solid support and the pressure gradient caused by the lipid source. [101, 116] Basically, the existence of the virtual cathode would not affect the amount of the lipid source. Therefore, our results indicate that the irradiation of EB could affect the friction constant. Especially, the friction constant would become large enough to stop the spreading of the SLB when the dose amount was between 200 pC and 1000 pC. This might be because the photobleached and broken molecules existed in the EB irradiated area, or the hydrophilicity of the EB-irradiated area was not high enough to spread the SLB. The saturation of the recovery speed would be due to the physical lower limit on the friction constant.

Therefore, our virtual cathode technique could achieve dynamic control of the fluidity of the SLBs by changing dose amount of electrons. These results were observed due to the surface reactions induced by the electrical and chemical effects of electrons, and the former effects were significant considering the detachment of MPC polymers (Chapter 5). Re-spreading phenomena were not observed in the case of MPC polymers, possibly because MPC polymers were physically entangled and they did not have fluidity.

The edges of the EB-irradiated area were still photobleached after the EB irradiation. This might be because some broken lipid molecules were attached to the substrate by chemical reactions. However, re-spreading of the SLB was observed even when such dark edges existed, and thus the existence of the dark edges would be problematic to dynamically control the spreading of SLBs.
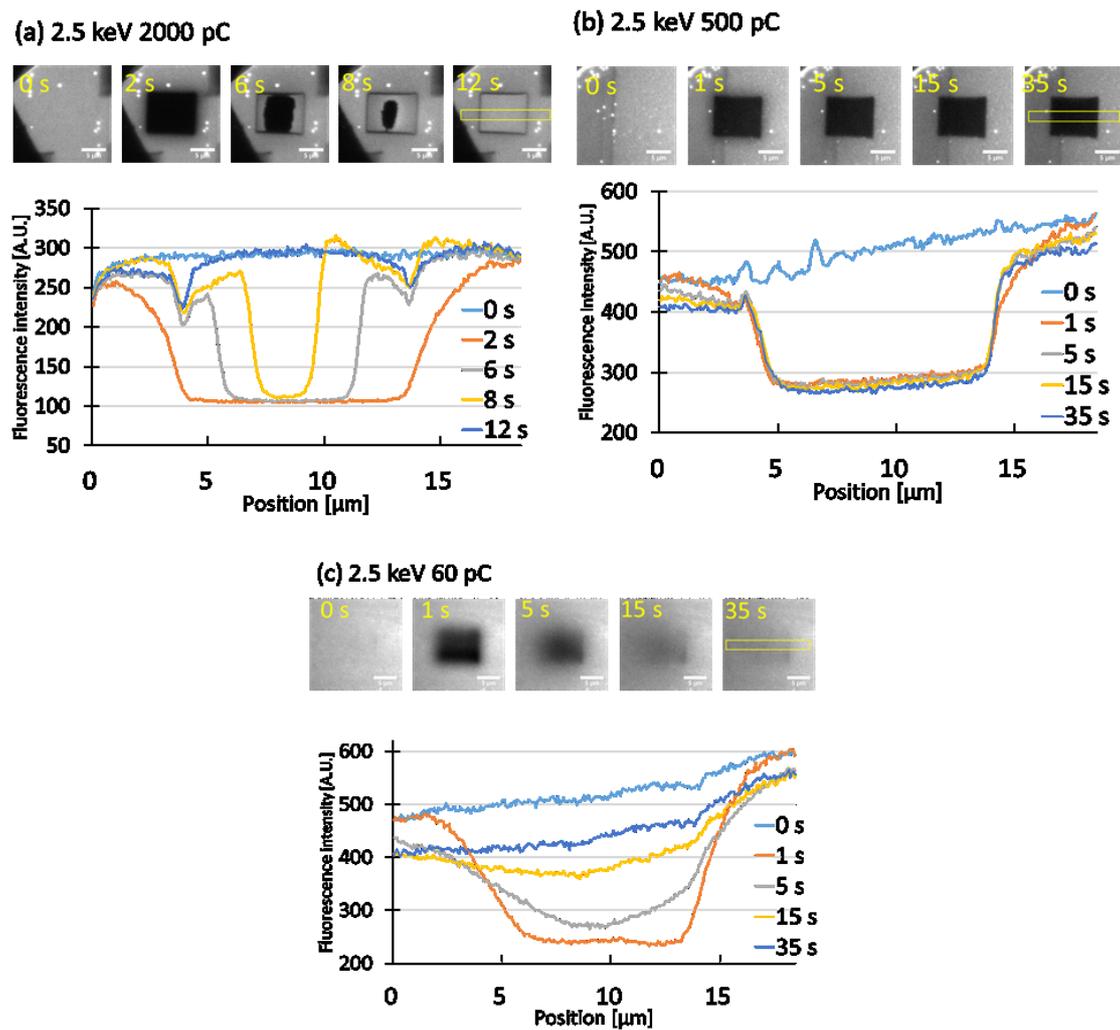
Fig. 6.6. Fluorescence images of DOPC lipid bilayers before and after EB irradiations. Yellow boxes represent ROIs for average intensity profiles.
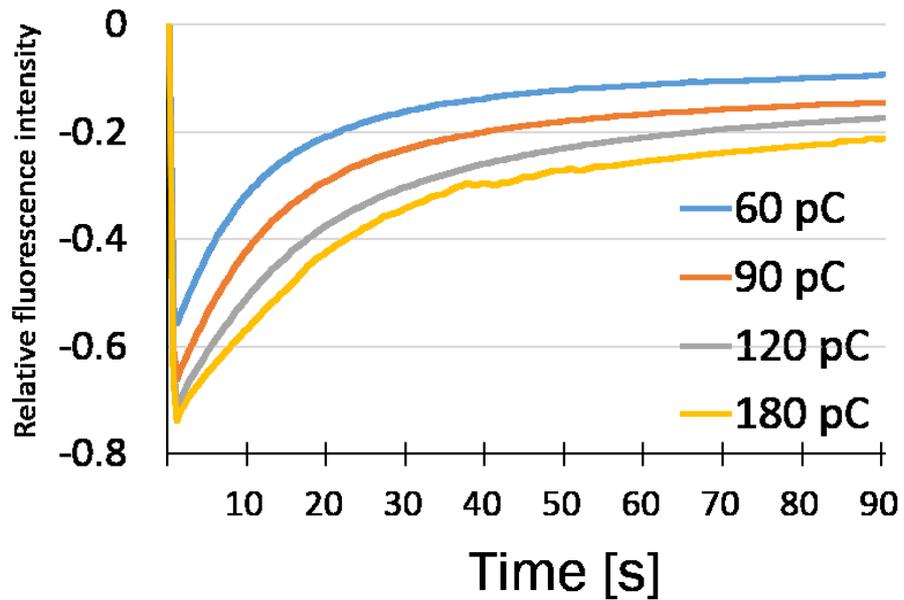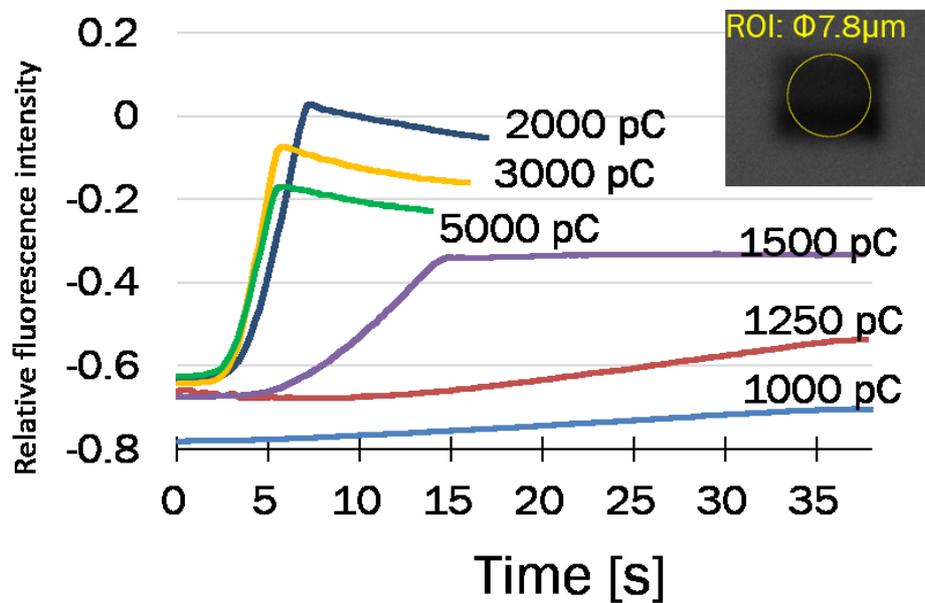
Fig. 6.7. Temporal changes of relative fluorescence intensity of DOPC lipid bilayers after the EB irradiations. Fluorescence intensity was averaged within 3.9 μm from the center of the rectangle virtual cathode.
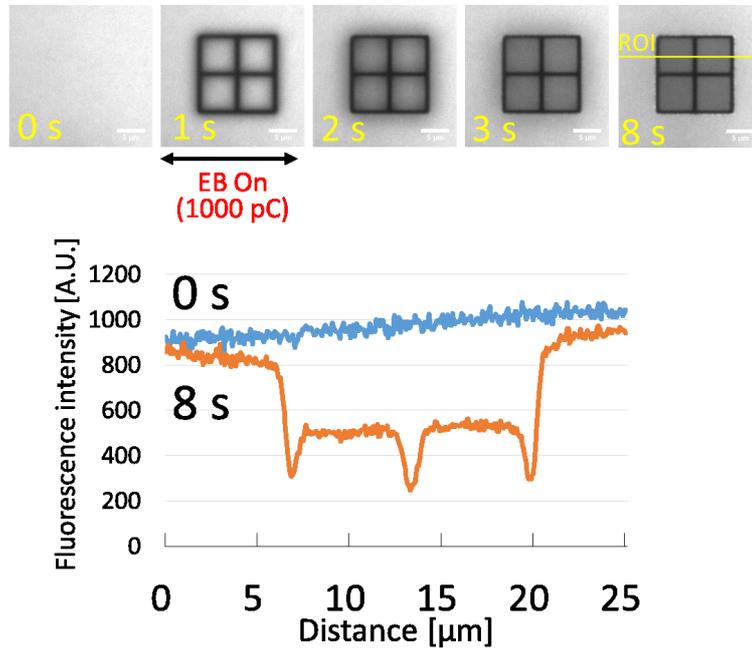
Fig. 6.8. Temporal changes of fluorescence intensity of the grid-patterned supported lipid bilayer.
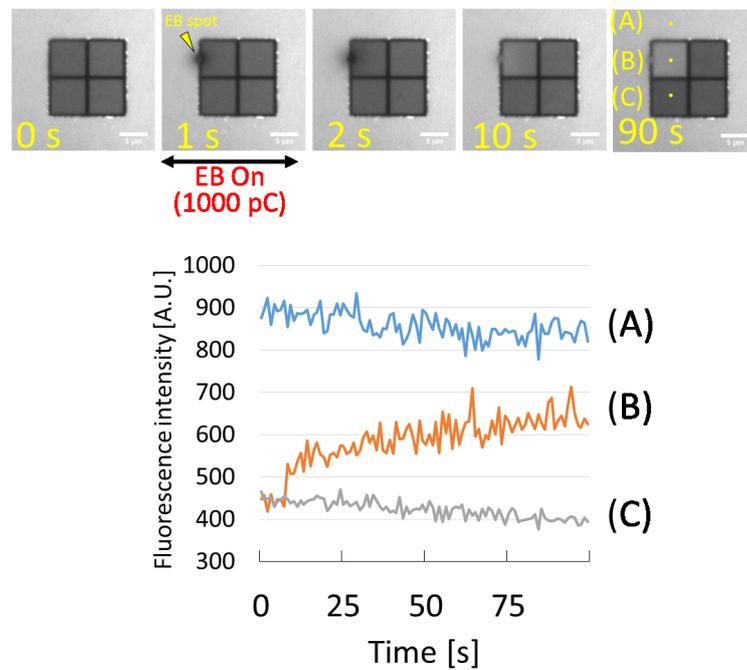
Fig. 6.9. Fluorescence recovery after the EB spot irradiation on the grid pattern.
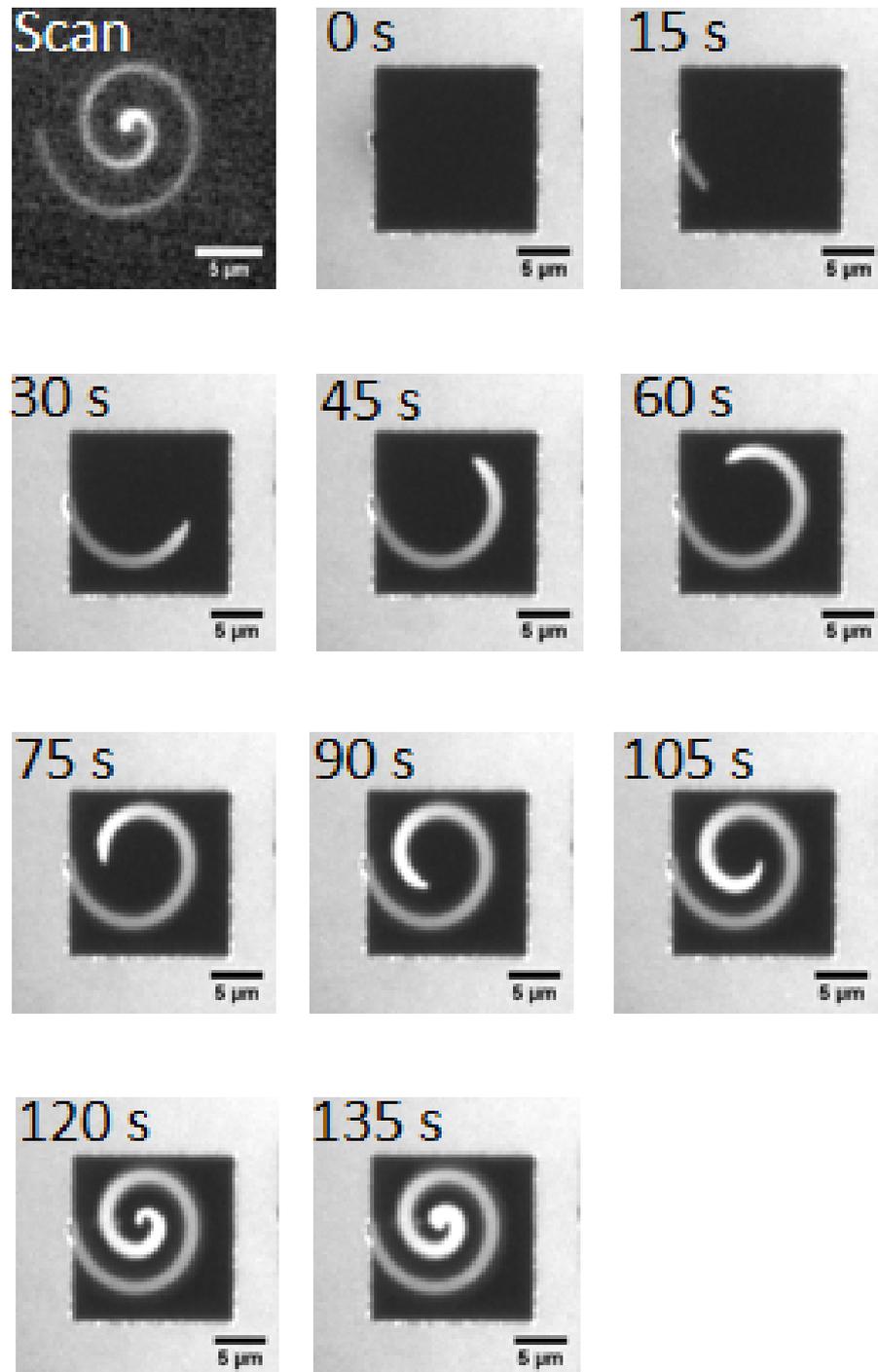
Fig. 6.10. Dynamic patterning of supported lipid bilayers by the spiral virtual cathode.

6.4.2   Membrane domain formation by dynamic spreading of SLBs

Fig. 6.11 (a) shows the spatiotemporal changes of fluorescence intensity of DOPC / DPPC / cholesterol (2:2:1) with 1mol% TR-DHPE in a 100 mM NaCl solution at room temperature. The acceleration voltage and the dose amount of the EB was 2.5 kV and 5000 pC, respectively. After the EB irradiation, re-spreading of the SLBs was observed as is the case in DOPC ($t = 5$, 10, 15 s). However, the dark and spot region grew after the re-spreading of the SLBs, as opposed to DOPC ($t = 40$, 90 s). A similar dark region was observed in the case of DOPC / DPPC / cholesterol (2:2:1) with 1mol% TR-DHPE and 1mol% ganglioside GM1 in 100 mM NaCl solution (Fig. 6.11 (b, c)).

   To investigate the dark region, CTB488 in PBS was added after the EB experiments. The final concentration of CTB488 was about 1 μg/mL, and the samples were placed at room temperature for 30 min. Then, the samples were washed out five times with 100 mM NaCl solutions. CTB488 was observed with an inverted fluorescence microscope(Ti-S, Nikon) mounted with a 20x lens (CFI S Plan Fluor ELWD; Nikon), a GFP filter (Ex: 450-490, DM: 495, BW: 500-550; Nikon), a CCD camera(1501C-USB-TE, Thorlabs), and an LED white-light source(pE-300; CoolLED). When the ganglioside GM1 was not added, the fluorescence intensity was remained unchanged (Fig. 6.11 (b)), whereas the fluorescence intensity became higher in the dark area as compared to unirradiated area (Fig. 6.11 (c)). Considering that CTB488 specifically binds to the ganglioside GM1, the ganglioside GM1 had a richer presence in the dark area.

   According to previous studies, ternary lipid mixtures of DOPC, DPPC, and cholesterol were phase separated when the molar ratio was 2:2:1, and liquid-ordered(Lo) and liquid-disordered phases(Ld) emerged. [119] Moreover, it is known that TR-DHPE and CTB488 are rich in Ld and Lo phase respectively. [120, 121] Therefore, our virtual cathode techniques successfully achieved the directed self-assembly of Ld phase by the re-spreading of SLBs. Though the directed assembly of lipid rafts by static patterns has already been achieved in [122], we have achieved a dynamic self-assembly of lipid rafts for the first time. Our technique would be applied to a dynamic mearument and control of the self-assembly process of lipid rafts.

(a)

(b) Without G_{M1}

(c) With 1mol% G_{M1}
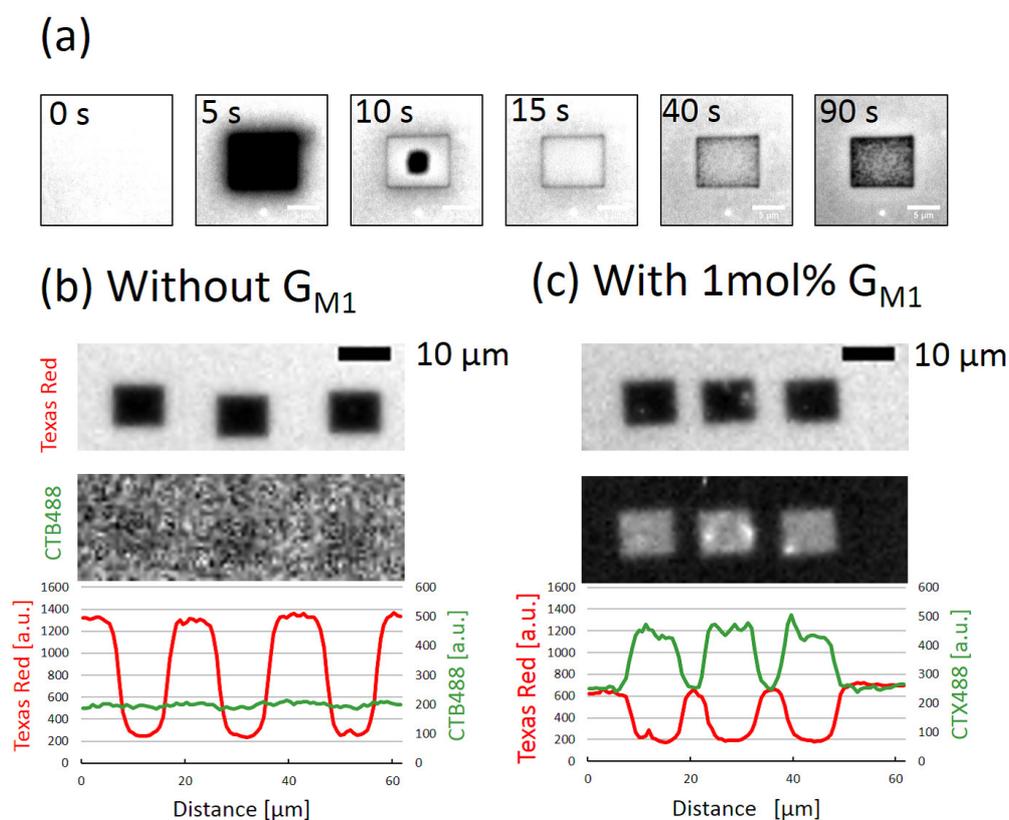
Fig. 6.11. Fluorescence images of DOPC/DPPC/Cholesterol lipid bilayers during and after the EB irradiations. (a) Time lapse images of the fluorescence intensity observed with Texas Red filter. (b, c) Fluorescence images and average intensity profiles after the addition of CTB488 solutions. (b) GM1 was not added to the SLB. (c) 1mol% GM1 was added to the SLB. Light spots in fluorescence images are small vesicles which would be attached after the experiments.

6.4.3   Deformation of lobe structures of SLBs

Fig. 6.12 shows the deformation of multilayered lipid bilayers consisting of DOPC dyed with POLARIC-500c6F in a 10 mM NaCl water solution. An EB spot was irradiated for 1 s, and its acceleration voltage and beam current were set at 2.5 kV and 1.6 nA, respectively. When a virtual cathode was generated inside the edge of the lipid bilayers, large deformation of the lipid bilayers was observed and recovered when the irradiation stopped [Fig. 6.12 (a, b)]. In contrast, deformation of the lipid bilayers was minor when a virtual cathode was generated outside the edge of the lipid bilayers [Fig. 6.12 (c, d)]. Temporal changes in the distance between the edge of the lipid bilayers and the virtual cathode are shown in Fig. 6.13. The lipid bilayer was deformed at the micrometer scale when the virtual cathode was generated 4—6 μm inside the edge of the lipid bilayers [Fig. 6.13 (a—c)], whereas the lipid bilayers were repelled from the virtual cathode by around several hundred nanometers when the virtual cathode was generated 0.4—0.5 μm outside the edge of the lipid bilayers [Fig. 6.13 (d—f)]. These results indicated that the electric field of the EB-induced virtual cathode was strong enough to exert mechanical stress on the lipid bilayers, and that the mechanical stress was large only around the virtual cathode.
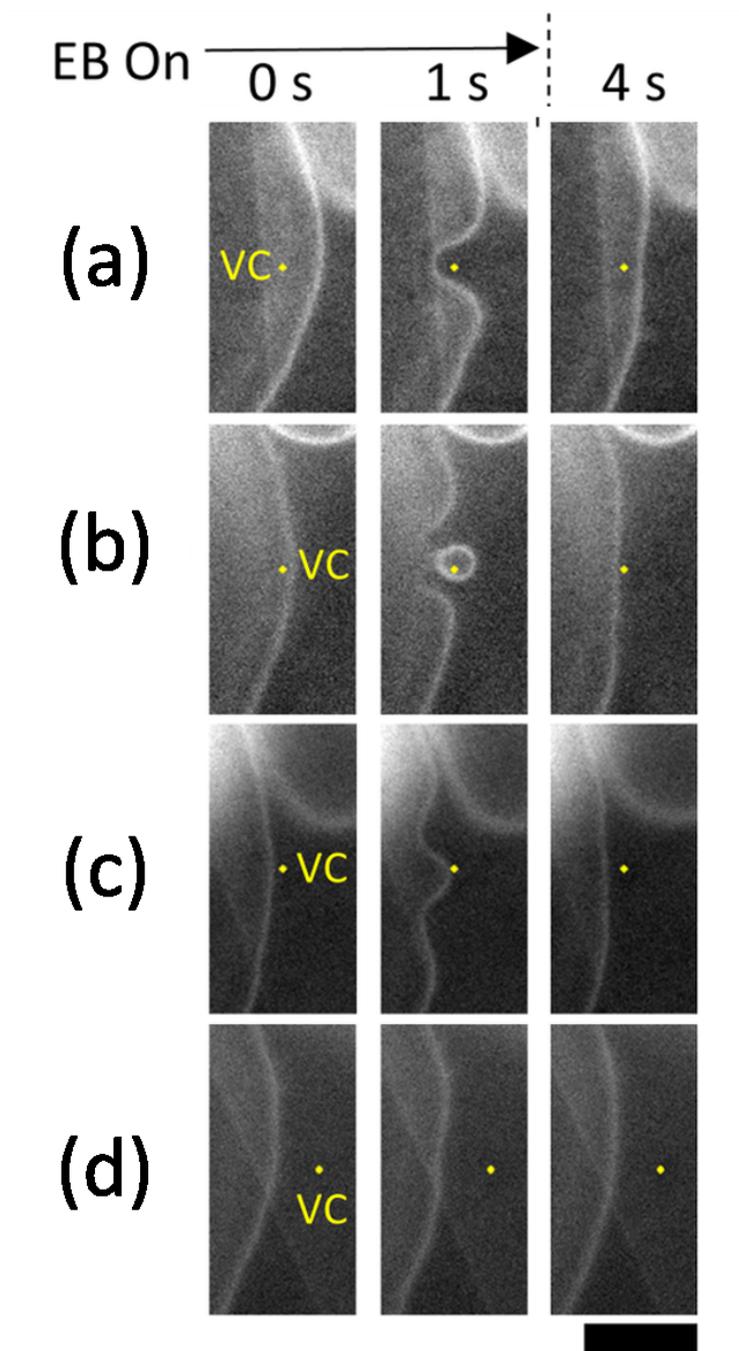
Fig. 6.12. Time-lapse images of the DOPC lipid bilayers dyed with POLARIC around the EB-induced virtual cathode. The virtual cathode was generated inside the lipid bilayers (a, b) or outside the lipid bilayers (c, d) for 1 s. Yellow circles indicate the positions of the virtual cathode. Scale bars indicate 10 μm.
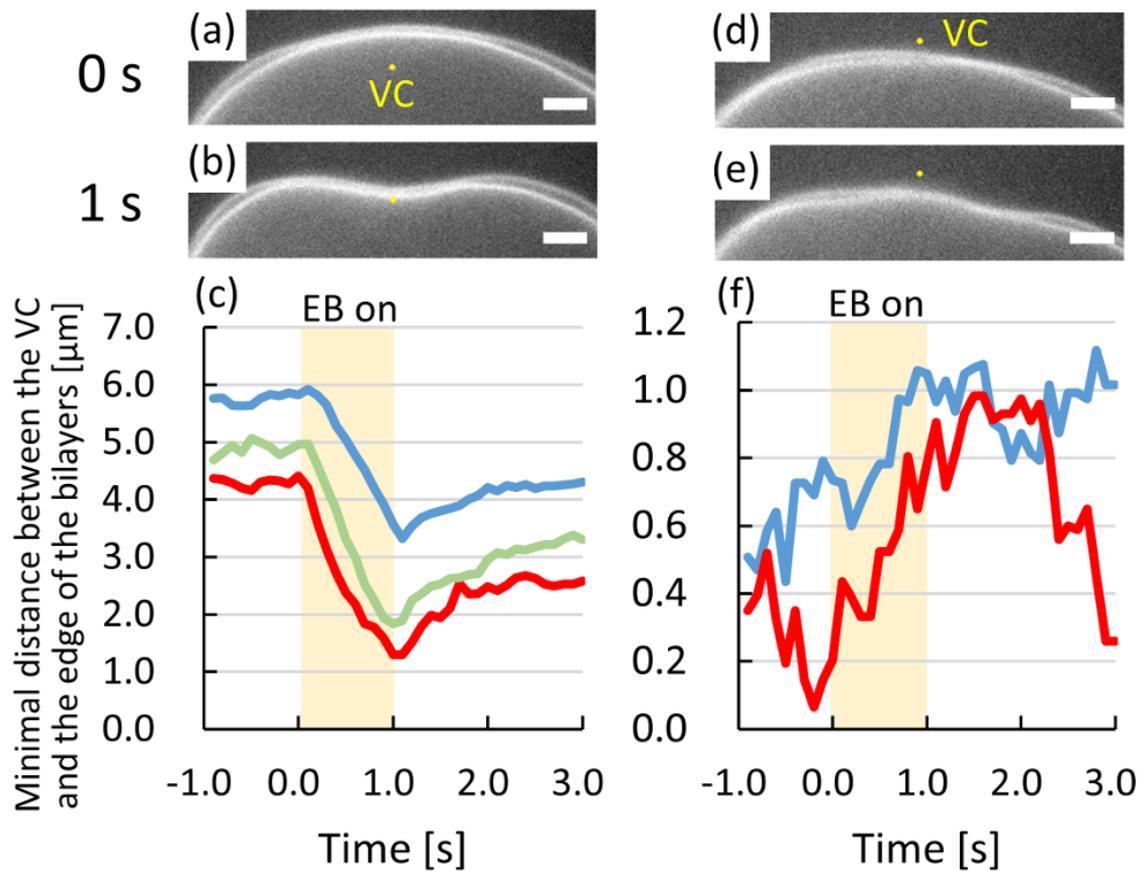
Fig. 6.13. Time-lapse images of the DOPC lipid bilayers around the EB-induced virtual cathode (a,b,d,e) and temporal changes in the minimal distance between the virtual cathode and the edge of the lipid bilayers (c, f). (a—c) The virtual cathode was generated 4—6 μm inside the edge of the lipid bilayers. (d—f) The virtual cathode was generated 0.4—0.5 μm outside the edge of the lipid bilayers. Scale bars indicate 5 μm.

6.4.4   Numerical simulations of the deformation of the SLB

Fig. 6.14 shows the simulations results of the deformation of lipid bilayers when the virtual cathode exists inside the SLB. As shown in Fig. 6.14(b), the electric field was deformed to avoid the   virtual cathode. It can be seen in Fig. 6.14(c) that the deformation quantity depended on the location of the virtual cathode, and the relaxation time became long for large deformation. Fig. 6.15 shows the equilibrium state of the deformation and its curvature. The curvature became negative around the virtual cathode to avoid it, whereas the increase of the curvature was observed around the edges whose curvatures were negative. Contrary to the above results, the deformation was rarely observed when the virtual cathode existed 100 nm outside the SLB as shown in Fig. 6.16. These results indicate that the Maxwell stress could be applied to the SLB only when the virtual cathode was placed inside the edge of the SLB, and that the stress was localized.

When virtual cathodes are located as shown in Fig. 6.17(a), the increase of the curvature was observed between the two cathodes (Fig. 6.17(b,c)). This increase of the curvature became larger as the two cathodes came closer (i.e. θ decreased) (Fig. 6.17(c)). Fig. 6.17(d) shows the relationship between the curvature of the edge Γ_0 and θ (Γ_0 was defined as shown in Fig. 6.17(c)). When $3° \leq \theta \leq 10°$, the curvature became larger as θ decreased, whereas the curvature did not increase when $\theta \geq 10°$. According to these results, the control of curvature could be achieved by generating several virtual cathodes near the edge.

These numerical simulations support the premise that the Maxwell stress induced by the virtual cathode could be one of the driving forces of the deformation of the SLB, but other effects such as Marangoni effects or electrostatic effects should be considered for the deformation. The temperature rise could have occurred when the virtual cathode was generated, as discussed in Chapter 2, and the temperature rise could have changed the elastic properties of the SLB, such as line tension. However, the flow speed induced by the Marangoni effects was estimated at   10 nm/s according to our evaluation of the temperature rise for the EB irradiation (Details are shown in Appendix D). Electrostatic effects should also be considered since the zeta potential of the DOPC in 1 mM NaCl water solution is about -21.8 mV and the corresponding surface charge density σ_0 is about 1.6×10^{-3} C/m^2. [102] Electrostatic pressure can be calculated by $\sigma_0 E(r)$, but this pressure is small compared to the Maxwell pressure, as shown in Fig. 6.18. Therefore, the Marangoni effects or electrostatic effects would be small compared to the Maxwell stress.

According to our experimental results and numerical simulations, the proposed model based on Maxwell stress could not explain the formation of the positive curvature around the virtual cathode as shown in Figs. 6.12 (b) and (c). To form such positive curvature around the virtual cathode, it is necessary to consider the attraction force toward the cathode. One possible candidate for such an attraction force is the viscous force of electroosmotic flow. As discussed in Chapter 4, the SiN is negatively charged

and thus the flow toward the virtual cathode could be generated. In our experiments, the Debye length of the electric double layer was about 3 nm (in 10 mM NaCl solution), and the hydration layer between the SLB and the SiN was about 1 nm. Thus, the SLB would be affected by the electroosmotic flow, but the detailed mechanism should be studied in future works.

The mechanism of the proposed method is similar to optical tweezers [24] at the point of the Maxwell stress, but the spatial resolution of the proposed method would be finer than that of the optical tweezers because the large deformation occurred only when the virtual cathode existed inside the lipid membrane. Therefore, it is expected that the proposed method would achieve a nanometer-scale mechanical stress on biomolecules to measure the mechanical and structural properties of the biomolecules, which cannot be achieved by optical manipulations.

6.5   Conclusion of this chapter

In Chapter 6, we have applied the proposed techniques to the electromechanical control of lipid membrane domains and morphology. By controlling the surface reactions of EB-induced virtual cathode, SLBs were dynamically patterned, and fluidity and re-spreading of the SLBs could be controlled by the dose amount of the EB. Moreover, re-spreading of SLBs induced a directed self-assembly of a liquid-ordered phase which contained rich ganglioside GM1 in a DOPC/DPPC/cholesterol mixture. Finally, a dynamic and reversible deformation of the stacked lipid bilayers was achieved by several forces such as Maxwell's stress around the EB-induced virtual cathode.

Fig. 6.14. Simulation results of the deformation of the SLB when the virtual cathode was located inside the SLB. (a) Initial condition of the SLB and the location of the virtual cathode. (b) Temporal change of the interface of the SLB when the virtual cathode was located 5 μm inside the SLB. (c) Temporal change of the distance between the edge of the SLB and the virtual cathode.

(a)

(b)
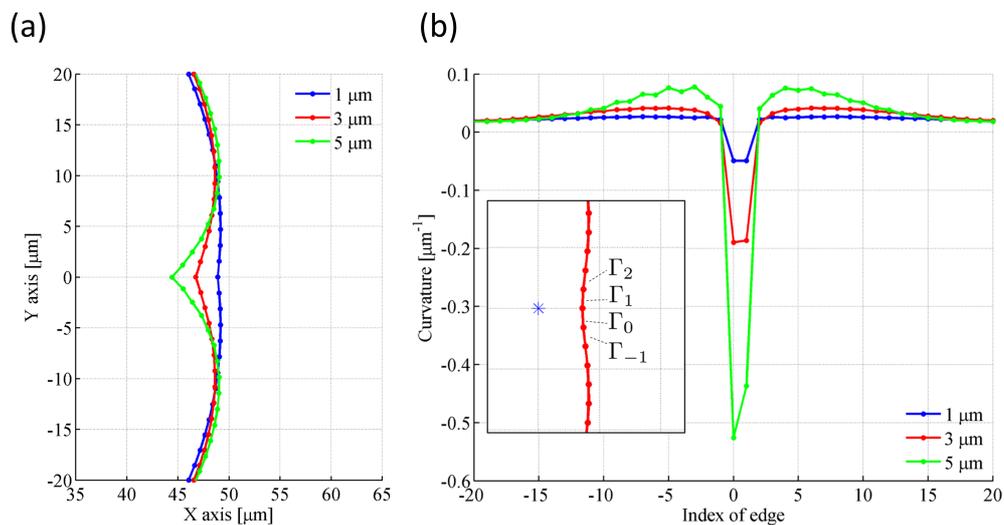
Fig. 6.15. Equilibrium state of the deformation and its curvature of the SLB when the
virtual cathode was located inside the SLB ($t = 6.25$ s). (a) Equilibrium state
of the deformation. The virtual cathode was located 1 μ m, 3 μ m, or 5 μ m
inside the interface of the SLB. (b) Equilibrium state of the curvature of the
SLB and the definition of the indices of the vertices.
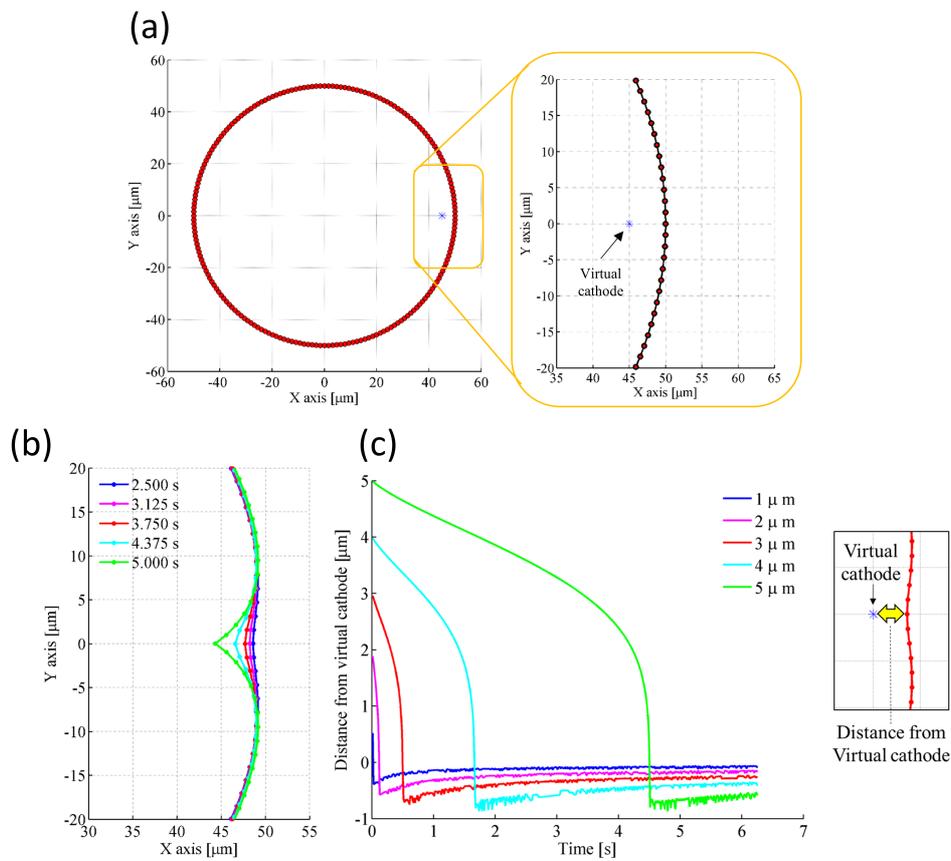
(a)

(b)
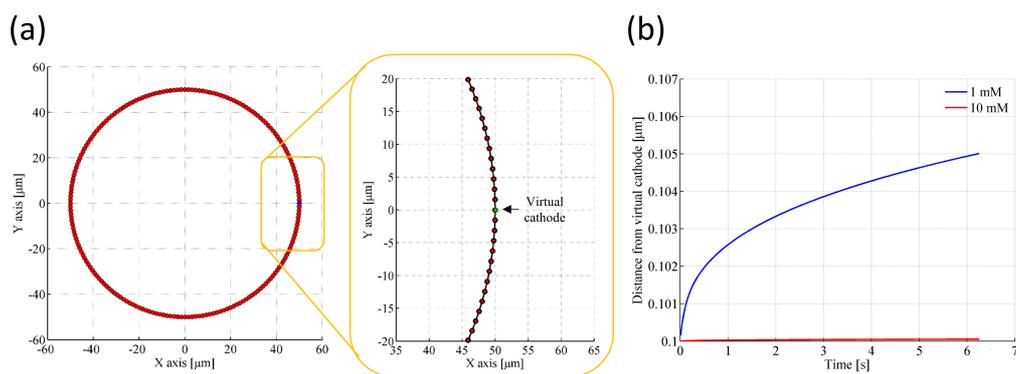
Fig. 6.16. Simulation results of the deformation of the SLB when the virtual cathode was
located outside the SLB. (a) Initial condition of the SLB and the location of
the virtual cathode. (b) Temporal change of the distance between the edge of
the SLB and the virtual cathode. The definition of the distance between the
edge of the SLB is same as Fig. 6.14.
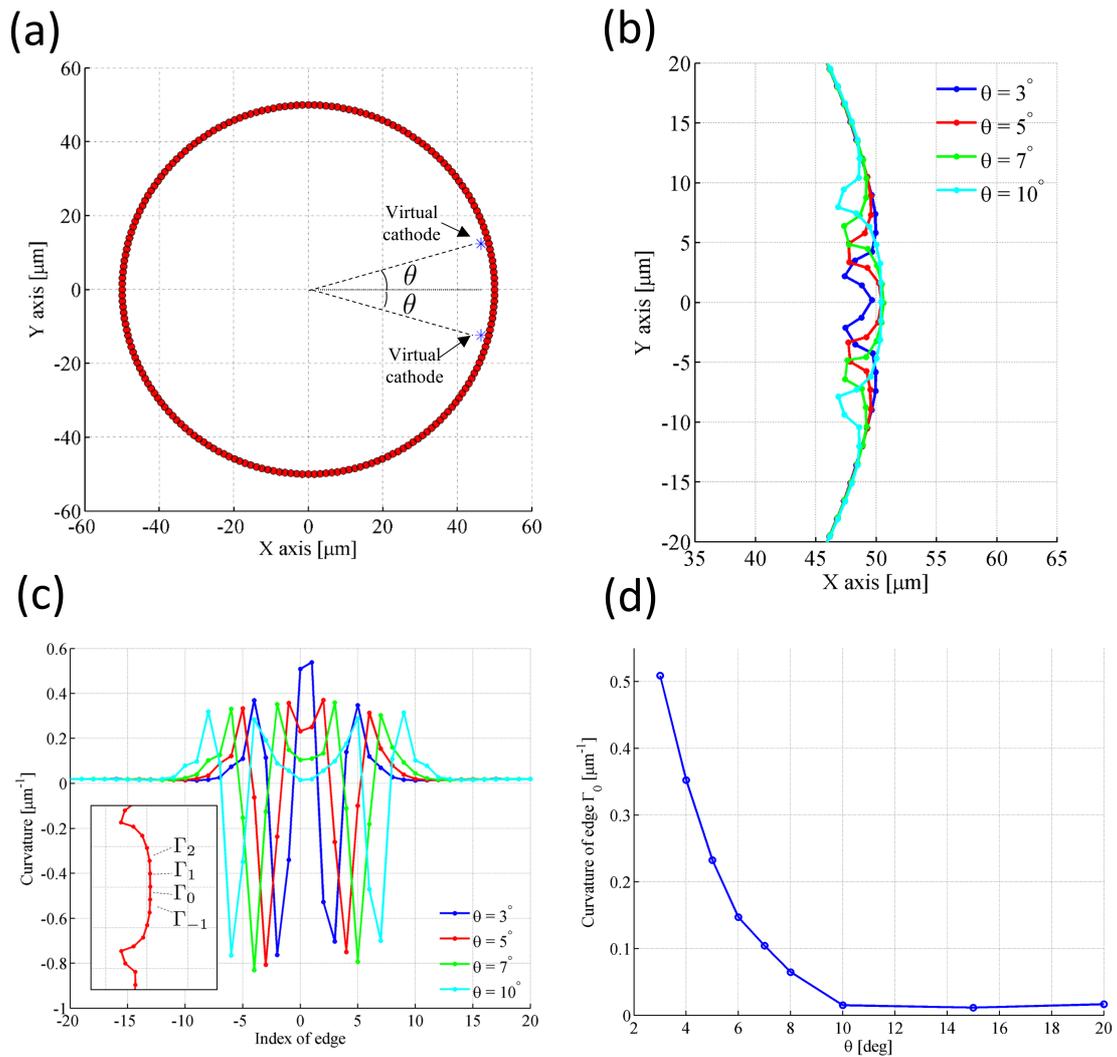
Fig. 6.17. Simulation results of the deformation of the SLB when two virtual cathodes were located inside the edge of the SLB. (a) Initial condition of the SLB and the location of the virtual cathode. (b) Deformation of the SLB at $t = 0.25s$. (c) Curvature of the SLB at $t = 0.25s$. (d) Relationship between the curvature of the edge Γ_0 and θ. Γ_0 is defined in (c).
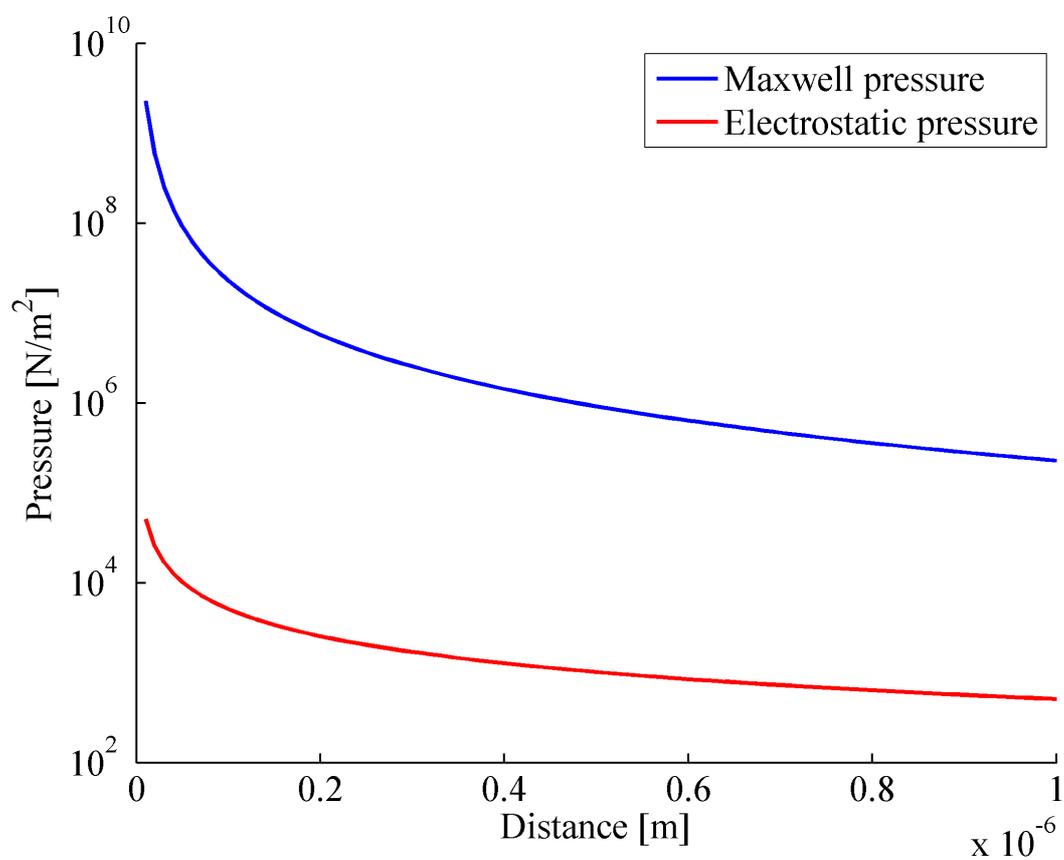
Fig. 6.18. Spatial distribution of electrostatic pressure and Maxwell pressure in 1 mM NaCl solution.

Chapter 7

Conclusion

7.1   Conclusion of this thesis

In this thesis, we have proposed new analysis and fabrication techniques for soft matter that can achieve operando analysis and the directed self-assembly of soft matter based on the spatiotemporal control of the electric field. An EB was used to generate the virtual cathode in aqueous solutions at the spatial scale of the self-assembled structures of soft matter.

In Chapter 2, current techniques of virtual electrode were overviewed and the basic concept of the virtual electrode induced by charged particle beams was introduced. For the physical implementation of the virtual electrode, a virtual cathode display system using an inverted EB lithography system was proposed and the physical effects of the EB-induced virtual cathode, such as electrical, chemical, and thermal effects, were discussed. By measuring the temperature rise of rhodamine B water solution, it was confirmed that the thermal effect around the EB-induced virtual cathode was small.

In Chapter 3, the electrostatic effects of the virtual cathode were discussed. The physical setup of the virtual cathode in an electrolyte solution was formulated, and the fundamental solutions of the electric field, spatial distributions of electrolytes, and diffusion of hydroxide ions generated by cathodic reactions were calculated. By using these fundamental solutions, the design method of the virtual cathode was proposed to achieve the target electric field or ionic concentrations by solving optimization problems. Finally, it was demonstrated that an increase and ionic shielding were induced around the EB-induced virtual cathode, as predicted by the calculation of the fundamental solutions.

In Chapter 4, the electrokinetic effects of the virtual cathode, such as EOF and electrophoresis, were investigated. The integrated model of hydrodynamics and electric field around the virtual cathode were proposed, and FEM simulations showed that EOFs could be induced around the EB-induced virtual cathode when the surface was electrically charged. Then, it was confirmed that EOFs were generated around the EB-induced virtual cathode by tracking the movement of nanoparticles. Finally, these electrokinetic effects were applied to the manipulation of a single nanoparticle, concentration patterning of nanoparticles, and elongation of DNA molecules.

Chapter 5 focused on surface reactions induced by the chemical and electrical

effects of an EB. It was demonstrated that MPC polymers were detached from an SiN membrane and glucose, sucrose, and PEI polymer molecules were deposited on the membrane in water through surface reactions of the EB-induced virtual cathode. Monte Carlo simulations of scattered electrons and the experimental results suggested that the detachment phenomenon of MPC polymers is due to the electrical effects of the EB and that the deposition phenomenon of the PEI polymers is due to chemical reactions induced by the kinetic energy of the EB. Therefore, it was confirmed that chemical and electrical effects were controlled by changing the acceleration voltage.

In Chapter 6, the proposed techniques were applied to the electromechanical control of lipid membrane domains and morphology. By controlling the surface reactions of the EB-induced virtual cathode, SLBs were dynamically patterned and the fluidity and re-spreading of the SLBs could be controlled by the dose amount of the EB. Moreover, the re-spreading of SLBs induced the directed self-assembly of the liquid-ordered phase, which contained rich ganglioside GM1 in DOPC/DPPC/cholesterol mixture. Finally, the dynamic and reversible deformation of stacked lipid bilayers was achieved by Maxwell's stress around the EB-induced virtual cathode, which would be applicable to the spatiotemporal measurements of the mechanical properties of SLBs.

7.2   Future directions based on this study

This thesis demonstrated the operando analysis and directed self-assembly of DNA molecules and lipid bilayers in aqueous solutions by using electrostatic and electrokinetic phenomena as well as the surface reactions of an EB-induced virtual cathode. Therefore, the proposed method could be applied to the operando analysis of other soft matter, such as stimuli-responsive polymers. Since the proposed techniques enabled the simultaneous stimulation and observation of soft matter and the stimulation was at the submicrometer scale, the spatial dependencies of the stimuli response of the soft matter could be measurable by the proposed techniques. Such measurements could contribute to the material design of soft matter such as stimuli-responsive materials.

Moreover, the EB-induced virtual cathode can generate various electric field shapes, which can be easily changed by scanning an EB. Therefore, the proposed method could also be applied to the rapid prototyping of electrical devices such as multi electrode arrays.

Acknowledgements

References

[1] M. Doi: "Soft matter physics", Oxford University Press (2013).

[2] Y. Kimura: "Microrheology of soft matter", Journal of the Physical Society of Japan, **78**, 4 (2009).

[3] A. Caspi, M. Elbaum, R. Granek, A. Lachish and D. Zbaida: "Semiflexible polymer network: A view from inside", Physical Review Letters, **80**, 5, pp. 1106–1109 (1998).

[4] I. Y. Wong, M. L. Gardel, D. R. Reichman, E. R. Weeks, M. T. Valentine, A. R. Bausch and D. A. Weitz: "Anomalous diffusion probes microstructure dynamics of entangled F-actin networks", Physical Review Letters, **92**, 17, pp. 178101–1 (2004).

[5] D. Mizuno, Y. Kimura and R. Hayakawa: "Electrophoretic microrheology in a dilute lamellar phase of a nonionic surfactant", Physical Review Letters, **87**, 8, p. 088104 (2001).

[6] A. R. Bausch, W. Möller and E. Sackmann: "Measurement of local viscoelasticity and forces in living cells by magnetic tweezers", Biophysical Journal, **76**, 1, pp. 573–579 (1999).

[7] R. R. Brau, J. M. Ferrer, H. Lee, C. E. Castro, B. K. Tam, P. B. Tarsa, P. Matsudaira, M. C. Boyce, R. D. Kamm and M. J. Lang: "Passive and active microrheology with optical tweezers", Journal of Optics A: Pure and Applied Optics, **9**, 8, pp. S103–S112 (2007).

[8] J. Alcaraz, L. Buscemi, M. Grabulosa, X. Trepat, B. Fabry, R. Farré and D. Navajas: "Microrheology of human lung epithelial cells measured by atomic force microscopy", Biophysical Journal, **84**, 3, pp. 2071–2079 (2003).

[9] R. Pease and S. Chou: "Lithography and other patterning techniques for future electronics", Proceedings of the IEEE, **96**, 2, pp. 248–270 (2008).

[10] G. M. Whitesides, E. Ostuni, X. Jiang and D. E. Ingber: "Soft lithography in biology and biochemistry", Annual Review of Biomedical Engineering, **3**, pp. 335–73 (2001).

[11] C. Vieu, F. Carcenac, A. Pepin, Y. Chen, M. Mejias, A. Lebib, L. Manin-Ferlazzo, L. Couraud and H. Launois: "Electron beam lithography - Resolution limits and applications", Applied Surface Science, **164**, pp. 111–117 (2000).

[12] G. M. Whitesides: "Self-assembly at all scales", Science, **295**, 5564, pp. 2418–2421 (2002).

[13] J. S. Lindsey: "Self-assembly in synthetic routes to molecular devices. Biological principles and chemical perspectives: a review" (1991).

[14] P. W. K. Rothemund: "Folding DNA to create nanoscale shapes and patterns",

Nature, **440**, 7082, pp. 297–302 (2006).

[15] M. Antonietti and S. Förster: "Vesicles and liposomes: A self-assembly principle beyond lipids" (2003).

[16] D. J. Lohse and N. Hadjichristidis: "Microphase separation in block copolymers", Current Opinion in Colloid & Interface Science, **2**, 2, pp. 171–176 (1997).

[17] S. Ouk Kim, H. H. Solak, M. P. Stoykovich, N. J. Ferrier, J. J. de Pablo and P. F. Nealey: "Epitaxial self-assembly of block copolymers on lithographically defined nanopatterned substrates", Nature, **424**, 6947, pp. 411–414 (2003).

[18] F. Ercole, T. P. Davis and R. A. Evans: "Photo-responsive systems and biomaterials: photochromic polymers, light-triggered self-assembly, surface modification, fluorescence modulation and beyond", Polym. Chem., **1**, 1, pp. 37–54 (2010).

[19] T. Hamada, R. Sugimoto, T. Nagasaki and M. Takagi: "Photochemical control of membrane raft organization", Soft Matter, **7**, 1, pp. 220–224 (2011).

[20] M. A. Bañares: "Operando methodology: Combination of in situ spectroscopy and simultaneous activity measurements under catalytic reaction conditions", Catalysis Today, Vol. 100, pp. 71–77 (2005).

[21] M. A. Bañares: "Operando spectroscopy: The knowledge bridge to assessing structure-performance relationships in catalyst nanoparticles", Advanced Materials, **23**, 44, pp. 5293–5301 (2011).

[22] A. Urakawa: "Trends and advances in Operando methodology", Current Opinion in Chemical Engineering, **12**, pp. 31–36 (2016).

[23] D. Fygenson, J. Marko and A. Libchaber: "Mechanics of microtubule-based membrane extension", Physical Review Letters, **79**, 22, pp. 4497–4500 (1997).

[24] R. Bar-Ziv, E. Moses and P. Nelson: "Dynamic excitations in membranes induced by optical tweezers.", Biophysical Journal, **75**, 1, pp. 294–320 (1998).

[25] Y. Shitamichi, M. Ichikawa and Y. Kimura: "Mechanical properties of a giant liposome studied using optical tweezers", Chemical Physics Letters, **479**, 4-6, pp. 274–278 (2009).

[26] S. Ota, S. Wang, Y. Wang, X. Yin and X. Zhang: "Lipid bilayer-integrated optoelectronic tweezers for nanoparticle manipulations", Nano Letters, **13**, 6, pp. 2766–2770 (2013).

[27] T. Okada and T. Ogura: "Nanoscale imaging of untreated mammalian cells in a medium with low radiation damage using scanning electron-assisted dielectric microscopy", Scientific Reports, **6**, July, p. 29169 (2016).

[28] E. U. Donev and J. T. Hastings: "Electron-beam-induced deposition of platinum from a liquid precursor.", Nano letters, **9**, 7, pp. 2715–8 (2009).

[29] T. Hoshino and K. Mabuchi: "Closed-looped in situ nano processing on a culturing cell using an inverted electron beam lithography system.", Biochemical and biophysical research communications, **432**, 2, pp. 345–349 (2013).

[30] B. Murty, P. Shankar, R. Baldev, B. Rath and J. Murday: "Textbook of nanoscience and nanotechnology", Springer (2013).

[31] J. Ferguson and A. W. Mau: "Spontaneous and stimulated emission from dyes. Spectroscopy of the neutral molecules of acridine orange, proflavine, and rhodamine B", Australian Journal of Chemistry, **26**, 8, pp. 1617–1624 (1973).

[32] H. D. Duong and J. I. Rhee: "Exploitation of thermo-effect of rhodamine B entrapped in sol-gel matrix and silica gel for temperature detection", Sensors and Actuators, B: Chemical, **124**, 1, pp. 18–23 (2007).

[33] V. M. Chauhan, R. H. Hopper, S. Z. Ali, E. M. King, F. Udrea, C. H. Oxley and J. W. Aylott: "Thermo-optical characterization of fluorescent rhodamine B based temperature-sensitive nanosensors using a CMOS MEMS micro-hotplate", Sensors and Actuators, B: Chemical, **192**, pp. 126–133 (2014).

[34] J. Sakakibara, K. Hishida and M. Maeda: "Measurements of thermally stratified pipe flow using image-processing techniques", Experiments in Fluids, **16**, 2, pp. 82–96 (1993).

[35] D. Ross, M. Gaitan and L. E. Locascio: "Temperature measurement in microfluidic systems using a temperature-dependent fluorescent dye", Analytical Chemistry, **73**, 17, pp. 4117–4123 (2001).

[36] W. Haynes: "CRC Handbook of chemistry and physics, 95th edition, 2014-2015", Vol. 54 (2014).

[37] G. N. Watson: "A treatise on the theory of Bessel functions", Cambridge University Press, 2 edition (1944).

[38] M. M. Martin and L. Lindqvist: "The pH dependence of fluorescein fluorescence", Journal of Luminescence, **10**, 6, pp. 381–390 (1975).

[39] R. Sjöback, J. Nygren and M. Kubista: "Absorption and fluorescence properties of fluorescein", Spectrochimica Acta Part A: Molecular and Biomolecular Spectroscopy, **51**, 6, pp. L7–L21 (1995).

[40] D. F. H. Wallach, D. M. Surgenor, J. Soderberg and E. Delano: "Preparation and properties of 3, 6-Dihydroxy-2,4-bis-[N,N' -di-(carboxymethyl)-aminomethyl] fluoran Utilization for the ultramicrodetermination of calcium", Analytical chemistry, **31**, 3, pp. 456–460 (1959).

[41] D. F. H. Wallach and T. L. Steck: "Fluorescence techniques in the microdetermination of metals in biological materials", Analytical chemistry, **35**, 8, pp. 1035–1044 (1963).

[42] T. Hoshino, H. Miyazako, A. Nakayama, A. Wagatsuma and K. Mabuchi: "Electron beam induced fine virtual electrode for mechanical strain microscopy of living cell", Sensors and Actuators, B: Chemical, **236**, (2016).

[43] M. M. Meighan, S. J. R. Staton and M. A. Hayes: "Bioanalytical separations using electric field gradient techniques.", Electrophoresis, **30**, 5, pp. 852–65 (2009).

[44] J. Voldman: "Electrical forces for microscale cell manipulation.", Annual review of biomedical engineering, **8**, pp. 425–54 (2006).

[45] X. Wang, C. Cheng, S. Wang and S. Liu: "Electroosmotic pumps and their applications in microfluidic systems", Microfluidics and Nanofluidics, **6**, 2, pp. 1–34

(2009).

[46] H. Stone, A. Stroock and A. Ajdari: "Engineering flows in small devices", Annual Review of Fluid Mechanics, **36**, 1, pp. 381–411 (2004).

[47] T. G. Henares, S. Funano, K. Sueyoshi, T. Endo and H. Hisamoto: "Advancements in capillary-assembled microchip (CAs-CHIP) development for multiple analyte sensing and microchip electrophoresis", Analytical Sciences, **30**, 1, pp. 7–15 (2014).

[48] A. Kumar, S. J. Williams, H.-S. Chuang, N. G. Green and S. T. Wereley: "Hybrid opto-electric manipulation in microfluidics-opportunities and challenges.", Lab on a chip, **11**, 13, pp. 2135–2148 (2011).

[49] S. J. Williams, A. Kumar and S. T. Wereley: "Electrokinetic patterning of colloidal particles with optical landscapes.", Lab on a chip, **8**, 11, pp. 1879–1882 (2008).

[50] A. Kumar, J.-S. Kwon, S. J. Williams, N. G. Green, N. K. Yip and S. T. Wereley: "Optically modulated electrokinetic manipulation and concentration of colloidal particles near an electrode surface.", Langmuir : the ACS journal of surfaces and colloids, **26**, 7, pp. 5262–72 (2010).

[51] R. Hayward, D. Saville and I. Aksay: "Electrophoretic assembly of colloidal crystals with optically tunable micropatterns", Nature, **404**, March (2000).

[52] P. Y. Chiou, A. T. Ohta and M. C. Wu: "Massively parallel manipulation of single cells and microparticles using optical images.", Nature, **436**, 7049, pp. 370–372 (2005).

[53] H. Hwang and J.-K. Park: "Optoelectrofluidic platforms for chemistry and biology.", Lab on a chip, **11**, 1, pp. 33–47 (2011).

[54] W. Choi, S.-W. Nam, H. Hwang, S. Park and J.-K. Park: "Programmable manipulation of motile cells in optoelectronic tweezers using a grayscale image", Applied Physics Letters, **93**, 14, p. 143901 (2008).

[55] R. Daw and J. Finkelstein: "Opto-electrokinetic manipulation for high-performance on-chip bioassays", Lab on a chip, **12**, 23, pp. 4955–9 (2006).

[56] H. Hwang and J.-K. Park: "Rapid and selective concentration of microparticles in an optoelectrofluidic platform.", Lab on a chip, **9**, 2, pp. 199–206 (2009).

[57] H. Hwang and J.-K. Park: "Dynamic light-activated control of local chemical concentration in a fluid.", Analytical chemistry, **81**, 14, pp. 5865–70 (2009).

[58] H. Hwang, H. Chon, J. Choo and J.-K. Park: "Optoelectrofluidic sandwich immunoassays for detection of human tumor marker using surface-enhanced Raman scattering.", Analytical chemistry, **82**, 18, pp. 7603–10 (2010).

[59] H. Hwang and J.-K. Park: "Measurement of molecular diffusion based on optoelectrofluidic fluorescence microscopy.", Analytical chemistry, **81**, 21, pp. 9163–7 (2009).

[60] H. Hwang, Y.-J. Choi, W. Choi, S.-H. Kim, J. Jang and J.-K. Park: "Interactive manipulation of blood cells using a lens-integrated liquid crystal display based optoelectronic tweezers system.", Electrophoresis, **29**, 6, pp. 1203–12 (2008).

[61] A. Jamshidi, S. L. Neale, K. Yu, P. J. Pauzauskie, P. J. Schuck, J. K. Valley, H.-Y.

Hsu, A. T. Ohta and M. C. Wu: "NanoPen: dynamic, low-power, and light-actuated patterning of nanoparticles.", Nano letters, **9**, 8, pp. 2921–5 (2009).

[62] B. J. Kirby: "Micro- and nanoscale fluid mechanics: Transport in microfluidic devices", Cambridge University Press (2010).

[63] D. Drouin, A. Couture, D. Joly and X. Tastet: "CASINO V2. 42-A fast and easy-to-use modeling tool for scanning electron microscopy and microanalysis users", Scanning, **29**, 3, pp. 92–101 (2007).

[64] H. Kawakita, T. Uneyama, M. Kojima, K. Morishima, Y. Masubuchi and H. Watanabe: "Formation of globules and aggregates of DNA chains in DNA/polyethylene glycol/monovalent salt aqueous solutions.", The Journal of chemical physics, **131**, 9, p. 094901 (2009).

[65] N. Jaffrezic-Renault, A. De, P. Clechet and A. Maaref: "Study of the silicon nitride/aqueous electrolyte interface on colloidal aqueous suspensions and on electrolyte/insulator/semiconductor structures", Colloids and Surfaces, **36**, 1, pp. 59–68 (1989).

[66] L. Bousse and S. Mostarshed: "The zeta potential of silicon nitride thin films", Journal of Electroanalytical Chemistry and Interfacial Electrochemistry, **302**, 1-2, pp. 269–274 (1991).

[67] J. Suh, H.-J. Paik and B. K. Hwang: "Ionization of poly(ethylenimine) and poly(allylamine) at various pH's", Bioorganic Chemistry, **22**, 3, pp. 318–327 (1994).

[68] Y. Nawa, W. Inami, A. Chiba, A. Ono, A. Miyakawa, Y. Kawata, S. Lin and S. Terakawa: "Dynamic and high-resolution live cell imaging by direct electron beam excitation.", Optics express, **20**, 5, pp. 5629–35 (2012).

[69] C. Sato, S. Manaka, D. Nakane, H. Nishiyama, M. Suga, T. Nishizaka, M. Miyata and Y. Maruyama: "Rapid imaging of mycoplasma in solution using Atmospheric Scanning Electron Microscopy (ASEM).", Biochemical and biophysical research communications, **417**, 4, pp. 1213–8 (2012).

[70] H. Sugi, H. Minoda, Y. Inayoshi, F. Yumoto, T. Miyakawa, Y. Miyauchi, M. Tanokura, T. Akimoto, T. Kobayashi, S. Chaen and S. Sugiura: "Direct demonstration of the cross-bridge recovery stroke in muscle thick filaments in aqueous solution by using the hydration chamber.", Proceedings of the National Academy of Sciences of the United States of America, **105**, 45, pp. 17396–401 (2008).

[71] T. Ogura: "Direct observation of unstained wet biological samples by scanning-electron generation X-ray microscopy.", Biochemical and biophysical research communications, **391**, 1, pp. 198–202 (2010).

[72] R. F. Egerton, P. Li and M. Malac: "Radiation damage in the TEM and SEM.", Micron (Oxford, England : 1993), **35**, 6, pp. 399–409 (2004).

[73] D. Phifer, L. Tuma, T. Vystavel, P. Wandrol and R. J. Young: "Improving SEM imaging performance using beam deceleration", Microscopy Today, **17**, 04, pp. 40–49 (2009).

[74] M. Bazant and T. Squires: "Induced-charge electrokinetic phenomena: Theory and

microfluidic applications", Physical Review Letters, **92**, 6, p. 066101 (2004).

[75] D. Falconnet, G. Csucs, H. M. Grandin and M. Textor: "Surface engineering approaches to micropattern surfaces for cell-based assays.", Biomaterials, **27**, 16, pp. 3044–63 (2006).

[76] Z. Ma, Z. Mao and C. Gao: "Surface modification and property analysis of biomedical polymers used for tissue engineering.", Colloids and surfaces. B, Biointerfaces, **60**, 2, pp. 137–57 (2007).

[77] T. Hoshino, A. Higashi, T. Konno, K. Ishihara and K. Morishima: "Cell-driven three-dimensional manipulation of microparts for a microassembly", Japanese Journal of Applied Physics, **49**, 6, p. 06GM03 (2010).

[78] J.-I. Edahiro, K. Sumaru, Y. Tada, K. Ohi, T. Takagi, M. Kameda, T. Shinbo, T. Kanamori and Y. Yoshimi: "In situ control of cell adhesion using photoresponsive culture surface.", Biomacromolecules, **6**, 2, pp. 970–4 (2005).

[79] G. Kumar, C.-C. Ho and C. C. Co: "Guiding cell migration using one-way micropattern arrays", Advanced Materials, **19**, 8, pp. 1084–1090 (2007).

[80] H. Kaji, K. Tsukidate, T. Matsue and M. Nishizawa: "In situ control of cellular growth and migration on substrates using microelectrodes.", Journal of the American Chemical Society, **126**, 46, pp. 15026–7 (2004).

[81] X. Jiang, D. a. Bruzewicz, A. P. Wong, M. Piel and G. M. Whitesides: "Directing cell migration with asymmetric micropatterns.", Proceedings of the National Academy of Sciences of the United States of America, **102**, 4, pp. 975–8 (2005).

[82] M. Junkin, S. L. Leung, S. Whitman, C. C. Gregorio and P. K. Wong: "Cellular self-organization by autocatalytic alignment feedback.", Journal of cell science, **124**, Pt 24, pp. 4213–20 (2011).

[83] T.-H. Chen, X. Zhu, L. Pan, X. Zeng, A. Garfinkel, Y. Tintut, L. L. Demer, X. Zhao and C.-M. Ho: "Directing tissue morphogenesis via self-assembly of vascular mesenchymal cells.", Biomaterials, **33**, 35, pp. 9019–26 (2012).

[84] P. Krsko, S. Sukhishvili, M. Mansfield, R. Clancy and M. Libera: "Electron-beam surface-patterned poly(ethylene glycol) microhydrogels", Langmuir, **19**, 14, pp. 5618–5625 (2003).

[85] Y. Wang, E. Firlar, X. Dai and M. Libera: "Poly(ethylene glycol) as a biointeractive electron-beam resist", Journal of Polymer Science Part B: Polymer Physics, **51**, 21, pp. 1543–1554 (2013).

[86] B. Brough, K. L. Christman, T. S. Wong, C. M. Kolodziej, J. G. Forbes, K. Wang, H. D. Maynard and C.-M. Ho: "Surface initiated actin polymerization from top-down manufactured nanopatterns", Soft Matter, **3**, 5, p. 541 (2007).

[87] K. L. Christman, E. Schopf, R. M. Broyer, R. C. Li, Y. Chen, H. D. Maynard, C. E. Young, V. Dri and L. Angeles: "Positioning multiple proteins at the nanoscale with electron beam cross-linked functional polymers", Journal of the American Chemical Society, **131**, 2, pp. 521–527 (2009).

[88] M. A. C. Stuart, W. T. S. Huck, J. Genzer, M. Müller, C. Ober, M. Stamm, G. B.

Sukhorukov, I. Szleifer, V. V. Tsukruk, M. Urban, F. Winnik, S. Zauscher, I. Luzinov and S. Minko: "Emerging applications of stimuli-responsive polymer materials.", Nature materials, **9**, 2, pp. 101–13 (2010).

[89] M. A. Cole, N. H. Voelcker, H. Thissen and H. J. Griesser: "Stimuli-responsive interfaces and systems for the control of protein-surface and cell-surface interactions.", Biomaterials, **30**, 9, pp. 1827–50 (2009).

[90] K. Ishihara, T. Ueda and N. Nakabayashi: "Preparation of phospholipid polymers and their properties as polymer hydrogel membranes", Polymer Journal, **22**, 5, pp. 355–360 (1990).

[91] J. Sakakibara, K. Hishida and M. Maeda: "Experiments in fluids measurements of thermally stratified pipe flow using image-processing techniques", Experiments in Fluids, **96**, 2, pp. 82–96 (1993).

[92] J. N. Israelachvili: "Intermolecular and surface forces", Academic Press, New York, 3rd edition (2011).

[93] T. Hoshino and K. Morishima: "Electron-beam direct processing on living cell membrane", Applied Physics Letters, **99**, 17, p. 174102 (2011).

[94] T. Hoshino, H. Miyazako, A. Nakayama, A. Wagatsuma and K. Mabuchi: "Electron beam induced fine virtual electrode for mechanical strain microscopy of living cell", Sensors and Actuators, B: Chemical, **236**, pp. 659–667 (2016).

[95] A. R. Vancha, S. Govindaraju, K. V. L. Parsa, M. Jasti, M. González-García and R. P. Ballestero: "Use of polyethyleneimine polymer in cell culture as attachment factor and lipofection enhancer.", BMC biotechnology, **4**, 1, p. 23 (2004).

[96] R. Bahulekar, N. Ayyangar and S. Ponrathnam: "Polyethyleneimine in immobilization of biocatalysts", Enzyme and Microbial Technology, **13**, 11, pp. 858–868 (1991).

[97] U. Lungwitz, M. Breunig, T. Blunk and A. Göpferich: "Polyethylenimine-based non-viral gene delivery systems.", European journal of pharmaceutics and biopharmaceutics : official journal of Arbeitsgemeinschaft für Pharmazeutische Verfahrenstechnik e.V, **60**, 2, pp. 247–66 (2005).

[98] E. Evans and W. Rawicz: "Entropy-driven tension and bending elasticity in condensed-fluid membranes", Physical Review Letters, **64**, 17, pp. 2094–2097 (1990).

[99] W. Rawicz, K. Olbrich, T. McIntosh, D. Needham and E. Evans: "Effect of chain length and unsaturation on elasticity of lipid bilayers", Biophysical Journal, **79**, 1, pp. 328–339 (2000).

[100] E. Sackmann: "Supported membranes: Scientific and practical applications", Science, **271**, 5245, pp. 43–48 (1996).

[101] J. Rädler, H. Strey and E. Sackmann: "Phenomenology and kinetics of lipid bilayer spreading on hydrophilic surfaces", Langmuir, **11**, 11, pp. 4539–4548 (1995).

[102] H. Nabika, A. Fukasawa and K. Murakoshi: "Control of the structure of self-spreading lipid membrane by changing electrolyte concentration", Langmuir, **22**, 26, pp. 10927–10931 (2006).

[103] K. Furukawa, H. Nakashima, Y. Kashimura and K. Torimitsu: "Microchannel device using self-spreading lipid bilayer as molecule carrier.", Lab on a chip, **6**, 8, pp. 1001–6 (2006).

[104] C. Liu, C. F. Monson, T. Yang, H. Pace and P. S. Cremer: "Protein separation by electrophoretic-electroosmotic focusing on supported lipid bilayers", Analytical Chemistry, **83**, 20, pp. 7876–7880 (2011).

[105] C. F. Monson, H. P. Pace, C. Liu and P. S. Cremer: "Supported bilayer electrophoresis under controlled buffer conditions", Analytical Chemistry, **83**, 6, pp. 2090–2096 (2011).

[106] H. P. Pace, S. D. Sherrod, C. F. Monson, D. H. Russell and P. S. Cremer: "Coupling supported lipid bilayer electrophoresis with matrix-assisted laser desorption/ionization-mass spectrometry imaging", Analytical Chemistry, **85**, 12, pp. 6047–6052 (2013).

[107] H. Nabika, T. Motegi and K. Murakoshi: "Single molecule tracking of cholera-toxin subunit B on GM1-ganlioside containing lipid bilayer", e-Journal of Surface Science and Nanotechnology, **7**, pp. 74–77 (2009).

[108] M. Loose, E. Fischer-Friedrich, J. Ries, K. Kruse and P. Schwille: "Spatial regulators for bacterial cell division self-organize into surface waves in vitro", Science, **320**, 5877, pp. 789–792 (2008).

[109] J. T. Groves, N. Ulman and S. G. Boxer: "Micropattering fluid lipid bilayers on solid supports", Science, **275**, 1997, pp. 651–653 (1997).

[110] J. S. Hovis and S. G. Boxer: "Patterning and composition arrays of supported lipid bilayers by microcontact printing", Langmuir, **17**, 11, pp. 3400–3405 (2001).

[111] S. Lenhert, P. Sun, Y. Wang, H. Fuchs and C. A. Mirkin: "Massively parallel dip-pen nanolithography of heterogeneous supported phospholipid multilayer patterns" (2007).

[112] A. M. Smith, T. Huser and A. N. Parikh: "Dynamic recompartmentalization of supported lipid bilayers using focused femtosecond laser pulses", Journal of the American Chemical Society, **129**, 9, pp. 2422–2423 (2007).

[113] M. Mathieu, D. Schunk, S. Franzka, C. Mayer, E. Hasselbrink and N. Hartmann: "Direct laser patterning of soft matter: Photothermal processing of supported phospholipid multilayers with nanoscale precision", Small, **5**, 18, pp. 2099–2104 (2009).

[114] M. Roark and S. E. Feller: "Structure and dynamics of a fluid phase bilayer on a solid support as observed by a molecular dynamics computer simulation", Langmuir, **24**, 21, pp. 12469–12473 (2008).

[115] T. J. Zwang, W. R. Fletcher, T. J. Lane and M. S. Johal: "Quantification of the layer of hydration of a supported lipid bilayer", Langmuir, **26**, 7, pp. 4598–4601 (2010).

[116] I. Gözen, P. Dommersnes and A. Jesorka: "Lipid self-spreading on solid substrates", Surface Energy (Ed. by Mahmood Aliofkhazraei), InTech, chapter 12, pp. 337–371 (2015).

[117] S. Richardson: "Hele Shaw flows with a free boundary produced by the injection of fluid into a narrow channel", Journal of Fluid Mechanics, **56**, 4, pp. 609–618 (1972).

[118] K. Sakakibara and S. Yazaki: "A charge simulation method for the computation of Hele-Shaw problems", RIMS Kôkyûroku, **1957**, pp. 116–133 (2015).

[119] S. L. Veatch and S. L. Keller: "Separation of liquid phases in giant vesicles of ternary mixtures of phospholipids and cholesterol", Biophysical Journal, **85**, 5, pp. 3074–3083 (2003).

[120] T. Baumgart, G. Hunt, E. R. Farkas, W. W. Webb and G. W. Feigenson: "Fluorescence probe partitioning between Lo/Ld phases in lipid membranes", Biochimica et Biophysica Acta - Biomembranes, **1768**, 9, pp. 2182–2194 (2007).

[121] A. T. Hammond, F. A. Heberle, T. Baumgart, D. Holowka, B. Baird and G. W. Feigenson: "Crosslinking a lipid raft component triggers liquid ordered-liquid disordered phase separation in model plasma membranes.", Proceedings of the National Academy of Sciences of the United States of America, **102**, 18, pp. 6320–6325 (2005).

[122] Y. S. Ryu, N. J. Wittenberg, J. H. Suh, S. W. Lee, Y. Sohn, S. H. Oh, A. N. Parikh and S. D. Lee: "Continuity of monolayer-bilayer junctions for localization of lipid raft microdomains in model membranes", Scientific Reports, **6**, (2016).

[123] B. J. Kirby and E. F. Hasselbrink: "Zeta potential of microfluidic substrates: 1. Theory, experimental techniques, and effects on separations" (2004).

[124] A. Revil, P. A. Pezard and P. W. J. Glover: "Streaming potential in porous media: 1. Theory of the zeta potential", Journal of Geophysical Research, **104**, B9, p. 20021 (1999).

[125] B. A. Bezuglyi, N. A. Ivanova and A. Y. Zueva: "Laser-induced thermocapillary deformation of a thin liquid layer", Journal of Applied Mechanics and Technical Physics, **42**, 3, pp. 493–496 (2001).

[126] J. Pan, S. Tristram-Nagle, N. Kučerka and J. F. Nagle: "Temperature dependence of structure, bending rigidity, and bilayer interactions of dioleoylphosphatidylcholine bilayers", Biophysical Journal, **94**, 1, pp. 117–124 (2008).

[127] Y. Nojima and K. Iwata: "Viscosity heterogeneity inside lipid bilayers of single-component phosphatidylcholine liposomes observed with picosecond time-resolved fluorescence spectroscopy", Journal of Physical Chemistry B, **118**, 29, pp. 8631–8641 (2014).

Appendix A

Monte Carlo simulations of scattered electrons

To get the distribution of the scattered electrons as shown in Figs. 4.2 (a) and (b), the scattering processes of 10^7 electrons (2.5 keV) were simulated by CASINO ver. 2.4. In these simulations, there were three layers, the vacuum space, 100-nm-thick SiN layer and H2O layer. The thickness, density and chemical compositions of each layer were as shown in Table S1. The beam radius was set to 25 nm. Each electron was simulated until the electron energy was below 50 eV or the electron escaped from the surface of the SiN layer into the vacuum layer.

   Additionally, the scattering processes of 10^5 electrons (2.5 keV) were simulated by CASINO ver. 2.4. to get and approximate the distribution of the scattered electrons for the FEM simulations. The histograms of coordinates of stop-points of scattered electrons (except back scattered electrons) are shown in Fig. A. To represent these distributions as mathematical functions for FEM simulations, Kernel density estimation was used. We used Kernel Density Estimation Toolbox for MATLAB (distributed by Alexander Ihler, http://www.ics.uci.edu/ ihler/code/kde.html), and the histograms were approximated by Gaussian kernels as follows:

$$p_e(x, y, z) = \frac{1}{Nh} \sum_{i=1}^{N} K\left(\frac{x - x_i}{h}\right) K\left(\frac{y - y_i}{h}\right) K\left(\frac{z - z_i}{h}\right)$$

where $K(x) = \frac{1}{\sqrt{2\pi}} \exp\left(-\frac{x^2}{2}\right)$, N denotes the number of simulated electrons, (x_i, y_i, z_i) denotes the coordinates of the stop-point of the i-th electron, and $h = 10^{-8}$. The estimation results are also shown in Fig. A.

Table S1: Physical parameters for simulations

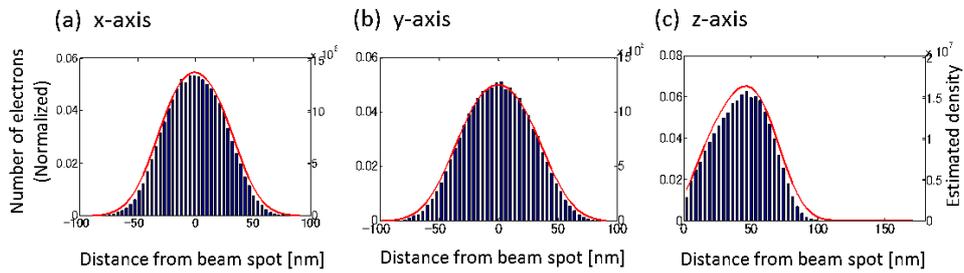|	Thickness [nm]	Density [g cm^{-3}]	Composition
Vacuum	100	1.00 x 10^{-5}	H$_2$
SiN	100	3.10	Si$_3$N$_4$
Water	Substrate	1.00	H$_2$O

Fig. A.1. Simulation results of spatial distributions of scattered electrons. Bar charts represent the histograms of scattered electrons, and solid lines represent estimated distribution function of electrons using a kernel density estimation method.

Appendix B

FEM simulations of electric field caused by EB irradiation

The electric field caused by EB irradiation was simulated by COMSOL Multiphysics 4.4. Geometrical definitions were as shown in Fig. B.1. The size and thickness of the SiN layer were almost the same as those of the actual SiN membrane.

There were two origins of the electrostatic potential, ionic charges in the water layer (ϕ_1), which generated an electric double layer, and negative charges of electrons in SiN layer (ϕ_2), which could generate electroosmotic flow in the water layer. As deionized water was used in the experiments, there were only two species of ions, H^+ and OH^-, in the water layer. The concentrations of these two ions were denoted as c_{H+} and c_{OH-}.

The electrostatic potential caused by ionic charges in the water layer (ϕ_1) satisfied the following Poisson equation,

$$\nabla^2 \phi_1 = -\frac{F(c_{H+} - c_{OH-})}{\epsilon_0 \epsilon_w},$$

where F is the Faraday constant, and ϵ_0 and ϵ_w are permittivities of the vacuum and water, respectively. Additionally, the concentration of ions (c_{H+}, c_{OH-}) satisfied the following conservation law.

$$\frac{\partial c_{H+}}{\partial t} + \nabla \cdot J_{H+} = 0$$

$$\frac{\partial c_{OH-}}{\partial t} + \nabla \cdot J_{OH-} = 0$$

The ionic currents of ions (J_{H+}, J_{OH-}) were defined as follows.

$$J_{H+} = -F c_{H+} \mu_{H+} \nabla \phi_1 - D_{H+} \nabla c_{H+}$$

$$J_{OH-} = -F c_{OH-} \mu_{OH-} \nabla \phi_1 - D_{OH-} \nabla c_{OH-}$$

Here, μ_{H+} and μ_{OH-} are the mobilities of H^+ and OH^-, and D_{H+} and D_{OH-} are the diffusion coefficients of H^+ and OH^-. The mobility was calculated from the following Nernst-Einstein relation.

$$\mu_{H+} = \frac{D_{H+}}{k_B T}, \quad \mu_{OH-} = \frac{D_{OH-}}{k_B T}$$

Table S2: Physical parameters for simulations

	Description of parameter	Value	Unit
ϵ_0	Permittivity of vacuum	8.85×10^{-12}	$m^{-3} kg^{-1} s^4 A^2$
ϵ_W	Permittivity of water	81.1	1
ϵ_S	Permittivity of SiN	7.10	1
F	Faraday constant	7.65×10^4	$C \, mol^{-1}$
k_B	Boltzmann constant	1.38×10^{-23}	$m^2 kg \, s^{-2} K^{-2}$
D_{H+}	Diffusion constant of hydrogen ion	8.70×10^{-9}	$m^2 s^{-1}$
D_{OH-}	Diffusion constant of hydroxide ion	4.50×10^{-9}	$m^2 s^{-1}$
ψ	Zeta potential of SiN in water (pH 7.0)	-4.00×10^{-2}	V
ρ	Charge of scattered electrons	-4.00×10^{-9}	C

The boundary conditions for ϕ_1 were as follows. First the voltages on the E_1 and E_4 boundaries were set to zero (earth), and ψ (zeta potential) respectively. Second, there were no ionic exchanges at E_4; that is, the following equations were satisfied at E_4.

$$\boldsymbol{n} \cdot c_{H+} = 0, \quad \boldsymbol{n} \cdot c_{OH-} = 0$$

Here, $\boldsymbol{n}$ denotes the normal vector. Finally, the densities of c_{H+} and c_{OH-} are fixed at 10^{-7} mol/L at E_1, E_2 and E_3.

The electrostatic potential caused by negative charges in the SiN layer (ϕ_2) satisfied the following Poisson equation,

$$\nabla^2 \phi_2 = -\frac{\rho_e(\boldsymbol{r})}{\epsilon(\boldsymbol{r})},$$

where $\epsilon(\boldsymbol{r})$ and $\rho_e(\boldsymbol{r})$ were defined as follows.

$$\epsilon(\boldsymbol{r}) = \begin{cases} \epsilon_0 & (R3) \\ \epsilon_0 \epsilon_S & (R2) \\ \epsilon_0 \epsilon_W & (R3) \end{cases}, \quad \rho_e(\boldsymbol{r}) = \begin{cases} \rho p_e(x, y, z) & (R2) \\ F(c_{H+} - c_{OH-}) & (R1) \\ 0 & (R3) \end{cases}$$

In the above equation, $p_e(x, y, z)$ is the probability distribution of scattered electrons estimated in Appendix A. The spatial charge density $\rho_e(\boldsymbol{r})$ in region R2 is described in Fig. B.1(c). The voltages of $E_1, E_2, E_3, E_5, E_6, E_8, E_9$ and E_{10} were each set to zero.

By coupling the above equations, the steady state solution of the electric field after the start of EB irradiation was simulated. The physical parameters for the simulations were as shown in Table S2. The temperature was fixed at 293 K.
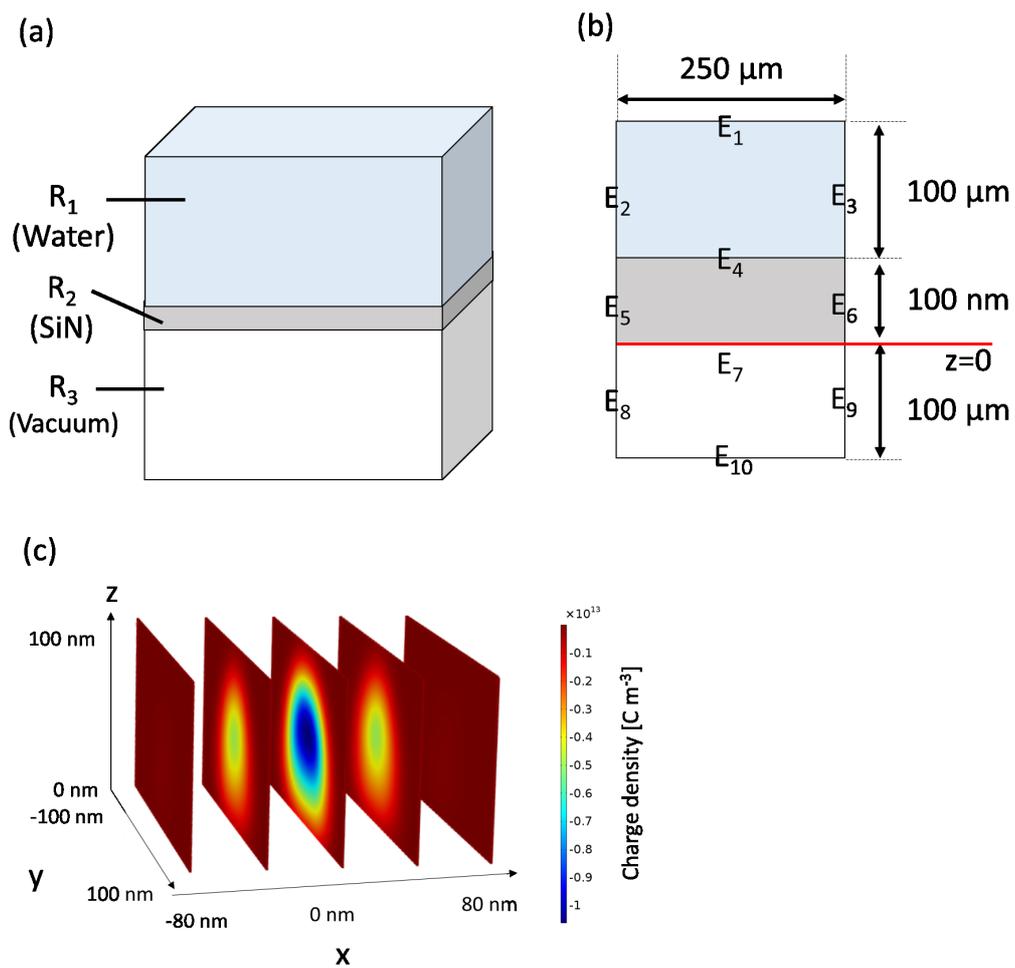
(a)

R₁
(Water)

R₂
(SiN)

R₃
(Vacuum)

(b)

(c)

Fig. B.1. Geometrical definitions for EB-induced electric field. (a) General view of the geometrical definitions. R1 to R3 represent the regions of each layer. (b) Side view of the geometrical definitions. E1 to E7 represent the boundaries. (c) Spatial charge density $\rho_e(\boldsymbol{r})$ in R2.

Appendix C

FEM simulations of thermal conduction and convection caused by EB irradiation

To estimate temperature rise caused by EB irradiation, the thermal conduction and convection were simulated by COMSOL Multiphysics 4.4. Geometrical definitions were as shown in Fig. C.1.

The thermal conductivity equation in the SiN membrane was represented as follows.

$$\rho_S C_s \frac{\partial T}{\partial t} = \nabla \cdot (k_S \nabla T) + Q$$

Similarly, the thermal conductivity equation in the water layer was as follows.

$$\rho_W C_W \frac{\partial T}{\partial t} + \rho_W C_W (\boldsymbol{u} \cdot \nabla T) = \nabla \cdot (k_W \nabla T)$$

The fluid velocity $\boldsymbol{u}$ satisfies the following Navier-Stokes equation with the external gravity force,

$$\rho_0 \frac{\partial \boldsymbol{u}}{\partial t} + \rho_W (\boldsymbol{u} \cdot \nabla)\boldsymbol{u} = -\nabla p + \mu \nabla^2 \boldsymbol{u} - (\rho_0 - \alpha \rho_0 (T - T_0))\boldsymbol{g},$$

where ρ_0 means the density of water at the reference temperature value $T_0 = 293$ K and α represents the thermal expansion coefficient of water.

The initial temperature was 293 K. We assumed that EB irradiation supplied 10 μW in R2, and the spatial distribution of the heat supply was determined by the distribution of scattered electrons estimated in Appendix A. The spatial distribution of heat supply was described in Fig. C.1 (c). Boundary conditions were as follows. The temperatures at E1 to E3 were each fixed to the initial value (293 K). The fluid velocity at E1 to E3 were fixed at zero, and the thermal exchange at E1 to E3 was zero; that is, the following equation was satisfied:

$$-\boldsymbol{n} \cdot (-k_W \nabla T) = 0,$$

where $\boldsymbol{n}$ denoted the normal vector.

By coupling the above equations, the electric field 1 s after the start of EB irradiation was simulated. The physical parameters for the simulations were as shown in Table S3. The time step (Δt) was 0.01 s.

The simulation results were as shown in Figs. C.2 and C.3. The 1 s EB spot irradiation could generate only several degrees Kelvin, and the velocity of thermal convection was much slower than that of observed flow. In addition, the effects of the temperature rises on the material properties were also small according to the simulation results. When the temperature rises from 293 to 296 K, the Reynolds number increases about 7%, the Debye length increases about 0.5% [62], and the zeta potential of silicon nitride increases about 6% [123, 124]. As compared to these increases, the coefficient of variation of the observed electroosmotic flow was much larger within 20 μm from the EB spot (about 50 %) as shown in Fig. 4.4 (b). These simulated results showed that the thermal effect on EB-induced flow was small.

Table S3: Physical parameters for simulations

|	Description of parameter	Value	Unit
g	Gravitational acceleration	9.80	m s^{-2}
ρ_0	Density of water	1.00×10^3	kg m^{-3}
ρ_S	Density of SiN	3.10×10^3	kg m^{-3}
k_W	Thermal conductivity of water	6.02×10^{-1}	W m^{-1} K^{-1}
k_S	Thermal conductivity of SiN	2.40×10^1	W m^{-1} K^{-1}
C_W	Heat capacity of water	4.18×10^3	J kg^{-1} K^{-1}
C_S	Heat capacity of SiN	6.80×10^2	J kg^{-1} K^{-1}
η	Viscosity coefficient of water	8.94×10^{-4}	Pa s
α	Thermal expansion coefficient of water	2.06×10^{-4}	K^{-1}
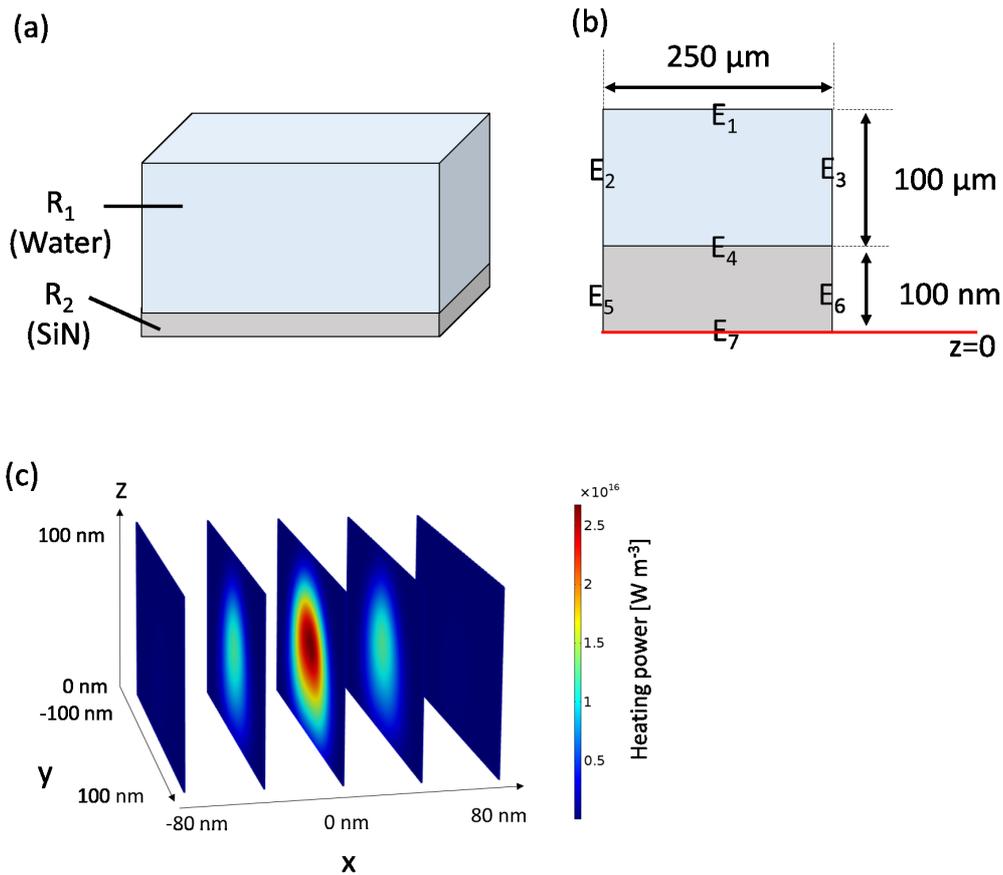
Fig. C.1. Geometrical definitions for thermal conduction and convection. (a) General view of the geometrical definitions. R1 to R3 represent the regions of each layer. (b) Side view of the geometrical definitions. E1 to E7 represent the boundaries. (c) Spatial distribution of the heat supply by EB irradiation in R2.
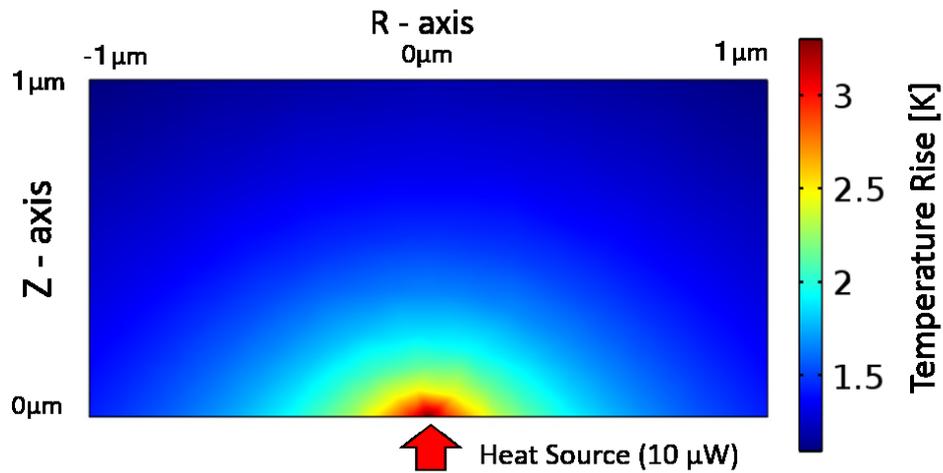
Fig. C.2. Simulation results of temperature rise 1 s after the start of EB irradiation. The temperature peaked around the heat source, but the temperature rise was only 3 K.

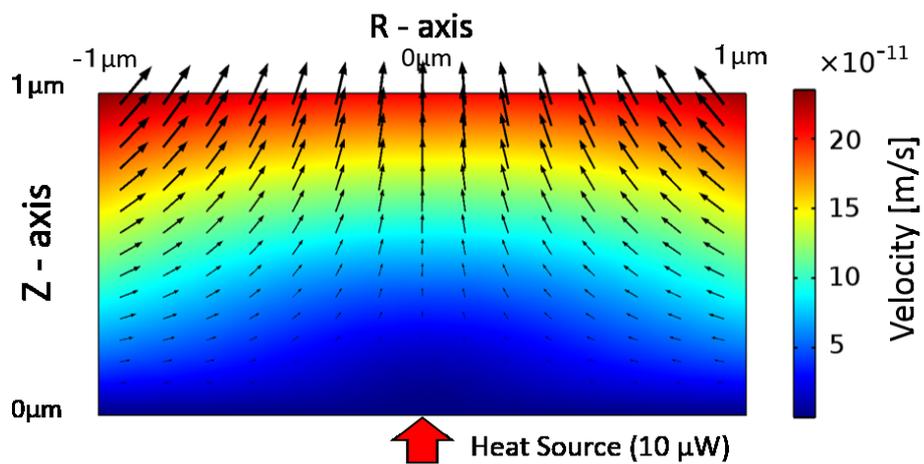
Fig. C.3. Simulation results of thermal convection 1 s after the start of EB irradiation. Black arrows are the vectors of flow velocity at each point, and the color map indicates the magnitude of the flow velocity. The order of the velocity was about 10^{-10} m/s between z = 0 μm and z = 1 μm, which was much smaller than the actual EB-induced fluid flow.

Appendix D

Evaluation of Marangoni effects on SLBs caused by EB irradiation

Marangoni effects are known as flow generation caused by a difference in the surface tension at an interface. Since surface tension usually depends on temperature, Marangoni effects can be observed when sufficient changes of temperature exist. According to Section 2.3 and Appendix C, temperature rise would occur around the EB-induced virtual cathode. In this section, the numerical simulations were performed to estimate the thermal effects on the Marangoni convection in SLBs.

In what follows, the physical setup of Marangoni flow of the SLB is introduced and an approximate solution of the velocity of the flow is derived referring to [125]. Fig. D.1 shows the physical setup of a single SLB in water solution. The bottom layer of the SLB is in contact with a solid substrate, and the upper one is contacted with the water solution. It is assumed that the SLB behaves as an incompressible flow. Since the viscosity of water ($1 \times 10^{-3}\,\mathrm{Pa \cdot s}$) is smaller than that of lipid membrane ($4 \times 10^{-2}\,\mathrm{Pa \cdot s}$), the viscosity of the water is not significant at the interface between the water solution and the SLB. Moreover, the Reynolds number of the SLB is very small and inertial effects of the SLB can be neglected. Under these assumptions, the steady flow of the SLB can be described by the Stokes equation $\nabla p = \eta \nabla^2 \boldsymbol{v}$, where $\boldsymbol{v} := (v_r, v_\theta, v_z)^T$, p, and η are the velocity, pressure and viscosity coefficient of the SLB, respectively. Considering the z-axial symmetry of the velocity, the Stokes equation can be written as follows:

$$\frac{\partial p}{\partial r} = \eta \left(\frac{\partial^2 v_r}{\partial r^2} + \frac{1}{r} \frac{\partial v_r}{\partial r} + \frac{\partial^2 v_r}{\partial z^2} \right)$$

$$\frac{\partial p}{\partial z} = \eta \left(\frac{\partial^2 v_z}{\partial r^2} + \frac{1}{r} \frac{\partial v_z}{\partial r} + \frac{\partial^2 v_z}{\partial z^2} \right).$$

Since the thickness of the SLB h $(4-5\,\mathrm{nm})$ is much smaller than the horizontal characteristic length L ($1\,\mu\mathrm{m}$), the latter equation can be negligible. Under this assumption, $\partial V_r/\partial r \ll \partial V_r/\partial z$ holds since $\partial V_r/\partial r \approx V_r/L, \partial V_r/\partial z \approx V_r/h$, and $h \ll L$. Therefore, we can assume that v_r depends mainly on z, and the above equations are approximated as the following equation.

$$\frac{\partial p}{\partial r} = \eta \frac{\partial^2 v_r}{\partial z^2}.$$

The boundary conditions for v_r at the bottom ($z = 0$) and above($z = h$) layers are written as follows:

$$v_r(z = 0) = 0, \quad \eta v_r(z = h) = \frac{\partial \sigma}{\partial r} = \frac{\partial \sigma}{\partial T} \frac{\partial T}{\partial r},$$

where σ denotes the surface tension of the SLB. According to [125], v_r can be calculated as follows:

$$v_r = \frac{1}{\eta} \frac{\partial \sigma}{\partial T} \frac{\partial T}{\partial r} \left(\frac{3}{4h} z^2 - \frac{1}{2} z \right).$$

Thus, the radial velocity of the Marangoni flow can be calculated from the following equation.

$$v_r(z = h) = \frac{h}{4\eta} \frac{\partial \sigma}{\partial T} \frac{\partial T}{\partial r}.$$

The thermal coefficient of the surface tension $\partial \sigma / \partial T$ can be estimated as follows. Stretch modulus K_A and surface tension σ of SLB satisfy a relational expression $K_A = 6\sigma$, and the streach modulus is 264 mN/m at 15 °C and 252 mN/m at 45 °C according to [126]. Therefore, $\partial \sigma / \partial T$ is about -7×10^{-5} N/(m · K). According to Section 2.3, the temperature difference between $r = 0 \, \mu$m and $r = 10 \, \mu$m was about 0.1 K (fluorescence intensity decreased about 0.2% and temperature change with the thermal coefficient of -2%/K) when the acceleration voltage and beam current were 2.5 kV and 4 nA, respectively. Therefore, $\partial T / \partial r$ is about -1×10^4 K/m. Viscosity inside the DOPC lipid bilayers was estimated to be about 0.05 Pa · s [127]. When it is assumed that the viscosity of the SLB η is about 0.05 Pa · s, the velocity v_r at $z = h = 4 \times 10^{-9}$ m is about $(-7 \times 10^{-5}) \times (-1 \times 10^4) \times 4 \times 10^{-9}/(4 \times 0.05) = 1.4 \times 10^{-8}$ m/s $\approx 1 \times 10^{-8}$ m/s. Therefore, the Marangoni effects would not be significant.
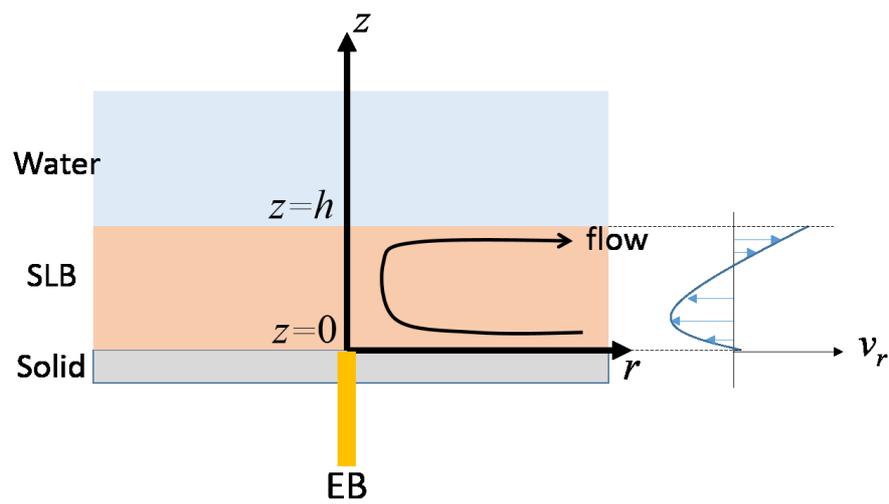
Fig. D.1. Schematic view of the Marangoni flow of the SLB.

Appendix E

List of Publications

Journal Papers

1. Takayuki Hoshino, **Hiroki Miyazako**, Atsuki Nakayama, Akira Wagatsuma, and Kunihiko Mabuchi, "Electron beam induced fine virtual electrode for mechanical strain microscopy of living cell," Sensors & Actuators : B. Chemical, Vol. 236, pp. 659—667, (2016).

2. **Hiroki Miyazako**, Kazuhiko Ishihara, Kunihiko Mabuchi, and Takayuki Hoshino, "In-situ Patterning of Organic Molecules in Aqueous Solutions Using an Inverted Electron-beam Lithography System," Japanese Journal of Applied Physics, Vol. 55, No. 6S1, pp. 06GL07, (2016).

3. Yutaka Hori, **Hiroki Miyazako**, Soichiro Kumagai, and Shinji Hara, "Coordinated Spatial Pattern Formation in Biomolecular Communication Networks," IEEE Transactions on Molecular, Biological, and Multi-Scale Communications, Vol. 1, No. 2, pp. 111—121, 2015.

4. **Hiroki Miyazako**, Kunihiko Mabuchi, and Takayuki Hoshino, "Spatiotemporal Control of Electrokinetic Transport in Nanofluidics Using an Inverted Electron-Beam Lithography System," Langmuir, Vol. 31, No. 23, pp. 6595—6603, 2015.

5. Yuichiro Yada, Tatsuya Haga, **Hiroki Miyazako**, Yuzo Takayama, Osamu Fukayama, Takayuki Hoshino, and Kunihiko Mabuchi, "Using Simulations to Evaluate Input-Site and Tetanized-Site Specificity of Tetanic Effect on Neuronal Networks," Electronics and Communications in Japan, Vol. 97, No. 8, pp. 72—80, 2014.

Other Articles

1. 宮廻裕樹，満渕邦彦，星野隆行，"第 33 回研究会優秀発表賞 電子線による局所電場印加システムを用いた高分子レオロジーのその場制御，" 化学とマイクロ・ナノシステム学会誌，Vol.15，No.2，pp.16—17，2016.10.

Presentations at International Conferences

1. **Hiroki Miyazako**, Kunihiko Mabuchi, and Takayuki Hoshino, "Dynamic Electromechanical Control of Biomolecules using a Nano Virtual Cathode Display," The 39th Annual International Conference of the IEEE Engineering in Medicine and Biology Society (EMBC2017), WeCT6-02.1, International Convention Center, Jeju Island, Korea, Jul. 2017. (査読あり，ポスター発表)

2. Takayuki Hoshino, Moto Yoshioka, Akira Wagatsuma, **Hiroki Miyazako**, and Kunihiko Mabuchi, "FINE VIRTUAL CATHODE DISPLAY FOR BIOMOLECULES CONTROL AND CELL NANO SURGERY," The 30th IEEE International Conference on Micro Electro Mechanical Systems (MEMS2017) , M-058, Las Vegas, USA, Jan. 2017. (査読あり，ポスター発表)

3. **Hiroki Miyazako**, Kunihiko Mabuchi, and Takayuki Hoshino, "Electrical Control for Self-Assembly of Biomaterials Using an Electron-Beam-Induced Virtual Electrode," 2016 MRS Fall Meeting & Exhibit, BM2.6.22, Hynes Convention Center, Boston, USA, Nov. 2016. (査読なし，ポスター発表)

4. Takayuki Hoshino, Moto Yoshioka, **Hiroki Miyazako**, Akira Wagatsuma, and Kunihiko Mabuchi, "VIRTUAL ELECTRODE FOR MECHANICAL STRAIN MICROSCOPY AND ELECTROPORATION ON INVERTED-¬ ELECTRON BEAM LITHOGRPHY," International Conference on Single Cell Research 2016, P2-24, University of Tokyo, Tokyo, Japan, Nov. 2016. (査読なし，ポスター発表)

5. Chihiro Okutani, Akira Wagatsuma, **Hiroki Miyazako**, Kunihiko Mabuchi, and Takayuki Hoshino, "TOPOGRAPHICAL STRUCTURE INDUCED FUNCTIONAL SINGLE CELL MIGRATION: A HOLE-SIDE WALL TRAPPING CELL AND ENHANCING CELL MIGRATION SPEED," International Conference on Single Cell Research 2016, P1-5 (Poster), University of Tokyo, Tokyo ,Japan, Nov. 2016. (査読なし，ポスター発表)

6. **Hiroki Miyazako**, Kunihiko Mabuchi, and Takayuki Hoshino, "In-situ Manipulation of Giant Liposomes Using an Electron-beam Induced Virtual Cathode," RSC Tokyo International Conference 2016, B31, Makuhari Messe, Chiba, Japan, Sep. 2016. (査読なし，ポスター発表)

7. **Hiroki Miyazako**, Kunihiko Mabuchi, and Takayuki Hoshino, "2D control of ionic transport and electrochemical reaction in nanofluidics using a highly focused electric field of an electron-beam" , The International Chemical Congress of Pacific Basin Societies (Pacifichem 2015), Hawaii, USA, Dec. 2015. (査読なし，口頭発表)

8. **Hiroki Miyazako**, Kazuhiko Ishihara, Kunihiko Mabuchi, and Takayuki Hoshino, "Dynamic Patterning of Organic Molecules in Aqueous Solutions Using an Inverted Electron-Beam Lithography System," The 28th International Microprocesses and

Nanotechnology Conference (MNC2015), 12D-6-2, Toyama International Conference Center, Toyama, Japan, Nov. 2015. (査読あり，口頭発表)

9. Moto Yoshioka, **Hiroki Miyazako**, Akira Wagatsuma, Kunihiko Mabuchi, and Takayuki Hoshino, "Single-Cell Membrane Surgery by Virtual Electrodes Using an Inverted Electron Beam Lithography System," 2014 IEEE/SICE International Symposium on System Integration (SII2014), SaA1C.2, Tokyo, Japan, Dec. 2014. (査読あり，口頭発表)

10. Takayuki Hoshino, **Hiroki Miyazako**, Akira Wagatsuma, and Kunihiko Mabuchi, "Measurement of Intracellular Strain Energy Distributions by Using Inverted-Electron Beam Lithography," The 26th International Microprocesses and Nanotechnology Conference (MNC 2014), 7P-11-93, Fukuoka, Japan, Nov. 2014. (査読あり，ポスター発表)

11. **Hiroki Miyazako**, Kunihiko Mabuchi, and Takayuki Hoshino, "2-D Electrokinetic Nano-manipulation for Aqueous Solution by Using a Simple Scanning Electron Beam," The 18th International Conference on Miniaturized Systems for Chemistry and Life Sciences (MicroTAS 2014), M.442e, San Antonio, USA, Oct. 2014. (査読あり，ポスター発表)

12. **Hiroki Miyazako**, Yutaka Hori, and Shinji Hara, "Turing Instability in Reaction-Diffusion Systems with a Single Diffuser: Characterization Based on Root Locus," The 52nd IEEE Conference on Decision and Control, Florence, Italy, Dec. 2013. (査読あり，口頭発表)

13. Takayuki Hoshino, **Hiroki Miyazako**, Atsuki Nakayama, Osamu Fukayama, and Kunihiko Mabuchi, "50-nm Resolution of Two-dimensional Patterning in Water by Using Inverted-Electron Beam Lithography," The 26th International Microprocesses and Nanotechnology Conference (MNC 2013), 6C-2-3, Sapporo, Japan, Nov. 2013. (査読あり，口頭発表)

Presentation at Domestic Conferences

1. 宮廻裕樹，星野隆行，"電子線によるバーチャル電極を用いた人工脂質膜の動的パターニング，"化学とマイクロ・ナノシステム学会第 36 回研究会，3P18(ポスター発表)，桐生市市民文化会館（群馬），2017.10.5.

2. 遠山渉，**宮廻裕樹**，星野隆行，"電子線走査型バーチャル電極によるナノ界面の電気化学イメージング，"化学とマイクロ・ナノシステム学会第 36 回研究会，3P18(ポスター発表)，桐生市市民文化会館（群馬），2017.10.5.

3. 宮廻裕樹，星野隆行，"電子線による高精細バーチャル電極ディスプレイを用いた膜ドメインと膜形態の動的制御（Dynamic Control of Membrane Domains and Morphology Using an Electron-beam Induced Fine Virtual Cathode Display），"第 55 回日本生

物物理学会年会, 1C1356, 熊本大学 (熊本)，2017.9.19．（口頭発表）

4. **宮廻裕樹**, 満渕邦彦, 星野隆行，"仮想電極ディスプレイによる脂質膜操作，" 第 64 応用物理学会春季講演会, 17a-F206-12, パシフィコ横浜（神奈川），2017.3.17．（口頭発表）

5. 遠山渉, **宮廻裕樹**, 満渕邦彦, 星野隆行，"電子線励起バーチャル電極による液体試料の電気化学イメージング，" 第 64 応用物理学会春季講演会, 16a-P2-4, パシフィコ横浜（神奈川），2017.3.16．（ポスター発表）

6. 星野隆行, **宮廻裕樹**, 吉岡基, 我妻玲, 満渕邦彦，"バーチャル電極ディスプレイの単一細胞解析への応用 -細胞内ひずみ解析とピンポイントエレクトロポレーション-," 第 64 応用物理学会春季講演会, 14a-F204-7, パシフィコ横浜（神奈川），2017.3.14．（口頭発表）

7. 富井潤, **宮廻裕樹**，奥谷智裕, 我妻玲, 星野隆行, 満渕邦彦，"筋芽細胞のネマチック性に基づく細胞配向パターンの誘導のための境界設計法，" 計測自動制御学会第 29 回自律分散システム・シンポジウム，調布クレストンホテル（東京），2017.1.31．（口頭発表）

8. **宮廻裕樹**, 満渕邦彦, 星野隆行，"電子線による局所電場を用いたリポソームの形状操作，" 化学とマイクロ・ナノシステム学会第 34 回研究会, 1P04, 幕張メッセ (千葉), 2016.9.6．（ポスター発表）

9. **宮廻裕樹**，満渕邦彦，星野隆行，"電子線による局所電場印加システムを用いた高分子レオロジーのその場制御，" 化学とマイクロ・ナノシステム学会第 33 回研究会, 1P07, 東京大学（東京），2016.4.25．（ポスター発表）

10. 星野隆行, **宮廻裕樹**, 満渕邦彦，"電子線誘起局所電界操作によるバイオ分子操作と in-situ リソグラフィ，" 第 63 回応用物理学会春季講演会, 20a-W323-1, 東京工業大学（東京）,2016.3.20．（口頭発表）

11. 吉岡基, **宮廻裕樹**, 我妻玲, 満渕邦彦, 星野隆行，"倒立型電子線描画を用いた細胞膜電気穿孔現象"，第 63 回応用物理学会春季講演会, 20p-P12-28, 東京工業大学（東京）,2016.3.20．（ポスター発表）

12. **宮廻裕樹**, 藤田恭子, 中村暢文, 大野弘幸, 満渕邦彦, 星野隆行，"生化学分析のための電子線による有機カチオン輸送制御 (Transportation Control of Organic Cations Using an Electron-beam for Biochemical Analysis)," 第 53 回日本生物物理学会年会, 2Pos228, 金沢大学（金沢），2015.9.14．（ポスター発表）

13. 吉岡基, **宮廻裕樹**，我妻玲, 満渕邦彦，星野隆行，"電子線の動電現象による単一接着性細胞への局所的な染色液導入の観察 （Observation of Local Dye Inflow into Single Adherent Cells induced by Electrokinetic Phenomena of Electron Beam）," 第 53 回日本生物物理学会年会, 2Pos207, 金沢大学（金沢），2015.9.14．（ポスター発表）

14. **宮廻裕樹**，満渕邦彦，星野隆行，"電子線による高電界生成を用いたナノ空間における物質輸送制御,"第 62 回応用物理学会春季学術講演会， 13a-D6-1，東海大学（神奈川），2015.03.13．（口頭発表）

15. 吉岡基，**宮廻裕樹**，我妻玲，満渕邦彦，星野隆行，"電子線描画を用いた細胞膜穿孔現象の閾値探索，"第 62 回応用物理学会春季学術講演会，11a-D5-8，東海大学（神奈川），2015.03.11．（口頭発表）

16. 村田俊樹，**宮廻裕樹**，満渕邦彦，星野隆行，"伸展誘発性収縮を考慮した心筋細胞群の収縮伝播特性のシミュレーション，"「細胞を創る」研究会 7.0，P-37，東京大学，2014.11.13-14．（ポスター発表）

17. **宮廻裕樹**，満渕邦彦，星野隆行，"ダイナミック電子線リソグラフィによる 2 次元ナノ流体制御，"日本機械学会第 6 回マイクロ・ナノ工学シンポジウム講演論文集，22am2-F5，くにびきメッセ（島根），2014.10.22．（口頭発表）

18. **宮廻裕樹**，村田俊樹，深山理，満渕邦彦，星野隆行，"電気－機械相互作用を考慮した心筋細胞群モデル，"第 52 回日本生物物理学会年会，3P137，札幌コンベンションセンター（北海道），2014.9.27．（ポスター発表）

19. 星野隆行，**宮廻裕樹**，我妻玲，満渕邦彦，"筋芽細胞のインパルス応答特性とひずみエネルギ計測，" 第 52 回日本生物物理学会年会，2P293，札幌コンベンションセンター（北海道），2014.9.26．（ポスター発表）

20. **宮廻裕樹**，我妻玲，満渕邦彦，星野隆行，"電子線励起作用による細胞培養環境の時空間ポテンシャル生成と拡散運動操作，"第 61 回応用物理学会春季学術講演会,19p-E17-20,青山学院大学（東京），2014.3.19．（口頭発表）

21. **宮廻裕樹**，深山理，満渕邦彦，星野隆行，"局所エネルギー供給による反応拡散系の空間パターン制御インタフェース，" 第 31 回日本ロボット学会学術講演会, RSJ2013AC 1 F1-05，首都大学東京（東京），2013.9.4．（口頭発表）